Characterization and Evaluation of Mechanical Properties of Ferritic and Austenitic Stainless Steel Weld Joint Using Gas Tungsten Arc Welding

Thesis submitted by

Angshuman Roy

Doctor of Philosophy (Engineering)

Department of Power Engineering
Faculty Council of Engineering & Technology
Jadavpur University
Kolkata, India
2024

JADAVPUR UNIVERSITY
KOLKATA – 7000 032, INDIA

INDEX NO. 43/18/E

1. Title of the thesis: Characterization and Evaluation of Mechanical Properties of Ferritic and Austenitic Stainless Steel Weld Joint Using Gas Tungsten Arc Welding

2. Name, Designation & Institution of the Supervisors:

i) **Dr. Subrata Mondal**
Assistant Professor
Department of Power Engineering
Jadavpur University, Salt Lake, 2nd Campus
Kolkata 700 106, West Bengal, India

ii) **Dr. Nabendu Ghosh**
Assistant Professor
Mechanical Engineering Department
Jadavpur University, Jadavpur
Kolkata 700 032, West Bengal, India

3. List of Publication:

Journal Publication

i) Roy, A., Ghosh, N. & Mondal, S. (2024). Analysis of the multi-criteria optimization strategies for determining the weld quality of dissimilar TIG welding between ferritic and austenitic stainless steel. Int J Interact Des Manuf 18, 1443–1457. https://doi.org/10.1007/s12008-023-01421-6

ii) Ghosh, N., Roy, A. (2024). Optimization of tig welding parameters to enhance the tensile strength of AISI 304 L stainless steel joints using taguchi methodology. Int J Interact Des Manuf https://doi.org/10.1007/s12008-024-02008-5

iii) Roy, A., Ghosh, N., & Mondal, S. (2023). Effect of heat input on mechanical and metallurgical properties of AISI 304L stainless steel by using TIG welding. Welding International, 37(2), 91–100. https://doi.org/10.1080/09507116.2023.2185169

iv)   Roy, A., Ghosh, N., & Mondal, S. (2023). Multi-criteria optimization of TIG welding process parameters on AISI 409M stainless steel by Grey Taguchi method. Welding International, 37(3), 135–141. https://doi.org/10.1080/09507116.2023.2198658

4 List of Patents: Nil

5. List of Presentations in International Conferences:

i)   Roy, A., Ghosh, N., & Mondal, S. (2024). Grey-Based Taguchi Technique For Parametric Optimization of TIG Welded AISI 304l Austenitic Stainless Steel, INCOM24: Proceedings of the 2nd International Conference on Mechanical Engineering Jadavpur University Kolkata India January 5 & 6, 2024, ISBN: 978-81-954806-6-1

ii)   Roy, A., Ghosh, N., & Mondal, S. (2024). Optimization of TIG Weld Process Parameters using the Taguchi Method and Grey Relational Analysis: A Review, International Conference on Advanced Mechanical Engineering and Industrial Management Organized by Department of Mechanical Engineering Swami Vivekananda Institute of Science & Technology, Kolkata.

I, **Angshuman Roy** registered on **19. 06. 2018** do hereby declare that this thesis entitled "**Characterization and Evaluation of Mechanical Properties of Ferritic and Austenitic Stainless Steel Weld Joint Using Gas Tungsten Arc Welding**" contains literature survey and original research work done by the undersigned candidate as part of Doctoral studies.

All information in this thesis have been obtained and presented in accordance with existing academic rules and ethical conduct. I declare that, as required by these rules and conduct, I havefully cited and referred all materials and results that are not original to this work.

I also declare that I have checked this thesis as per the "Policy on Anti Plagiarism, Jadavpur University, 2019", and the level of similarity as checked by iThenticate software is 09 %.

Signature of Candidate: *Angshuman Roy*

Date: 19/09/2024

Certified by Supervisor(s):
(Signature with date, seal)

1. **Dr. Subrata Mondal**   *S Mondal 19/9/2024*
Assistant Professor
Dept. of Power Engineering
Jadavpur University
Salt Lake, 2nd Campus
Kolkata-700 098

2. **Dr. Nabendu Ghosh**
ASSISTANT PROFESSOR
Mechanical Engineering Deptt,
Jadavpur University
Kolkata-700 032

CERTIFICATE FROM THE SUPERVISORS

This is to certify that the thesis entitled **"Characterization and Evaluation of Mechanical Properties of Ferritic and Austenitic Stainless Steel Weld Joint Using Gas Tungsten Arc Welding"** submitted by **Shri Angshuman Roy**, who got his name registered on **19. 06. 2018** for the award of Ph. D. (Engg.) degree of Jadavpur University is absolutely based upon his own work under the supervision of **Dr. Subrata Mondal** and **Dr. Nabendu Ghosh** and that neither his thesis nor any part of the thesis has been submitted for any degree/ diploma or any other academic award anywhere before.

1._____ 13/9/2024
Signature of the Supervisor
and date with Office Seal

Assistant Professor
Dept. of Power Engineering
Jadavpur University
Salt Lake, 2nd Campus
Kolkata-700 098

2._____ 19/9/2024
Signature of the Supervisor
and date with Office Seal

ASSISTANT PROFESSOR
Mechanical Engineering Deptt.
Jadavpur University
Kolkata-700 032

Thank you

Angshuman Roy

Angshuman Roy

Dedicated
To my teacher
Late Prof. Dr. Asish Bandyopadhyay
Prof. Mechanical Engineering Department
Jadavpur University

SYNOPSIS

Welding is a highly adaptable method for fabricating metal. Selecting the right welding technique and adjusting the input process parameters is crucial for welders to achieve high-quality joints. TIG welding is a highly versatile method for joining different types of materials, whether they are similar or dissimilar. It offers exceptional precision and can be incredibly useful in various applications.

Austenitic stainless steels (ASS 304L) and ferritic stainless steels (FSS 409M), known for their outstanding mechanical qualities, form the basis of many industrial components. The austenitic stainless steel and Ferritic stainless-steel exhibit excellent mechanical properties, including ductility, weldability, toughness, corrosion resistance, and high tensile strength at elevated temperatures. These properties make them highly desirable for a wide range of industrial applications, such as the nuclear industry, shipping industry, food industry, chemical industry, and so on.

The effectiveness of TIG welding depends upon a correct selection of input parameters. This process allows for the adjustment of several variables that can impact the quality of the weld. Certain variables may have a substantial impact, while others may have a less significant impact. The selection of welding process parameters is essential in achieving the desired quality of weld joints. Many characteristics, including joint strength, hardness, and ductility, serve as the basis for evaluating joint quality. The current literature review highlights the need for further investigation and analysis of various welding aspects to enhance process control and predictably produce the desired joint characteristics.

Many researchers have been conducted thorough research, exploring a wide range of factors and aspects, resulting in the development of a dependable and comprehensive database of knowledge. Furthermore, researchers also analysed the convergence of results through different optimization approaches. This analysis can only be achieved through ongoing research, which is necessary to understand the use of various optimization techniques in the field. The study of TIG welding of austenitic stainless steel and ferritic stainless steel (similar and dissimilar) under different input parameters conditions to make significant and valuable field for study. This research encompasses a wide range of aspects. The researchers have indeed conducted some work, with each focussing on or taking into consideration specific aspects. Conducting a study that examines a broad range of factors can pose certain

challenges. Studying and understanding the impact of various input parameters on factors such as response to ultimate tensile strength, hardness at different zones, weld width, yield strength, and percentage elongation can be quite challenging. This study may also incorporate process optimisation and microstructural analysis under different welding conditions.

The present research intends to investigate the effects of input parameters on features of geometry of the bead profile (penetration depth and bead width) and mechanical properties (UTS, % of elongation and microhardness) of 409M FSS and 304L ASS based similar and dissimilar weldment fabricated through GTA welding.

Based on three input parameters such as welding current welding, speed and flow rate of gas, experiments have been carried out based on Taguchi L_9 orthogonal array design of experiments. X-ray based visual inspection was performed first to study various surface / subsurface flaws: if it exists. The research also aims to attempt GRA and TOPSIS methodologies integrated with Taguchi method to determine an optimal setting of process parameters in purview of measurable estimates of bead geometry, microhardness, and tensile strength of the weldment.

The present research also focused a novel attempt to join incompatible material (Ferritic to Austenitic steels) which is of immense important in industrial contest.

Specific objectives of the present dissertation are stated out bellow.

To study effects of GTA welding parameters (welding current, scanning speed and flow rate gas) on bead geometry, microhardness, and tensile properties of the dissimilar weldment.

To study the appearance of the deposited beads through visual inspections followed by detailed microstructural (HAZ and FZ) analysis to be carried through optical microscopy and SEM (scanning electron microscopy).

To corelate microstructural features with tensile properties of the specimen weldment.

To determine and optimal setting of welding parameters to satisfy multiple requirements of the weld quality simultaneously. GRA and TOPSIS based Taguchi optimization module is intended to be attempted to solve such a multi-objective optimization problem. The multi - objective optimization is defined herein in such a way that the optimal setting can simultaneously minimise bead width, maximise penetration depth and maximise weld tensile strength.

The work is to be carried out in the present dissertation is believed to have great industrial

relevance in the following aspects.

Finally, the understandings, discussions, and analyses from the three different series of experiments (ASS 304L to ASS 304L, FSS 409M to FSS 409M, and ASS 304L to FSS 409M) help us come to some beneficial conclusions. These may be regarded as contributions stemming from the current study.

Here are a few representative figures that match some of the results:
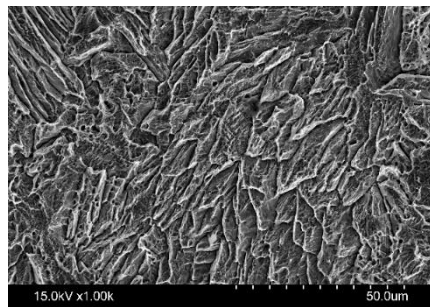
Figure 1 SEM micrographs (FZ)   Figure 2 Micro hardness profile
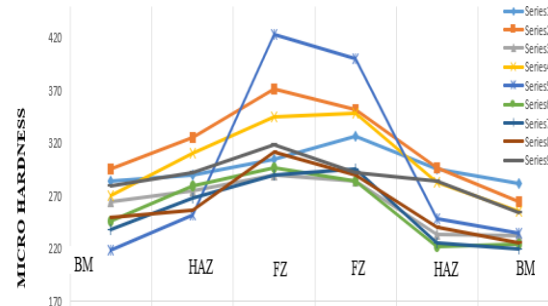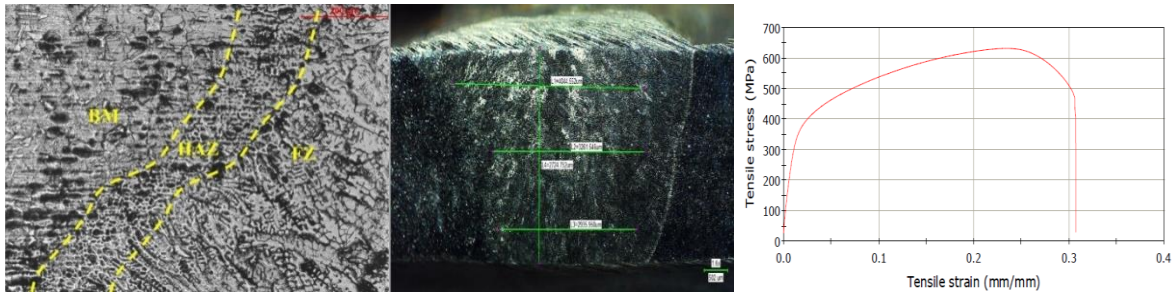
Figure 3 Microstructure (BM, HAZ, FZ), Weld bead geometry and Stress-Strain plot of welded sample

A

Alternating Current	AC
American Iron and Steel Institute	AISI
American Society for Testing and Materials	ASTM
Activated Tungsten Inert Gas	ATIG
Analysis of Variance	ANOVA
Austenitic Stainless Steel	ASS
Ampere	A, Amp.

B

Base Metal	BM
Body Centered Cubic	BCC
Bead Width	BW

C

Continuous Current Gas Tungsten Arc Welding	CCGTAW
Current	C
Cubic Feet Per Hour	CFH
Carbon	C
Chromium	Cr

D

Direct Current	DC
Depth of Penetration	DP

F

Ferritic Stainless Steel	FSS
Friction Stir welding	FSW
Face Cantered cubic	FCC

G

Gas Tungsten Arc Welding	GTAW
Grey Relational Grade	GRG
Grey Relational Analysis	GRA

I

Iron	Fe

H

Heat Affected Zone	HAZ
Higher- the- Best	HB
Hot-Wire Tungsten Inert Gas	HW-TIG

L

Lower- the-Best	LB

M

Metal Inert Gas	MIG
Magnetically Impelled Arc Butt	MIAB
Multiple Criteria Decision-Making	MCDM
Mild Steel	MS
Manganese	Mn
Molybdenum	Mo

N

Nominal- the- Best	NB
National Institute of Technical Teachers' Training and Research	NITTTR
Nickel	Ni

P

Plasma Arc Welding	PAW
Post Weld Heat Treatment	PWHT
Pulsed Current Gas Tungsten Arc Welding	PCGTAW
Percentage of Elongation	PE
Phosphorous	P

R

Response Surface Methodology	RSM

S

Shielded Metal Arc Welding	SMAW
Signal to Noise Ratio	SNR
Scanning Electron Microscope	SEM
Silicon	Si

T

Tungsten Inert Gas	TIG
Thermo-Mechanically Affected Zone	TMAZ
Technique for Order of Preference by Similarity to Ideal Solution	TOPSIS
Titanium	Ti

U

Ultimate Tensile Strength	UTS

V

Variable Energy Cyclotron Centre	VECC
Volt	V
Vickers Hardness Number	HVN

X

X-ray	X-radiation

Y

Yield Strength	YS

Page No.

Contents

Chapter 1

Chapter 2

Chapter 5

Chapter 6

1.1 Introduction

Welding is widely recognised as an exceptionally versatile method for metal and nonmetal joining of the manufacturing sectors. Welding is a permanent homogeneous joining process to join two or more than two pieces of the different materials or same materials (metal and nonmetal) to obtained a complete coalescence with the application of heat, pressure, or a combination of both with or without filler materials [1].

The joining methods are distinguished in different categories like permanent joining and semi-permanent joining. The semipermanent joints are rivets joint, nut and bolt joint, knuckle joint etc.

Welding joins are categorised as permanent joints because they accomplished homogeneity by heating and fusing the materials together. Typically, before the welding process begins, the metals are solid. When the welding is complete, there is a phase transition from solid to liquid and then back to a solid state. There are several variables that impact the weld quality, the most crucial of which are the heat affected zone (HAZ), mechanical and metallurgical characteristics, and the welding process itself. Since they are all adjustable process factors, welding quality is influenced by them. The main influencing factors for quality of weld are current, travel speed, gas flow rate, plate to nozzle distance, and filler material, if necessary [2].

A variety of industries use welding, a basic and adaptable technique, to permanently join materials. Contributing to the development of buildings, machines, and goods that are necessary for our everyday lives, it is fundamental to the construction, manufacturing, automotive, aerospace, and many other industries. Fundamentally, fusion welding is a method that helps to join materials by melting them together. The welding technique used might apply heat, pressure, or a mix of both to accomplish this procedure. There are several welding procedures, each designed to fit certain materials, uses, and specifications, so welding is not restricted to a single method. Not only is welding a mechanical process, but it is also a very skilled art that requires a thorough knowledge of materials science, metallurgy, and welding procedures. To achieve exact welds that satisfy strict quality requirements, welders need to be skilled in choosing the right welding technique, adjusting temperature and

pressure, and so on. An elementary summary of welding as a major industrial process is given in this introduction. Discussions of different welding methods, their uses, safety measures, and the influence of new technology on the welding industry will follow.

TIG welding, also known as GTAW (gas tungsten arc welding), is a welding technique that employs a non-consumable tungsten electrode and a shielding gas to prevent oxidation and improve the weld's quality. Helium and argon gases are primarily employed for shielding purposes. Weld quality is examined by a variety of factors, namely weld bead profile, mechanical-metallurgical properties, and weld chemistry. Important things that affect these traits a lot include the weld bead's shape, the groove's angle, the type and combination of shielding gases, and various input parameters like welding current, flow rate of gas, travel speed, electrode type, edge preparation, welding position, and the distance between the plate and the nozzle. The combined impact of several input factors determines the amount of joint strength required to fulfil the weld's practical requirements in real-world applications.

Thus, creating a high-quality welding seems to be a difficult task. [3,4]. In the present work, the two different materials like 409M Ferritic stainless steel (409M FSS) and 304L Austenitic stainless steel (304L ASS) have been chosen as parent material in view of specific applications in power engineering. At high temperatures, Austenitic stainless steel exhibits excellent resistance to creep and oxidation, whereas Ferritic stainless-steel serves to prevent the leaching of nickel by melted magnesium.

FSS is classified as a member of the iron-chromium alloy family, representing a distinct form of stainless-steel alloy. The material is renowned for its exceptional ability to resist corrosion, particularly in settings where it may encounter compounds containing chloride, such as saltwater or specific industrial chemicals. Ferritic stainless steel is classified as one of the five fundamental categories of stainless steel, being Austenitic, martensitic, duplex, and precipitation- hardened stainless steels.

Crystal structural analysis has demonstrated that FSS possess a BCC (body-centred cubic) structure of crystals. In a BCC (body-centred cubic) structure of crystals, atoms are located at the corners of the unit cell, with an additional atom positioned in the centre of the cell. FSS exhibit certain traits according to their composition, including pronounced magnetic properties and exceptional strength.

The FSS 409M is a member of the 400 series. The magnetic properties and high chromium content of Ferritic stainless steels are its defining characteristics. The chemical composition is Chromium (Cr): 10.5% - 11.75%, Manganese (Mn) 1.0% max, Carbon (C): 0.03% max, Sulphur (S): 0.02% max, Nickel (Ni): 0.5% - 1.5%, Silicon (Si): 1.0% max, Phosphorus (P): 0.04% max.

Wide range of application FSS 409M stainless stemless steel mostly these stainless steels are used in

Automotive exhaust systems: It is used because of its ability to resist corrosion and oxidation at high temperatures.

Industrial equipment manufacturing: It is used in several industrial applications that need resistance to corrosion, heat, and abrasion.

Heating appliances: FSS 409M steel is used for the manufacturing of heating equipment such as furnaces, ovens, and heat chambers because of its high heat resistance.

ASS is a specific kind of stainless-steel alloy that is renowned for its remarkable resistance to corrosion, notable ductility, and superb formability. This alloy is classified within the iron-chromium-nickel family and is recognized as a highly prevalent category of stainless steel. Austenitic stainless steel exhibits distinctive properties due to its Austenitic crystal structure, which exhibits remarkable stability even under ambient conditions.

ASS have a non-magnetic, FCC (face-centred cubic) crystal structure, making them more resistant to corrosion and ductile compared to other types of stainless steels. The crystal structure is essential when discussing a material's physical and mechanical properties

Chemical composition is Chromium (Cr) 18% to 20% Nickel (Ni): 8–10 %, carbon (C): up to 0.08 % Maximum of 2% manganese (Mn), silicon (Si) content: 0.75 % Max. phosphorus concentration: 0.045% Maximum concentration of sulphur (S): 0.03%.

The most common applications for SS304L stainless steel are

Food Processing Equipment: The food sector commonly used SS304L because of its resistance to corrosion and its ease of cleaning.

Chemical Containers: Because of its chemical reaction resistance properties, it may safely store and caustic transport compounds.

Medical Equipment: Because of its resistance to corrosion and biocompatibility, SS304L is used in various medical and surgical tools industries.

Heat Exchangers: It is an ideal material for use in heat exchangers because to its low corrosion resistance and high thermal conductivity.

There are a variety of uses for both ASS304L and FSS409M due to their distinct features. The automotive and industrial sectors are two examples of areas where FSS409M are used due to its high-temperature resistance and durability under stress. Conversely, sectors that prioritize hygiene and corrosion resistance often utilize ASS304L.

This study used several tests and an optimisation analysis to investigate the TIG butt welding of FSS 409M and ASS 304L. During operation, adjust the input process control parameters to get the required outputs. Select the input variables like welding current, flow rate of gas, and travel speed. This phase is crucial in the procedure. The weld joint is evaluated based on the UTS (ultimate tensile strength), PE (elongation percentage), YS (yield strength), and VHN (microhardness). Another important factor to consider is the width of the weld and penetration depth of the weld. Stringent quality standards have been implemented for the UTS (ultimate tensile strength), PE (elongation percentage), YS (yield strength), and VHN (Vickers hardness number) to optimise the joint's qualities. According to the literature survey, using the minimum weld width that is feasible would improve the weld joint's excellence. As a result of improved criteria, weld width decreased. The focus of this research is to investigate how these characteristics affect the weld's quality. Various methods, including traditional experimental design as well as Taguchi L$_9$ orthogonal array design, are used to set the settings for actual levels. Therefore, establishing a high-quality weld seems to be a difficult task. Regression analysis, the Taguchi method, and TOPSIS (Technique for Order Preference by Similarity to Ideal Solution) technique are some of the statistical methods that researchers have used to predict and improve the shape of weld beads and the quality of welds in gas tungsten arc welding (GTAW or TIG welding). Modelling, experimental, and analytical research may be used to study how process parameters affect different results. Developing mathematical models to represent reactions based on process parameters often requires using multiple linear regression and response surface methodologies. To find the best parameter configuration based on the needs, each quality aspect is changed to increase or decrease accordingly. This strategy is only suitable for use when maximizing a single objective function. When dealing with several goals, it is crucial to consolidate them into a unified objective function that is equitable and optimized. The

Taguchi technique has seen efficacy in several research investigations. This technique depends on a well-balanced orthogonal array design that uses a small number of tests. Traditional Taguchi techniques are ineffective when dealing with scenarios with several goals. Gray relational analysis must be used with the Taguchi approach to address this issue. Another approach to optimizing TIG welding parameters involves combining the TOPSIS. The TOPSIS method facilitates multi-criteria decision-making. This metric is employed to determine which option is most favourable among a given set of alternatives, according to their degree of proximity to the optimal solution.

Multiple responses have been combined into a single response optimized with the use of Grey Relational Analysis (GRA). A mathematical model is established between process parameters and GRA after applying the GRA method. TOPSIS optimization techniques used to solve the mathematical equation of YS for optimizing all welding responses collectively. A comparative study was conducted to determine the ideal welding condition by comparing the results obtained by TOPSIS.

This study focusses on optimising the welding process parameters in relation to the predetermined welding responses. In manufacturing processes, the overarching objective is to attain the desired output efficiently, minimizing both time and cost. This principle holds true for welding, necessitating the adjustment of input parameters to enhance process efficiency and cost-effectiveness. Achieving this requires a comprehensive understanding of how each parameter influences output responses and the extent of their impact. Accurate recognition of variation patterns can eliminate the need for trial-and-error procedures in the future. The primary aim of this study is to augment the existing knowledge on TIG welding, enabling more precise management of the process to achieve the desired weld joint quality.

Several physical qualities such as strength, hardness, ductility, toughness, corrosion resistance, and wear resistance influence the microstructure texture of a material, which refers to its surface structure. Understanding the science of weld metallurgy is crucial and may be evaluated by analysing microstructures. The weld's quality is defined by the microstructures found in the weld area, base material, and HAZ. Under specific circumstances, conducting microstructural investigations can enhance our understanding.

1.2 Background of TIG Welding

TIG welding, alternatively known as GTAW, emerged as a welding technique during the 1930s and has subsequently gained substantial popularity as a means of metal fusion. TIG welding emerged because of independent developments by two engineers throughout the 1930s. TIG welding technology was advanced through the contributions of Charles Langmuir, an esteemed scientist from the United States, and Russell Meredith, a notable engineer hailing from Australia. The technique was patented by Langmuir in the United States in 1941. TIG welding garnered considerable recognition and utilization in the context of World War II for military purposes, including in the fabrication of aeroplanes and many other military apparatuses. The material was highly regarded due to its capacity to generate welds of superior quality on a range of metals, encompassing aluminium and magnesium alloys. Following the conclusion of World War II, TIG welding experienced a continuous process of refinement and witnessed a surge in its utilization across diverse sectors such as aerospace, automotive, and manufacturing. Advancements in technology have led to significant improvements in TIG welding equipment, hence enhancing its accessibility to a broader spectrum of users. Throughout the course of time, there have been notable progressions in the field of TIG welding technology. The adaptability and quality of TIG welding have been enhanced by the advancement of shielding gases, electrode materials, and welding processes. TIG welding is widely recognized in the welding industry for its remarkable precision and ability to produce flawless and high-quality welds. The application of this method is widespread in businesses that place a high value on the quality of welds and visual attractiveness, including the aerospace, automotive, nuclear, and pharmaceutical sectors. Furthermore, the preference for utilizing this technique is widespread when it comes to the welding of non-ferrous metals, including but not limited to aluminium, magnesium, and stainless steel. In the present day, TIG welding remains an essential welding procedure that is commonly utilized alongside other approaches, including MIG welding and Stick welding. Welders continuously improve their skillset as they observe developments in equipment, which are typified by improved simplicity of use and greater complexity. These advancements are highlighted by the integration of digital controls and automation capabilities.
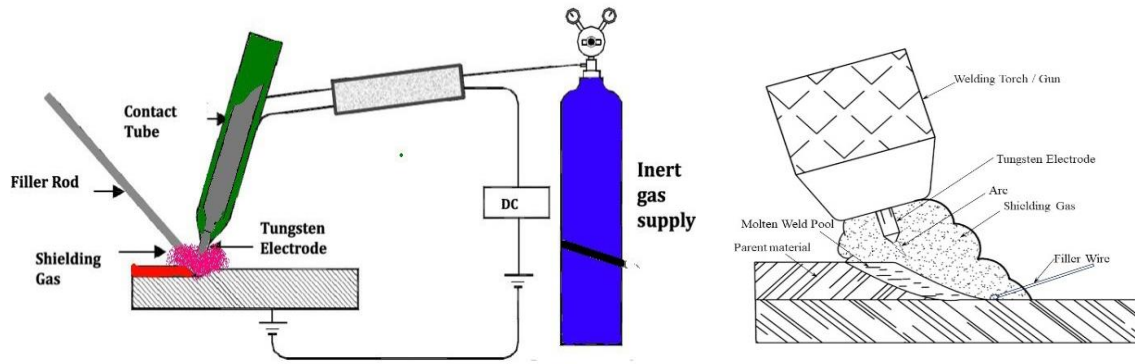
Figure 1.1 A schematic sketch of TIG welding

A simplified diagram of TIG welding has been shown in Figure 1. In this procedure, metal coalescence takes place through heat energy by creating an arc between the parent metal and a non-consumable tungsten electrode. A tungsten electrode is used to maintain a uniform arc. Shielding is achieved from a gas only or gas mixture argon, helium, or a mixture of the two is used. This process can create high-quality weld joint using all types of metals and their alloys. TIG Welding produces far lower levels of smoke compared to GMAW and SMAW [5].

1.3 Equipment's Used in TIG Welding:

Butt welding was performed for this investigation. The necessary welding equipment is given below.

Source of power: A steady current power source is usually needed for TIG welding. AC (alternating current) and DC (direct current) sources are used, but it depends on the material that needs to be weld. In this experiment Input 3 phase AC current and the output DC current with straight polarity have been used.

Tungsten Electrode: In TIG welding, tungsten electrodes are used because they can handle high temperatures and have a high melting point. Pure tungsten and thoriated tungsten are two common types tungsten used.

Welding Gun or Torch: The TIG torch or gun is used for controlling the welding process. It holds the tungsten electrode and lets the welder control the current, the flow of gas, and the addition of filler material.

Supply of Shielding Gas: TIG welding necessitates the use of shielding gas to prevent the molten metal from being contaminated by gases present in the atmosphere, such as carbon

dioxide, oxygen, nitrogen, and water vapor. Depending on the specific need, we often use argon, helium, or a combination of both as shielding gases.

Gas Flow Control Valve Switch: A valve regulator switch maintains a constant and suitable flow rate of shielding gas by controlling its flow from the gas cylinder to the TIG torch.

Welding Filler Rods: Filler rods are used to strengthen the weld joint quality by adding material, hence enhancing the weld. The selection of filler rod is contingent upon the base metal being welded.

Welding gloves and goggles: TIG welding produces heat and ultraviolet rays. Welders must wear suitable protection equipment such as gloves, a welding helmet with the correct shade, flame-resistant clothes and googles.

Workpiece Fixture or Welding Table: To keep the workpieces in place during welding, a uniform work surface or fixture is required.

Welding Power source Cable and Ground Clamp: The power source cables are connecting the TIG torch to the welding machine. A ground clamp is used to ensure a correct electrical connection and ground the workpiece.

1.4 Metal Transfer Method in TIG Welding

Molten metal transfer is the process by which the electrode transfers molten metal to the workpiece in TIG welding. The following metal transfer modes are commonly used during TIG welding:

Short-circuiting: Short-circuiting transfers occur at the lowest current levels. The electrode and the weld pool make direct contact, resulting in the transfer of metal from the electrode to the workpiece. This transfer occurs at an average rate of 20 to 200 times per second.

Lateral Transfer: In the lateral transfer (free flight) phase, the molten metal forms an attachment between the electrode and the workpiece, acting as a bridge. The combination of surface tension and gravity causes the molten metal to flow horizontally over the gap.

Droplet Transfer: In the droplet transfer mode, tiny droplets of molten metal are formed and detached from the electrode at regular intervals. The weld bead is formed when the droplets land on the workpiece. Thin materials work well in this mode, which is often linked to lower current levels.

Spray Transfer: It is possible to switch to a spray transfer mode when using a higher current during TIG welding. This technique involves spraying tiny droplets of molten metal onto the workpiece across the arc that extends from the electrode. When deeper penetration and faster deposition rates are required, spray transfer is the method of choice.

1.4.1 TIG Welding Input Process Parameters

Some process factors influence the weld characteristics in every welding process. The correct parameters must be chosen to achieve the intended outcomes. In TIG welding, the depth of penetration, shape of the bead, and overall quality of the weld are all affected by things like the welding current, travel speed, gas flow rate, and more. The following sections explain many of these process factors [6]:

Welding current: Welding current is an essential variable that directly affects weld characteristics such as weld bead profile, depth of penetration, deposition of metal rate, and input heat of the weldment. Excessive current may damage the workpiece, whereas insufficient current in TIG welding might cause the filler wire to stick. When using direct current with electrode negative, the negative electrode should be chosen over the positive electrode to provide more weld penetration and faster travel speed. In gas tungsten arc welding, reverse polarity on the other side can lead to fast heating and deterioration of the electrode tip because the anode heats up more than the cathode.

Travel speed: The relationship between travel speed and heat input is inverse. Reducing travel speed increases heat input, resulting in greater penetration and fusion, while a faster speed decreases it, potentially causing partial fusion and weaker weld. Regulating travel speed is crucial for reducing heat distortion in the workpiece. Maintaining a uniform travel speed during welding helps disperse heat and reduce distortion. Material thickness also influences the appropriate travel speed, thicker materials need a slower rate of travel speed to absorb and penetrate heat effectively, but thinner materials may need faster speeds.

Gas flow rate: The gas flow rate significantly influences the quality of a weld. Commonly 99.9 % pure Argon, helium, or a combination of both gases are often used for better results in TIG welding to shield the weld pool from the surrounding environment. Insufficient gas flow rate does not effectively shield the weld pool, while excessive gas flow leads to mixing with the surrounding air, causing porosity and cracks in the weld area.

Table 1.1 Characteristics of Different Shielding Gases

Characteristics	Helium	Argon	Mixture of both
Travel speed	Faster speed	Moderated speed	With cent percent Argon, scanning speeds are optimised.
Penetration	Augmented penetration	Lower penetration	Enhanced penetration over cent percent Argon
Cleanup	Less cleaning required	Upright cleaning action	Cleaning properties like Argon
Flow Rate	Higher flow rates (2 times)	Slower flow rates 10-30 CFH	Better flow rates than Argon
Arc Starting	Arc beginning is challenging	Easily arc produce	Enhanced arc starting over cent percent Helium
Arc Voltage	Higher arc voltages	Lower arc voltages	Arc voltages between cent percent Argon and Helium
Stability of Arc	Less low-amp stability	Highly stable arc	Enhanced arc stability over cent percent Helium
Cost	Higher cost than Argon	cheap cost and easy availability	More expensive than Argon

1.4.2 TIG Welding Responses

In this present study there are different types of output responses are measured and discussed details here. The output responses are defining the quality of weld joint and they are depending on different parametric conditions. The output responses consist of UTS, YS, microhardness, % of elongation, welding bead profile of the weld pool zone.

Weld bead size: The weld bead determines the quality of welding. Factors such as weld current, flow rate of gas, and travel speed have an impact on the shape of the weld bead. The quality of the weld bead directly influences the mechanical and metallurgical characteristics.

By reducing the bead width and HAZ, one can effectively minimise defects and achieve optimal results. Therefore, opting for a smaller bead size is more favourable.

Ultimate tensile strength: The primary determinant of weld joint efficiency is the maximum amount of stress (force per unit area) a material can withstand while being stretched or pulled before breaking. It represents the peak point on a stress-strain curve during a tensile test.

Percentage of elongation: In a tensile test, the ductility of a material may be evaluated by calculating the percentage of elongation. It gives an indication of the extreme amount of stretching that the material can withstand before breaking under stress.

Yield strength: Yield strength also an important factor to define the weld joint quality. If the joint quality is acceptable then yield strength quality gives the better results. The yield strength is a crucial parameter derived from a tensile test. The stress level at which a material undergoes irreversible distortion and loses its ability to regain its true shape is known as the elastic limit. The yield strength value is a significant occurrence for different structures whose quality can perform in an elastic region under normal conditions.

Hardness: Hardness is a fundamental characteristic of a material that describes its mechanical properties, including its ability to resist deformation, its ability to undergo plastic deformation, and its overall strength. Hardness is a crucial characteristic of a high-quality weldment.

1.5 Review of Past Research Work

This section provides a comprehensive review of previous research studies focused on TIG welding of austenitic and ferritic stainless steels. TIG welding, known for its precision and versatility, has been extensively studied to optimize its applications and understand its effects on different materials. A literature study on TIG welding generally includes an in-depth overview of the welding process, its principles, and practical applications across various industries. It also explores recent advancements in techniques, equipment, and materials to enhance welding quality and efficiency. Additionally, key findings from prior research are highlighted, emphasizing improvements in weld strength, corrosion resistance, microstructure, and thermal behaviour. Below is a detailed summary of

the insights and developments from existing studies on TIG welding, with a particular focus on its application to stainless steels.

Ramkumar et al. [9] investigated the weldability of FSS 430 using TIG welding, with and without active fluxes. This study examined the mechanical properties, metallurgical characteristics, and penetration depth of SS 430 weld beads while utilizing SiO_2 and Fe_2O_3 fluxes. Vidyarthy et al. [10] investigated how SUPERTIG ER 309L could be used as a filler material in A-TIG and M-TIG welding of AISI 409 FSS that is 8 mm thick. Various combinations of flux coating thickness, welding current, and welding speed successfully achieved full penetration in bead on plate welding. The A-TIG technique has the potential to improve the mechanical strength and joint penetration of the 409 FSS weldment. Anttila et al. [11] The study investigated the welding of low and medium chromium ferrite stainless steel using various filler wires. To distinguish between the joints, tensile strength, impact toughness, microhardness, and Erichsen cupping tests were conducted. Following welding, the focus shifted to examining the impact of heat treatments on ductility and toughness. Using A-TIG welding in their study, Vidyarthy and Dwivedi [12] studied the corrosion behavior of AISI 409 ferritic stainless steel (FSS) under different welding parameters. They analyzed the effects of welding current, flux coating density, and welding speed, identifying conditions that caused the highest and lowest corrosion levels to optimize welding practices. Vidyarthy and Dwivedi [13] investigated weldability of AISI 409 steel using A-TIG welding process. They have exhibited the influence of the different components like activating flux and its quality on the bead geometry. Ambade et al. [14] discovered the many welding techniques used to join AISI 409M SS, including TIG, MIG, and SMAW. They also compared the experimental and simulation results of the Goldak heat source model. In the end, we found the computational and experimental results for those welding processes to be outstanding. Lakshminarayanan et al. [15] investigate the effects of welding with SMAW, GMAW, and GTAW on the tensile and impact characteristics of AISI 409M FSS of 4 mm thickness. They discovered that AISI 409M FSS GTAW weld joints are superior to SMAW and GMAW joints in terms of tensile and impact strength. This is because the fusion and HAZ zones have a fine grain structure. Using ER304L and ER308L as two different austenitic filler wires during gas metal arc welding, Gupta et al. [16] investigated the impact of different levels of heat on the mechanical characteristics of 409L FSS and microstructure. The three heat input levels used

in this work are 0.3, 0.4, and 0.5 kJ/mm. It was discovered that the heat input affected the microstructure, microhardness, tensile properties, microstructure percentage dilution, and chromium-nickel ratio. The welded samples exhibit exceptional mechanical characteristics, even with a heat input as low as 0.4 kJ/mm. **Kose and Topal [17]** conducted a plasma arc welding (PAW) study on Ferritic stainless steel AISI 410S, utilising varying welding current conditions. Heat treatment after welding has been used to evaluate the differences in mechanical characteristics and microstructure between PWHT cases and those without PWHT. As a result of the tensile test, all samples also experienced ductile fracture modes. **Amuda and Mridha [18]** performed welded joints of Ferritic stainless steel AISI 430 using TIG welding technique with energy input ranging from 0.205 to 2.05kj/mm and is then examined for microstructure and hardness. The inter dendritic martensite and grain boundary martensite, together with some inter metallics in varied proportions, are likely present in the fusion zone and high-angle zone, respectively, according to the microstructural analysis of the welds with different heat input rates. According to the hardness values measured across the welds, when more heat is supplied during welding, grain refinement and intermetallic presence are decreased, allowing transformation to take place inside the dual phase zones. **Vidyarthy and Dwivedi [19]** studied the corrosion behaviour of the A-TIG weld fusion zone is a problem, however AISI 409 Ferritic stainless steel is employed in freight train carriages, ocean containers, and equipment for sugar refineries. For analysing the corrosion behaviour, potentiodynamic polarization tests were run. **Mousazadeh and Haghighi [20]** investigated inter-pass temperature has an impact on the microstructure growth and mechanical characteristics of AISI 430 steels when it is autogenously tungsten inert gas (TIG) welded, leading to a higher amount of martensite and a larger HAZ width and grain growth, which results in low tensile strength and ductility. **Lakshminarayanan et al. [21]** studied the microstructure and mechanical feature of FSS joints made with AISI 409M grade by electron beam welding. The results showed an overmatch between the weld metal and the parent metal. However, the joints exhibited commendable characteristics in terms of impact toughness and bend strength. **Akita et al. [22]** conducted a study that examined the microstructures, mechanical characteristics, and fatigue nature of welds made from FSS SUS430 using various filler metals. To perform MIG butt welding on SUS430, it was necessary to use two distinct filler metals, namely Filler I and II, which had different chemical

compositions. Al and Ti were among the coarser grains visible in the microstructure of Filler I. Due to the production of martensite, which is a hard material that resembles a needle, the HAZ in both welded joints had the highest hardness. The filler I welded joint required more heat to weld than the filler II welded joint. As a result, filler I's martensite content was both larger and more numerous than filler II's. **Mohandas et al. [23]** investigate Shielded metal arc welds exhibited lower tensile and yield strengths compared to gas tungsten arc welds, which displayed grains that were consistently spaced. Gas tungsten arc welding also demonstrated a slightly greater average tensile ductility compared to SMAW. When compared to the parent metal, welds typically exhibited constrained ductility. The filler material has been improved by the addition of copper and titanium, resulting in a major increase in the strength of the alloy compared to its original form. There could be a correlation between the fracture morphology and austenite content, which might explain the observed characteristics. **Lakshminarayanan and Balasubramanian [24]** examined the mechanical and microstructural characteristic of a FSW joint in Ferritic stainless steel 409M. They produced flawless single-pass welds without volumetric defects with a 1000 revolutions per minute rotational speeds. They conducted transverse tensile, impact, bend, and microhardness tests. Frictional agitation causes a lot of strain and a fast-cooling rate, which changes the base material's large ferrite grains into very small grains with a structure made up of both martensite and ferrite. The base metal and weld metal are overmatched, as indicated by tensile tests. Additionally, the joints demonstrate satisfactory impact durability and ductility. In their study, **Lakshminarayanan and Balasubramanian [25]** established a correlation between the process parameters and the mechanical and metallurgical characteristics of FSS 409M plates with a substantial thickness of 4 mm, using (FSW) friction stir welding. **Dinaharan et al. [26]** In the investigation, it was found that 4 mm thick AISI 409 Ferritic stainless-steel tubes were MIAB weldable. MIAB welding is utilized in industries to link metallic tubes and pipes. The joint region grew larger as the arc rotation current increased, and the axial shortening increased as well. At higher and lower current limits, the upsetting was incorrect. Due to grain refinement and dislocation fields, TMAZ demonstrated a multifield improvement in hardness, and the selection of arc rotation current is essential to achieving sound joints. **Delgado et al. [27]** A Ferritic stainless steel was joined utilizing GTAW both with and without filler metal, as well as with filler metal that is typically

Austenitic stainless steel (GTAW). In the heat affected zone, microstructure showed martensite laths and a coarse Ferritic matrix (HAZ). Austenite, martensite, and ferrite were shown to be associated with dilution between the filler and parent metal. **Zaman et al. [28]** investigate the butt TIG welding process using AISI 430. The results show that there are martensite and carbides where the grains meet, as well as a large grain structure in the HAZ and FZ. FSS has restricted ductility and is susceptible to cracking in demanding conditions because of its enhanced strength and hardness in the welding zone. **Delgado et al. [29]** used the GTA Welding Process to join Ferritic stainless steel. They performed welding using both conventional Austenitic stainless steel filler metal and without it. The microstructure of the HAZ exhibited a coarse Ferritic matrix together with martensite laths. Dilution occurred among the base metal and filler when the weld metal included austenite, martensite, and ferrite. Although the ductility increased by 25% compared to the base metal, there was also an improvement in toughness and tensile strength. **Ghosh et al. [30]** conducted a study on Ferritic stainless steel weld specimens, subjecting them to an X-ray radiography test to identify surface as well as the subsurface defects. They assessed the weld's quality using YS, UTS, and the % of elongation of the welded samples. They examined, discussed, and analysed the observed data using Grey-Taguchi, as well as checking the UTS, YS, and % of elongation. **Benlamnouar et al. [31]** investigated how to improve the welding process parameters of AISI 430 FSS welds by using Taguchi's design method to reduce the size of the ferrite grains. The minimal grain size was selected by using two input parameters: speed and welding current. Weld quality was examined by using ANOVA to find the effect of various parameters. Signal-to-noise analysis determined the optimal set of settings. Tensile testing, image correlations, optical microscopy, and electronic microscopy were used for experimental characterizations. The best conditions for welding created a smooth microstructure with few martensite particles and a better balance of strength and ductility, which caused ductile fractures in the base material. **Lakshminarayanan et al. [32]** examined the microstructure of the CCGTAW, PACAW, and PCAW joints, additionally the morphology of the fracture areas and mechanical properties on 409 M-grade Ferritic stainless steel.

Raveendra et al. [33] The study, which used GTAW procedures, aimed to compare the effects of current with and without pulses on the properties of weldments made of 3 mm thick AISI 304 stainless steels. Heat exposure causes fine grain refinement, resulting in maximum

hardness. The non-pulsed current weldments have the highest tensile strength. They also observed that the UTS and yield strength (YS) values of non-pulsed current weldments were higher than those of base metal and pulsed current weldments. **Ghosh et al. [34]** investigated GMAW with 316L filler wire to compare the different ways of welding FSS 409M and ASS 316L. They conducted the experiment using the Taguchi L_9 orthogonal array method. They measured and recorded the weld's yield strengths, tensile strengths, and percentage elongation. **Lothongkum et al. [35]** performed TIG welding on SS 316L with a plate thickness of 3 mm in various positions. They used pure argon as the shielding gas. They analysed an acceptable weld bead geometry with full penetration depth using welding speed and nitrogen contents in the argon shielding gas. The findings indicate that increasing the nitrogen content of argon gas reduces pulse currents, while increasing welding speed directly increases the pulse current. **Pasupulla et al. [36]** examining the mechanical behaviours of a welded joint and defects caused by these mechanical behaviours, such as tensile testing, bending, hardness testing, and impact testing carried on a work piece in destructive testing. The inner defects of sample detected through radiographic testing in non-destructive are produced on stainless steel 304 (SS304) plates using TIG welding equipment. After finishing the task, examine the quality and performance of the TIG-welded plates to compare mechanical faults and radiographic testing defects. The inner defects of sample detected through radiographic testing. Finally, they found the quality and performance of the TIG-welded plates to compare mechanical defects and radiographic testing defects. A study by **Yan et al. [37]** looked at the microstructure structure and mechanical properties of ASS 304 joints that were made with a laser, TIG, or a mix of the two. The phase composition was analysed using X-ray diffraction, and the joints' microstructure was analysed using microscopy. This was followed by the completion of tensile tests and the examination of the fracture surfaces. According to the findings, the laser-welded joint exhibited the uppermost tensile strength and the smallest dendritic grain size of all joints, while the TIG-welded joint exhibited the lowest tensile strength and the largest dendritic grain size. Transition zones and heat-affected zones are also clearly visible in the TIG welding joint. Fractography revealed a cup-and-cone-shaped fracture in the TIG welding joint, while the laser welding and hybrid welding joints displayed pure shear fractures. SS304L are suitable for joining by laser and hybrid welding due to their superior mechanical qualities and fast welding periods. **Durgutlu**

[38] studied TIG welding of 316L and examined microstructure, penetration depth and mechanical properties in different shielding gas composition. Hydrogen in argon as shielding gas increased mean grain size, penetration depth, and width of 316L Austenitic stainless steel, resulting in higher tensile strength. **Aslam and Sahoo [39]** evaluated the effects GMAW on mild steel substrates coated with stainless steel AISI 304. Microscopical and EDS tests have confirmed the effective deposition, and they have created a computer model to evaluate the impact of welding conditions on the morphology of the clad beads. Non-uniform weld bead formation was observed at reduced voltage and low WFR. During the cladding procedure, the wire input rate increased. **Kumar and Shahi [40]** examined the mechanical and metallurgical properties of 304 stainless steel joints in relation to heat input. After careful analysis, they found that the welding joints with lower heat input exhibited superior UTS compared to those welded with intermediate and elevated heat input. There was a noticeable increase in grain coarsening in the HAZ, and as the heat input increased, the average dendritic length and inter-dendritic spacing also increased. In TIG welding, the welded Ferritic stainless-steel joints, the impact of filler metals on fatigue crack growth behaviour was examined by **Shanmugam et al. [41]** Because of its increased yield strength, hardness, and toughness, duplex stainless steel filler metal has been observed to have better fatigue performance. **Mahajan et al. [42]** investigate how the composition of the filler material affects the welding characteristics of stainless steel 304 in a semi-automatic TIG process. The investigation focused on single V-butt joints using plates that were 6 mm thick. After that, they checked the surface roughness (R_a) value, tensile strength, and micro hardness and used ER (308L, 310, and316L) as filler materials for analysis of the joints. The study revealed that the properties of the filler materials ER 310 and 316L were inferior to those of ER 308. The SEM/EDAX test showed that there were a lot of alloying elements in the joints made with the ER (308L, 310L, and 316L) filler materials. Additionally, the fabrication of joints using the filler material ER 316L revealed a significant presence of alloying components. **Zhou et al. [43]** studied the effect of filler material composition on the welding characteristics of ASS 304 during semi-automatic TIG welding. They evaluated joints made with ER 310, ER 308L, and ER 316L fillers based on surface roughness, tensile strength, hardness, and SEM/EDAX analysis, finding that ER 308L provided the best results, while ER 316L and ER 310 showed less favourable properties. **Ghosh et al. [44]** investigated the use of MIG welding in butt

17

joints to join samples of AISI 316L stainless steel with various settings. The study employed both visual examination and X-ray radiography examinations to evaluate the impact of the process parameters. In terms of UTS, YS, and % of elongation, the weld's quality has been assessed. **Ghosh et al. [45]** experiments and studied, the impact of current, flow rate of gas, and plate to nozzle distance on the weld quality of AISI 316L ASS during metal inter gas arc welding has been investigated. **Kumar and Shing [46]** investigated the influence of oxide flux on the microstructure, mechanical characteristics, and form of welded 304 Austenitic stainless-steel joints. They employed a blend of six unique oxides, including FeO_3, Cr_2O, MoO_3, Fe_2O_3, Al_2O_3, and SiO_2. They used autogenous TIG welding and applied a fine layer of oxide before joining an 8-mm-thick Austenitic stainless-steel plate. The results exhibited that the use of metal oxides greatly improved the depth of penetration, although Al_2O_3 did not produce satisfactory results. The weld's mechanical properties were almost the same as those of the parent metal. **Ghosh et al. [47]** The study emphasizes on welding AISI 316L stainless steel samples using MIG welding to create butt joints with a consistent 3mm plate thickness. Crucial factors like current, rate of gas flow, and distance from nozzle tip to plate were analysed. Weld quality was evaluated using criteria such as UTS, yield strength, and % of elongation. The analysis of principal components was utilized to analyse the data and confirm the best parameter configurations. **Rajaravi et al. [48]** investigate the use of Austenitic stainless steel 316 in thermal power plants and automotive components because of its robust resistance to intergranular corrosion and enhanced toughness. The study employed the Taguchi approach to enhance output parameters in TIG welding, with a specific emphasis on input power and welding speed. Research results show that flux welding can reduce angular distortion in weld men by increasing the depth of welding and width aspect ratio and decreasing the HAZ area. **Khrais et al. [49]** analyse the results of Tungsten Inert Gas (TIG) welding on the bead shape, microstructural changes, and appearance of AISI 316 L stainless steel under the impact of three-part shielding gases. Utilizing the Taguchi L-27 method, the study systematically varied the nitrogen (N_2) concentration and helium (H_e) content within the argon (A_r) mixture of shielding gas, with welding current from 120 A to 180 A. The findings revealed that heightened helium and nitrogen concentrations resulted in larger austenite components. Specifically, for TIG welding with a 150 A arc current, the optimal shielding gas mixture comprised 10% He, 2.5% N2, and 87.5% Ar. The augmentation

of nitrogen and helium within the argon shielding gas blend concurrently increased the breadth and depth of the weld profile, ensuring thorough fusion throughout the welding process. **Baskaro et al. [50]** investigated ways to optimize the orbital parameters for pulse current welding with gas tungsten arcs on SS316L stainless steel pipes. The Taguchi method uncovered complex relationships, optimizing tensile strength, and reducing distortion to a minimum. Area plots developed by response surface approach led to 66.5% working cycle, peak current of 114.7 Amp, and a remarkable UTS of 661.4 MPa with minimum distortion. Experiments proved that the model was accurate and gave useful information for enhancing the quality, accuracy, and efficiency of welding. **Neelamegam et al. [51]** aimed to improve the efficiency of the hot-wire TIG (HW-TIG) welding method by increasing heat input and the number of runs. They used response surface methodology (RSM) in the design of experiments (DOE) to minimize trials and determine regression equations for the input variables. The optimal process parameters were identified using the desirability technique and applied to weld 316LN stainless steel joints, which were tested for metallography and tensile strength. The study showed that RSM reduced heat input, enhanced weld quality, and minimized the number of passes required for welding. **Linger and Bogale [52]** studied to improve the mechanical properties of welded seams in 304L stainless steel using L16 experimental analysis. They studied welding parameters such as current, root gap, arc length, and gas flow rate, determining optimal settings with the grey-based Taguchi technique. ANOVA showed that welding current most influenced weld quality, followed by travel speed and root gap. The study achieved an average grey relational grade of 0.863, with peak values of 101.38 HRB for hardness, 1425 MPa for tensile strength, and 1648.6 MPa for bending strength. **Rajput et al. [53]** An investigation was conducted on identical and dissimilar corelation of AISI 316L and AISI 409M using MIG welding with different notch angle root spacing. They conducted a tensile test to examine the strength of weld joints, exhibiting both similarities and differences. The layout of the joining surfaces affects the microstructure and mechanical characteristics. Root gaps of 2 mm with 60° notch angles resulted in strong yield and tensile strength, especially in dissimilar butt-welding joints. **Ghosh et al. [54]** Researchers are investigating the welding of different metals for their flexibility in creating and manufacturing commercial and industrial parts. This study uses GMAW to form dissimilar joint between FSS 409M and ASS 316L. Weld specimens are inspected utilizing

visual and X-ray scanning to detect faults and evaluate the quality of the weld. The data has been examined using the grey-Taguchi methodology. Grey-Taguchi Optimization Technique Determined ideal factor settings: is the C1 F3 S3 setup: 100 A welding current, 10 l/min gas flow, and 9 mm spacing between the nozzle and the plate. ANOVA analysis indicates that flow rate of gas has the maximum impact on joint, whereas plate to nozzle distance has the least impact. In their study, **Mehmood et al. [55]** examine how to optimise the TIG welding process parameters to create a hybrid structure made of aluminium alloy of grade 6061 and stainless steel of grade 304. They achieve this by utilizing an ER-Cu filler rod. The industrial sector relies on welding these materials because of the weight savings and environmental benefits it provides. The result is delicate intermetallic complexes with residual stresses caused by their different melting points and thermal properties. Microhardness and UTS were the response factors, whereas welding speed, current, and flow rate of gas were the input variables. The results indicate that with the increasing of welding current while decreasing the speed improves ultimate tensile strength, whereas increasing the welding speed while decreasing the current reduces micro-hardness. This enhancing the hybrid structure production process, this study optimises the use of each material and finds solutions to integration issues. **Chaudhari et al. [56]** studied the optimal TIG welding parameters for SS 304 of 6-millimetre plates made of mild steel and stainless steel with dimensions of 150 mm × 150 mm × 6mm. The authors utilized Taguchi's method in combination with a L_9 orthogonal array to assess the impact of gas flow rate, voltage, and current on joint hardness. Under optimal circumstances, the Rockwell hardness value achieved was 88.7 HRB, with a current of 150 amperes, a voltage of 22 Volt, and a gas flow rate of 12 litters per minute. In their study **Vora and Badheka [57]** looked at the mechanical properties of 6 mm thick plates of reduced-activation ferritic-martensitic (9Cr-1.4W-0.06Ta / RAFM) steel. They investigated the impact of single and double post-weld heating process cycles on the joints. The TIG welding was done on a 718 nickel-based super alloy with a 2.5 mm thick plate. The welding processes were performed at a range of welding voltages 13 to 15 Volt, currents 44 to 115 Amp, and traveling speeds 67 mm/min. **Sivaprasad and Raman [58]** examined the fatigue performance of TIG weldments under two different heat treatment conditions. **Ambade et al. [59]** investigated the tri-component oxide flux's effect on the weldability of Inconel 718 welding joints. The joints' results show that mixing flux significantly increases

penetration depth compared to conventional TIG welding. In their study, **Wang et al. [60]** discuss the impact of TIG arc welding parameters on various aspects of welded joints, including tensile property, microstructure texture, and fracture nature**.** Initial increases in the tensile strength, yield strength, and elongation of the welded joint lead to a subsequent decline as the welding current increases. With a reduction in welding travel speed and an increase in welding current, the heat input rises. It may cause the welding pool to broaden and deepen, the number of columnar crystals in the seam to decline, and the number of free dendritic crystals to rise. Strength and elongation may decrease with an increase in impulse frequency. The tension fracture nature is ductile, and the dimples disperse across the fracture area. The microstructure and tensile properties combine to optimise process parameters, including welding current, speed, and impulse frequency.

Karadeniz [62] investigated on welding penetration in Erdemir 6842 steel with a 2.5 mm thickness was examined in relation to various welding conditions. In contrast to arc voltage, which had a less significant impact, it was discovered that increasing welding current enhanced the depth of penetration. **Sharma et al. [63]** investigate weld bead geometry has a noteworthy impact on the welded joint's mechanical properties and quality, and is dependent on the input parameter values. **Naik and Reddy [64]** concentrate on optimizing tungsten inert gas welding settings and analysing the tensile strength of 2205 duplex stainless steel by the Taguchi technique and variance analysis. An attempt with orthogonal L_9 design is conducted using the Taguchi approach, aiming to identify issues and minimize errors in the output prediction of a neural network. Factors like current, time, speed, oxide flux variation, diameter of electrode, and flow rate of gas are adjusted to enhance tensile strength, hardness, and weld depth. Applying state-of-the-art statistical approaches. **Tesfaye and Getaneh [65]** investigate a hybrid TIG-MIG welding arrangement to combine the advantageous features of both welding techniques. The study's goal is to find the best way to use TIGMIG hybrid weldment on EN24 mild steel. They tested a 6 mm EN24 mild steel plate, observing its tensile strength and hardness. The study assessed vital process characteristics such as the travel speed of the welding gun, the MIG welding current and voltage, the TIG welding current and voltage. The study found that the best setup for MIG welding is 200 A current with a voltage of 15 Volt; for TIG welding, it is 200 A current with a voltage of 18 Volt; and for the welding gun to travel at a speed of 5 mm/s. The results demonstrate that TIG-MIG hybrid welding

outperforms other methods in terms of hardness and tensile strength, suggesting that the company consider using it to enhance the qualities of their weld joints, specifically their hardness and tensile strength. **Narang et al. [66]** investigated TIG welding process simulation using fuzzy logic was examined. The TIG welding of steel plates with varying thicknesses under various conditions, such as a welding current range of 55 to 95 Amp. and a welding speed of 15 to 45 mm/sec. to prophesy the characteristics of the depth of penetration, weld profile, and bead reinforcement macrostructure zones. In GTAW of dissimilar metals, **Kumar and Mittal [67]** investigated the effects of welding parameters such as welding travel speed, flow rate of gas, and welding current, electrode rod, etc. as inputs that affect the outputs like tensile strength and weld hardness.

Kim et al. [68] studied MATLAB/SIMULINK software to choose the best welding parameters based on multiple regressions and a neural network, this paper creates an intelligent system for GMA welding operations. **Narang et al. [69]** used butt joint welding to examine and forecast the characteristics of the weld bead shape. The mathematical model was created using the Taguchi statistical method, and the ANOVA test was used to determine whether the developed equation was sufficient. By choosing the proper process parameter values as specified by the developed models, weld bead geometry can be predicted with accuracy. **Ghosh et al. [70]** find Taguchi design is used to determine the optimal setting of parameters to achieve the desired quality of a weld. An experimental plan utilizing the Taguchi approach has been implemented. Orthogonal array, S/N ratio, and ANOVA are employed to analyses the welding characteristics of a material and optimize Parameters for welding. **Kumar et al. [71]** Using Taguchi's L_{27} orthogonal, this study determines the optimal process parameters for TIG welding, which include gas flow rate, root gap, voltage, and current. The study indicates that the hardness of the material is influenced by the welding voltage, and decreasing the voltage enhances the welded joint's strength. **Abebe and Bogale [72]** studied to find out the optimal possible welding process parameters to enhance the Rockwell hardness, bending strength, and UTS value of a butt-weld joint by utilizing a TIG torch. The Taguchi design's L_9 orthogonal array and an automated TIG welding setup were used in the experiment. The selected parameters included current, welding speed, voltage, and flow rate of gas. The analysis identified flow rate of gas and current as the most crucial elements. The average multi-response performance index was 0.6068. Rockwell hardness

was 95.3 HRB, and the highest UTS was 614.8 MPa. The highest bending strength was 765.32 MPa. **Omprakasam et al. [73]** The research finds the best settings for TIG welding and the most effective ways to penetrate 5052 metals using Taguchi techniques. To produce an L27 orthogonal array, variables such as welding current, voltage, and travel speed are adjusted. For each weld specimen, the model makes an estimate of its hardness, penetration shape factor, and reinforcing form factor. The ideal setting is 140 A for current, 18 V for voltage, and 300 mm/min for speed. **Esme et al. [74]** conducted an in-depth study to optimize TIG welding for multiple responses, aiming to achieve the desired bead shape in welded joints using the Taguchi method and Grey Relational Analysis (GRA). The experiment involved sixteen trials designed with an orthogonal array from the Taguchi method to strategically define target functions. Key objective functions were selected to focus on critical TIG welding parameters, such as penetration depth, bead geometry (width and height), tensile stress, and HAZ zone width. By combining Taguchi and GRA, the study addressed multi-response optimization. ANOVA was employed to statistically evaluate how various parameters influenced the overall quality of the weldment. The findings, supported by additional research, confirmed improved results, demonstrating the effectiveness of combining GRA with the Taguchi method to enhance product quality in manufacturing. The goal of **Ogbonna et al. [75]** was to make AISI 1008 MS (mild steel) and 316 ASS MIG-welded butt joints work better by using the Grey Taguchi method. They optimised welding parameters like voltage, current, and gas delivery rate using the L_9 Taguchi orthogonal array. They assessed weld joint integrity and determined that the ideal values were 180 amperes, 14 volts, and 19 litters per minute. The most significant process parameter is voltage, accounting for 63.76% of the weldments' total performance. **Bandhu et al. [76]** investigate the Taguchi technique for successfully controlling the metal transfer rate during MIG welding of ASTM 387 low-alloy steel. Analysis revealed that the ideal settings for achieving the desired penetration depth and HAZ were a welding current of 100 Amp., a welding voltage of 16 Volt, and a gas flow rate of 21 litres per minute. **Ahmad and Alam [77]** investigated grey relation analysis to determine the most favourable selection of parameters, with a particular focus on velocity, current, voltage, and penetration depth. To determine the SNR, the study used Taguchi's design of experiments methodology, utilising Minitab18 software. The goal was to improve the manufacturing industry's productivity and weld quality. Gray

relational analysis was employed by **Srirangan and Paulraj [78]** to enhance the tungsten inert arc welding process for Inconel 800HT. The obtained values for yield strength, impact toughness, and ultimate tensile strength were determined in relation to the welding current, voltage, and speed input parameters. By adjusting the parameters with grey relational analysis, the optimal combination of A2B1C2 was attained. Using the ANOVA method, the parameters that influenced the overall quality of the weldment were determined. Inspecting the metallurgical properties validated the mechanical properties. **Bahar et al. [79]** improve the weld bead's hardness and tensile properties by optimising speed, current, and gas flow rate parameters. To achieve this goal, these variables are analysed and optimized. These parameters are used to generate an L9 orthogonal array, which is then used to execute 9 tests. The experiments are tested to see how tough and hard they are. They used MINITAB to look at the hardness and toughness data, and then we improved it with Grey Relational Analysis. The results indicate that larger values for the specified parameters can achieve the ideal hardness and toughness. The flow of gas rate emerges as the most important parameter in this optimisation, as established by the analysis of variance (ANOVA) results. In their investigation, **Abima et al. [80]** used the ANFIS model to guess the maximum tensile strength in TIG-MIG hybrid welding. The model utilizes Taguchi's principles and empirical evidence to design experiments. The model specifies that the parameters with the highest tensile strength must be set to the following values: 25 volts for MIG voltage, 180 Amps for TIG current, and 19 litters per minute for gas flow rate. At 42.35%, the flow rate of gas is the single most important factor influencing ultimate tensile strength. The model attains 99.9% accuracy in training and 96.3% accuracy in testing, with R2-values approaching 1, signifying a robust agreement between experimental and predicted values. The findings indicate that ANFIS models can lower experimental expenses and difficulties linked to trial-and-error techniques, enabling the development and prediction of experimental layouts for various plate thicknesses and associated procedures. **Rajaravi et al. [81]** investigated the several uses of Austenitic stainless steel 316 and found that it did not undergo any post-hardening processes. By optimizing the output parameters using the Taguchi approach, the welding process observed less angular distortion. A method by **Jadhav and Sutar [82]** was used to compare an improvement using the TOPSIS technique between active TIG and standard TIG welding on hot 304L stainless steel plates. **Dahmene et al. [83]** address the issue of

identifying LME cracks. This research used ultrasonic pulse-echo amplitude to develop several NDT methods for fracture identification and characterization (particularly depth estimation). GTAW joint quality on 316L was determined by **Korra and Balasubramanian [84]** by analysing weld bead morphology, specifically width, height, and penetration. Grey through Taguchi analysis, you may optimize input parameters for a wide range of output variables. **Shrivastava and Kumar [85]** analysed GTA welding parameters. Its use reduces distortion in the welds and increases parametric penetration. Based on L_9 Taguchi orthogonal array the optimised values have been used in the experiment. In conclusion, welding speed has a significant impact on distortion caused by gas tungsten arc welding (WS). **Mondal et al. [86]** conduct research on the welding input variables to regulate welding quality. The quality of DSS welding joints is improved by improving TIG welding parameters including current, flow rate of gas, and speed. The Taguchi SNR and PCA are used to optimise these parameters. A second experiment supports the best result. **Chandrasekhar and Vasudevan [87]** developed an intelligent model that combines ANN and GA to find the ideal process parameters for A-TIG welding stainless steels of types 304LN and 316LN. Results from the GA model varied when bead width and target penetration depth were same. **Vinoth et al. [88]** studied TIG welds on 316 stainless steels, controlling parameters such as flow rate of gas, travel speed and welding current. They determined that a welding current of 150 Amperes, a traveling speed of 190 millimetres per minute, and a gas flow rate of 15 litres per minute were the optimal welding parameters. PCGTA with ERNiCrMo-3 filler is studied by **Avinash et al. [89]** in SS 304 and Monel 400. The use of Taguchi analysis in product development leads to better welds in all regards. They investigated the role that various parameters have in determining the resulting welding qualities of the weldment. **Jianming et al. [90]** investigated the MIG welding characteristics of Al 6061 alloy with a L32 Taguchi orthogonal array. The torch angle, wire feed rate, stand of distance, current, and travel speed undergo parametric alterations. Several elements, including rate of wire feed, travel speed, torch angle, and stand of distance, influence the welding current. **Li et al. [91]** examined the impact of hydrogen on 304 L K-TIG weld metal tensile characteristics and failure mechanism. Hydrogen atoms interact with strain-induced martensite to reduce ductility and strength. **Patil and Waghmare [92]** examined welding current, voltage, and speed on AISI 1030 mild steel UTS. Taguchi method is used to investigate and optimize welding

parameters. Welding speed, among other factors, affects tensile strength. Increasing welding scanning speed and reducing current increases the weld's tensile strength. **Reza Tabrizi et al. [93]** investigated the joint properties of AISI 316 L stainless steel as well as how continuous and pulsed current affected GTAW. The microstructure was characterised, and the phase equilibrium was found with optical microscopy, XRD, and FE-SEM with an EBSD detector. The influence of welding current type on joint mechanical properties was studied using Charpy impact, uniaxial tensile, and microhardness tests. After subjecting the material to stress through a tensile test and a Charpy impact, they analysed the fracture surfaces using FE-SEM. They determined the weld metal microstructure to be austenitic-ferritic. During the tensile test, the two joints failed, and the base metal broke. The change in welding current mode resulted in an increase hardness and fracture toughness. The joint fractography results revealed that the fractures were fully ductile in nature. **Sabzi and Dezfuli [94]** conducted a study that examined the microstructural changes, mechanical characteristics, and hot-cracking sensitivity in welded 316 L stainless steel. During the welding process, an increase in electromagnetic vibration leads to a noticeable transformation in the microstructure texture of the weld metal. In particular, the columnar structure transitions into a finely equiaxed dendritic structure, resulting in a reduction in the quantity and size of columnar dendrites. **Mousavi Anijdan et al. [95]** investigated the relationship between the tensile-shear strength of dissimilar joints and variables including welding current density, welding time, electrodes force, and post-welding holding time. Minitab was used to examine the influence of parameters and determine the optimal condition after the trials was designed using the Taguchi method. Scanning electron microscopy was used to examine the microscopic structure under ideal conditions (SEM). A lap shear test was used to evaluate the weld's durability. The optical microscope was used to analyse the fracture mode.

Researchers **Sabzi et al. [96]** looked at how changing the pulse current of (PCGTAW) Pulsed Current GTAW affected the result in terms of the properties of dissimilar welding between AISI SS 316 L and AISI SS 310. They analysed the microstructural development in different areas of the welded joints using microscopy by optical and field-emitted scanning electron microscopy techniques. Charpy impact, Tensile, and Vickers microhardness tests also measured the changes in mechanical properties caused by the pulsed current. Finally, they performed FE-SEM analysis on the fracture surfaces areas of the Charpy impact and

tensile test samples. The surface fractography for both the tensile and Charpy impact tests revealed a totally ductile fracture. An improved welding process was identified utilizing a Taguchi-based hybrid grey-based technique. Many weld quality variables were considered while determining the optimal welding process parameters for submerged arc welding by **Tarng et al. [97]** using grey-based Taguchi methods. **Murugan and Parmer [98]** used the Taguchi technique to design, analyse, and find the best possible TIG welding process control parameters. They did this to investigate how current, gas flow rate, and travel speed affect TIG welding of ferritic AISI 409M stainless steel. The Taguchi experimental strategy has been implemented to identify the optimum parameter combination for better weld quality. Ocular inspection and X-rays of weld samples were also used to evaluate the weld quality. **Sakthivel et al. [99]** made welding parts out of 316L (N) Austenitic stainless steel using both activated TIG (A-TIG) and standard TIG (MP-TIG) methods. Their welding process employs both single-pass and multi-pass techniques. The study examined the creep breach action in the two cases. In both welding joints, lower levels of creep fractures were seen.

A comparison study between TIG welding and other welding techniques

Shanmugam et al. [100] investigated the influence of SMAW, GMAW, and GTAW processes on the mechanical properties and microstructure of AISI 409M FSS weldments. GTAW weldments demonstrated superior tensile strength, impact toughness, and hardness compared to SMAW and GMAW. Microstructural analysis revealed predominantly dendritic austenite structures in all weldments. **Balasubramanian et al. [101]** compared the fatigue crack growth behaviour of ASTM 517 'F' grade steel weldments using SMAW and FCAW processes. Results showed that SMAW welded joints provided better resistance to fatigue crack growth than FCAW welded joints. **Ericsson et al. [102]** investigated the effect of welding speed on the fatigue strength of FSW welds, comparing them to TIG and MIG welds of Al-Mg-Si 6082 alloy. The study concluded that FSW welds exhibit superior fatigue strength compared to TIG and MIG welds. **Bendikiene et al. [103]** compared the microstructure and strength of GMAW and SMAW weld joints in non-alloy S235JR structural steel. The study aimed to assess the influence of grain structure on mechanical properties, concluding that GMAW joints, with finer grains, exhibit superior mechanical properties compared to SMAW joints. **Karthik et al. [104]** aimed to compare the TIG and SMAW welding processes based on the microstructure and mechanical properties of AISI

304 SS weldments. The study concluded that TIG weldments exhibit higher tensile strength compared to SMAW weldments. **Jorge et al. [105]** investigated the impact of GMAW and SMAW methods, along with post-weld heat treatment, on the mechanical properties of High-strength low-alloy steel joints. The specimens were multi-pass welded at a preheat temperature of 200°C. The study focused on various input parameters, including current, deposition rate, voltage, welding energy, and the number of passes. GMAW used a shielding gas mixture of Ar-CO_2 in a 4:1 ratio, while ER120S-G wire rods and E12018-M rods were employed as filler metals for GMAW and SMAW, respectively. To assess the soundness of the welded joints, magnetic particle and ultrasound inspection tests were performed. Metallographic analysis, including optical microscopy, SEM, and EBSD, was conducted to examine the microstructure. The presence of carbides resulting from PWHT was evaluated using Thermo-calc software. The study found that while PWHT generally reduces mechanical properties, particularly ultimate tensile strength (UTS), GMAW demonstrated a higher deposition rate than SMAW, offering a significant productivity advantage for welding High-strength low-alloy steel. **Shah et al**. **[106]** compared the effects of aluminum filler ER5356 and stainless-steel filler E308LSi on the microstructure and mechanical properties of MIG-welded dissimilar joints between aluminum alloy AA6061 and stainless steel SUS304. The choice of filler metal was found to significantly impact the weld joint properties. Welding and analyzing the microstructure of dissimilar metals is challenging due to their differing physical properties and the need for different etching solutions. The experimental results indicated that welds made with aluminum filler wire exhibited superior tensile strength but lower hardness compared to those made with stainless steel filler. **Zhen et al. [107]** compared the TIG and FSW welding processes by examining the microstructure and mechanical properties of Al-Mg-Mn-Sc-Zr alloy plates in both hot-rolled and cold-rolled annealed conditions. In TIG welding, Al-Mg-Sc-Zr alloy wire was used along with argon shielding gas. Microstructural analysis was performed using TEM. The results showed that FSW joints offered better tensile properties and a higher welding coefficient than TIG joints. Furthermore, the weld nugget zone in FSW joints exhibited finer grains and greater hardness compared to the TIG weld seam. **Yeni et al. [108]** conducted a comparative study on the MIG, TIG, and FSW processes, examining the microstructure and mechanical properties of 6 mm thick 7075 aluminium alloy welds. In the MIG and TIG welding processes, AA 5356

and AA 4043 were used as filler metals, respectively. To enhance penetration, the specimens were preheated to approximately 150°C before welding. Input parameters, such as current, shielding gas, voltage, welding speed, and gas flow rate, were carefully controlled during the MIG and TIG processes. Microstructural analysis using an optical microscope revealed that the nugget zone in FSW welds consisted of fine, recrystallized equiaxed grains. In contrast, coarse grains were observed in the weld and heat-affected zones of MIG and TIG welds, primarily due to the higher heat input associated with these processes. The mechanical properties of FSW joints were found to be superior compared to those of MIG and TIG joints.

The research gaps in TIG welding of austenitic and ferritic stainless steels, both for similar and dissimilar welding, include a lack of comprehensive studies examining the combined effects of input parameters on mechanical properties such as tensile strength, hardness, yield strength, and elongation. In dissimilar welding, challenges like metallurgical incompatibility, residual stresses, and brittle phase formation remain inadequately addressed. There is also insufficient focus on microstructural analysis to understand the influence of welding parameters on weld zone and heat-affected zone properties. Additionally, advanced optimization techniques for process parameter selection and understanding heat input and fusion characteristics require further exploration to improve weld quality and minimize defects. These gaps highlight the need for integrated experimental and computational approaches to advance TIG welding research.

The novelty of TIG welding lies in its unique combination of precise heat control, high-quality welds, and versatility. Below discussed the different points.

Precise Heat Control: TIG welding allows for fine control over heat input, which is essential for welding thin materials and preventing distortion. The ability to adjust both the welding current and arc length enables more accurate control over the welding process.

Clean, Contaminant-Free Welds: The use of an inert gas (usually argon) protects the weld pool from atmospheric contamination, resulting in clean, high-quality welds without the need for flux.

Diverse Material Compatibility: TIG welding can weld a wide variety of metals, including ferrous and non-ferrous materials like stainless steel, aluminum, and titanium, which makes it versatile across many industries.

Superior Weld Quality*:* The technique produces strong, visually appealing, and precise welds with minimal spatter or post-weld cleaning, which is highly beneficial for applications requiring aesthetic quality and integrity.

Adaptability in Hybrid Welding*:* The introduction of hybrid welding techniques, like combining TIG with other processes (e.g., MIG or laser welding), has increased the efficiency and application of TIG welding in industries demanding high-quality and complex joints.

1.6 Objectives of the Present Dissertation

The present research intends to investigate the effects of input parameters on features of geometry of the bead profile (penetration depth and bead width) and mechanical properties (UTS, % of elongation and microhardness) of 409M FSS and 304L ASS based similar and dissimilar weldment fabricated through GTA welding.

Based on three input parameters such as welding current welding, speed and flow rate of gas, experiments were carried out based on Taguchi L_9 orthogonal array design of experiments. X-ray based visual inspection was performed first to study various surface / subsurface flaws: if it exists. The research also aims to attempt GRA and TOPSIS methodologies integrated with Taguchi method to determine an optimal setting of process parameters in purview of measurable estimates of bead geometry, microhardness, and tensile strength of the weldment. The present research also focused a novel attempt to join incompatible material (Ferritic to Austenitic steels) which is of immense important in industrial contest.

Specific objectives of the present dissertation are stated out below.

1. To study effects of GTA welding parameters (welding current, scanning speed and flow rate gas) on bead geometry, microhardness, and tensile properties of the dissimilar weldment.
2. To study the appearance of the deposited beads through visual inspections followed by detailed microstructural (HAZ and FZ) analysis to be carried through optical microscopy and SEM (scanning electron microscopy).
3. To corelate microstructural features with tensile properties of the specimen weldment.

4. To determine and optimal setting of welding parameters to satisfy multiple requirements of the weld quality simultaneously. GRA and TOPSIS based Taguchi optimization model is intended to be attempted to solve such a multi-objective optimization problem. The multi - objective optimization is defined herein in such a way that the optimal setting can simultaneously minimise bead width, maximise penetration depth and maximise weld tensile strength.

The work is to be carried out in the present dissertation is believed to have great industrial relevance in the following aspects.

Material Compatibility: The work would help to understand and explore to understand and explore advantages of dissimilar TIG welding on emphasising suitability of dissimilar materials with varied composition, thermal characteristics, and metallurgical features.

Optimizing Welding Parameters: The work would help to achieve robust, defect-free joints between Ferritic and Austenitic stainless steels, it is necessary to optimize important welding parameters such as weld current, scanning speed, and gas flow rates.

Mechanical Properties Evaluation: The research would help to assesses the mechanical characteristics such as tensile strength, micro hardness, to determine their performance and integrity of similar and dissimilar TIG-weld joints.

Investigate the Changes in Microstructure: This study aims to provide a subtle understanding of its potential for the development of various phases during the welding process. To achieve this, it is crucial to analyse the microstructural changes that occur in different regions of the welded joint. Specifically, the fusion zone, where the base metal melts and solidifies, often exhibits significant microstructural transformations influenced by the heat input and cooling rate. The heat-affected zone (HAZ), which experiences thermal cycles without melting, is another critical region where microstructural modifications such as grain growth, phase transformations, and residual stress development can occur. Additionally, the interface between ferritic and austenitic stainless steels—commonly referred to as the "usable interface"—requires particular attention. This area often experiences complex metallurgical interactions due to the differing thermal and chemical properties of the two steel types. Understanding these microstructural changes is essential for optimizing welding parameters,

improving joint performance, and minimizing defects such as phase imbalances, cracking, or reduced corrosion resistance.

This chapter provides an overview of the study and the methodologies used in the research process. This chapter also covers the hypothesis, objective, and scope of the investigation, and discusses many optimization tools and techniques, including GRA and TOPSIS.

2.1 Design of Experiment and Optimization Tools

2.1.1 Research Methodology

This content discusses the optimisation strategies that were chosen and employed in the current study. The purpose is to emphasise the fundamental approach used in each of these approaches.

Hypothesis

The research hypothesis of this study indicates that the welding current, flow rate of gas, and travel speed in TIG welding have a positive impact on the performance of the welding process. For test hypothesis the following steps are follow

1.   Identify the criteria that are used to assess the effectiveness of each optimisation method.

2.   Create experimental designs to evaluate and compare the efficacy of each optimisation approach.

3.   Apply the Grey Taguchi and TOPSIS methodologies to the same dataset(s) and collect the results of each one.

4.   Evaluate the outcomes a result of each method according to the specified metrics. Evaluate the effectiveness of Grey Taguchi and TOPSIS in identifying key factors.

5.   ANOVA is used to determine if there are any significant differences in the performance of the optimisation approaches.

2.1.2 Optimization Technique used in Present Research

2.1.2.1 Taguchi Method

Dr. Genichi Taguchi, a renowned Japanese scientist, established the Taguchi technique. The Taguchi design of experiments offers a streamlined and methodical approach to enhancing

designs in terms of performance, quality, and cost. Several engineering disciplines extensively use the Taguchi technique to optimise production methods and systems. It is a crucial tool for building efficient systems or processes with little expense. The Taguchi technique is a statistical approach that utilises orthogonal array experiments. It aims to create a balanced design by assigning equal importance to all components while minimizing the number of experimental runs required. Thus, the implementation of the Taguchi method's orthogonal array significantly reduces both costs and experimental time. The signal-to-noise ratio (SNR) is a statistical performance measure that the Taguchi approach uses to determine the importance of process parameters. This ratio considers both the average value and the variability of the data. The SNR is defined as the ratio of the average signal to the standard deviation of the noise. The ratio is determined by the quality attributes of the product or process being optimised. Often used SNR (signal to noise ratio) include NB (nominal-is-best), LB (lowest-is-best), HB and (highest-is-best) [109, 110]. Figure 2 is a flow diagram depicting Taguchi's approach to the optimisation problem.
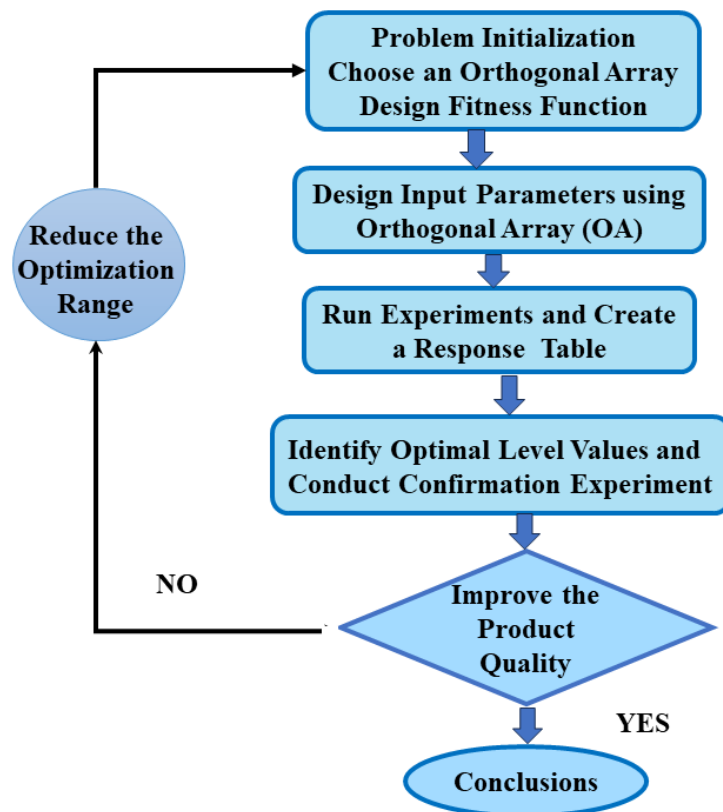

Figure 2.1 Flowchart of the suggested Taguchi's approach

Taguchi's SNR for NB (Nominal-is-best)

$$\eta = 10 \ln_{10} \frac{1}{n} \sum_{i=1}^{n} \frac{\mu^2}{\sigma^2} \quad \text{---------------- 2.1}$$

Taguchi's SNR for LB (Lowest-is-best)

$$\eta = -10 \ln_{10} \frac{1}{n} \sum_{i=1}^{n} y_i^2 \quad \text{---------------- 2.2}$$

Taguchi's SNR for HB (Highest-is-best)

$$\eta = -10 \ln_{10} \frac{1}{n} \sum_{i=1}^{n} \frac{1}{y_i^2} \quad \text{---------------- 2.3}$$

where n = experiment times

y_i= experimental value

η = SNR (signal to noise ratio)

μ = Standard Mean

σ = Standard Deviation

2.1.2.2 Grey Relational Analysis

The grey relation theory, introduced by Professor D. Julong in the year 1982, has shown its utility in handling inadequate, fragmented, and ambiguous information. Grey relational analysis, which is grounded on the principles of grey system theory, is a powerful tool for efficiently addressing complex interdependencies across numerous performance criteria. However, in grey analysis, the data must be pre-processed into quantitative indices to standardise the raw data for analysis. By drawing on insights from grey system theory, grey relational analysis provides insights into the intricate linkages between various performance metrics. Adjusting raw data for analysis in grey analysis calls for quantitative indices. The grey relational analysis scales experimental data on product quality from 0 to 1. The effectiveness of a multiple response procedure is based on its relational grey grade. Equations 2.4 is used to compute the grey relational creating normalized data for the higher-the-better (HB) criterion.

$$x_i(k) = \frac{y_i(k) - \min y_i(k)}{\max y_i(k) - \min y_i(k)} \quad \text{---------------- 2.4}$$

Equations 2.5 is used to determine the grey relational creating normalized data for the lower-the-better (LB) criterion.

$$x_i(k) = \frac{\max y_i(k) - y_i(k)}{\max y_i(k) - \min y_i(k)} \text{----------------- 2.5}$$

The generated sequence, $x_i(k)$, is the value obtained after grey relational generation. The ideal sequence, $x_0(k)$, represents the optimal or ideal values for the responses. The minimum value of $y_i(k)$ for the k_{th} response is denoted as $\min y_i(k)$, while the maximum value of $y_i(k)$ is denoted as $\max y_i(k)$. By using the grey relational grade, engineers and researchers can evaluate the effectiveness of a particular process or design. For example, in manufacturing, GRA has been used to optimize the parameters of a production process to achieve the desired outcomes.

The grey relation coefficient $\xi i(k)$ has computed as

$$\xi_i(k) = \frac{\min \Delta_i(k) - \zeta \max \Delta_i(k)}{\Delta_i(k) - \zeta \max \Delta_i(k)} \text{---------------- 2.6}$$

where $\Delta_{oi} = \|x_0 \text{-} x_i(k)\|$ disparity in the absolute values $x_0(k)$ and $x_i(k)$; θ is the differentiating coefficient $0 \leq \theta \leq 1$; $\Delta_{min} = \forall_j^{min} \text{-} t \forall k^{min} \|x_0(k) \text{-} x_j(k)\| =$ the minimum value of Δ_{0i} ; and $\Delta_{max} = \forall_j^{min} \text{-} t \forall k^{min} \|x_0(k) \text{-} x_j(k)\| =$ maximum value of Δ_{0i}.

The variables x_i and x_0, which is also referred to as the GRG in comparative sequence analysis, are being considered. Additionally, the term $\Delta_{oi}(k)$ represents the absolute difference between $x_0(k)$ and $x_i(k)$. The grey relational grade γ_i may be determined by calculating the mean of the grey relation coefficients.

$$\gamma_i = \frac{1}{n} \sum_{k=1}^{n} \xi_i(k) \text{---------------- 2.7}$$

where, n = total responses quantity

A higher GRG value assemble with the significant relational degree among the reference sequence $x_0(k)$ and the specified sequence $x_i(k)$. The reference sequence $x_0(k)$ signifies the optimal sequence process.

The Taguchi L_9 method has been used in this experimental investigation owing to its dependability in optimising results and its less susceptibility to failure or variation. Taguchi L_9 orthogonal arrays are mostly used in fewer experiments than other traditional experimental designs. It is also efficient to explore many parameters with a minimum number of experimental trials, and it takes less time.

Taguchi's SNR is a statistical tool used in experimental research for collecting mean performance and system variability data. It is very easy to understand how factors effect on quality.

2.1.2.3 TOPSIS

TOPSIS is recognised as a very successful (MCDM) Multi-Criteria Decision-Making approach because of its special qualities. These traits contribute to its high level of consistency and require minimal computational work. This method consolidates the multi-response values to produce a single performance response value. The aim of the TOPSIS technique is to establish a ranking that closely matches the perfect solution. An ideal solution is a theoretical solution that maximizes the advantages and minimises the drawbacks of characteristics or alternatives. Alternatively, the negative (-ve) ideal solution is a hypothetical approach that would raise the expenses associated with the features or criteria while reducing their advantages. As a result, the best option for solving the problem is the one that minimizes the negative (-ve) ideal solution and is farthest from the negative one. The Euclidean Distance or Geometric Distance is used to represent the similarity or difference between two entities. The ideal solution and the negative ideal are determined by analysing the maximum and minimum values in the database. This technique allows for trade-offs across criteria by evaluating the possibility of neglecting poor outcomes in one criterion in favour of excellent results in another criterion. This method uses a more realistic modelling [111, 112].

In every Multiple Criteria Decision Making (MCDM) situation, a decision matrix of size m × n is used. The matrix consists of m alternatives and n criteria.

$$X = \begin{vmatrix} x_{11} & x_{12} & x_{1n} \\ x_{21} & .. & x_{2n} \\ x_{31} & .. & x_{3n} \end{vmatrix}_{m \times n} \quad \text{---------------- 2.8}$$

For all equations in this section, the variables i range from 1 to m, while the variables j range from 1 to n. The problem can involve a vector for criteria weights, defined as W = (w$_1$, ..., w$_n$), which must satisfy to the given mathematical equation no 2.9

$$\sum_{j=i}^{n} w_j = 1 \quad \text{---------- 2.9}$$

Figure 2.2 and the accompanying description outline the six primary processes of selecting the optimal option using the TOPSIS approach.
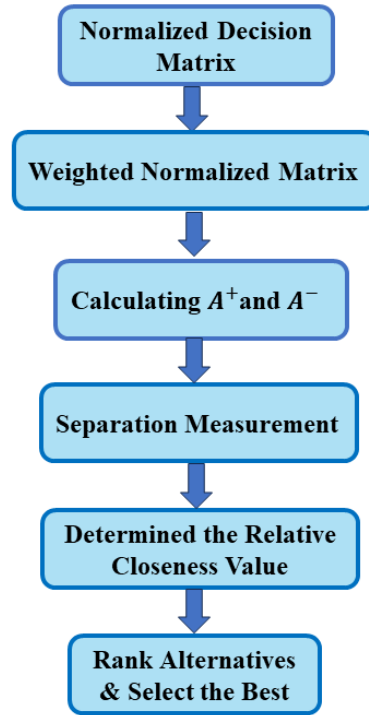

Figure 2.1 Procedures for the TOPSIS technique

I. *Normalizing the Decision Matrix*

This equation is used in this method to convert different units in the chosen matrix into dimensionless equivalent units. As an example, the vector normalisation technique's normalised values for each x_{ij} in the decision matrix are shown as follows:

$$r_{ij} = \frac{x_{ij}}{\sqrt{\Sigma_{i=1}^{m} x_{yij^2}}} \text{---------- } 2.10$$

II. *Construction of Weighted Normalized Decision Matrix*

Each element of the normalised decision matrix has been multiplied by the criterion-corresponding weight. Here is the formula for calculating the weighted normalised decision matrix (V):

$$V = \left(v_{ij}\right)_{n \times m} \text{---------- } 2.11 \qquad \text{Where } v_{ij} = w_j r_{ij}$$

III. Determination of (+ve) Positive Ideal Solution and (-ve) Negative Ideal Solution:

The +**ve** ideal solution, commonly referred to as Zenith (A*), is the optimal performance for each normalised criteria, characterised by the highest value for each criterion. On the other hand, the -ve ideal solution, sometimes referred to as Nadir or anti-ideal (A-), shows the worst performance, consisting of the lowest value for each criterion.

$$A^* = \{1, 1…..,1\}$$
$$A^- = \{0,0 ….,0\}$$

Additionally, the subsequent equations are suggested for deriving ideal solutions that are both negative and positive.

$$A^* = \{v_1^*, v_2^*, … v_n^*\} = \{(\,^{max}_j v_{ij}|\ i\ \in I'), \{(\,^{min}_j v_{ij}|\ i\ \in I'')\} ---------- 2.12$$

$$A^- = \{v_1^-, v_2^-, … v_n^-\} = \{(\,^{min}_j v_{ij}|\ i\ \in I'), \{(\,^{max}_j v_{ij}|\ i\ \in I'')\} --------- 2.13$$

The equations indicate that the A^* value is derived by selecting the highest possible performances from V, whereas A^- is obtained from the lowest possible performances of the normalised matrix [104].

IV. Calculation of Distance Measures

Determine the Euclidean distance between every alternative and the best possible positive outcome (A^*) as well as the negative ideal outcome (A^-).

$$D_i^* = \sqrt{\sum_{J=1}^n \left(v_{i,j} - v_J^*\right)^2} ---------- 2.14$$

$$D_i^- = \sqrt{\sum_{J=1}^n \left(v_{i,j} - v_J^-\right)^2} --------- 2.15$$

V. Determining the Relatively Proximity

The following formula calculates the proximity factor, which has a range of 0 to 1.

$$C_i^* = \frac{D_i^-}{D_i^+ \mp D_i^-} ---------- 2.16$$

VI. Ranking of Alternatives:

Ultimately, the options are ranked according to their similarity rankings. The alternative having a highest (C_1^*) close to1 similarity score has been considered as the optimal choice.

TOPSIS is often used in situations where decision-making requires the simultaneous consideration of numerous factors. The technique offers decision-makers a methodical and

unbiased way to assess and prioritise options, considering their performance across many criteria [113].

2.2 ANOVA

ANOVA, a collection of statistical models, divides variability into systematic and random components to investigate differences between the means of two independent variables. It consistently yields the best results when applied to static interference [114].

ANOVA

In an experiment with several interventions or levels of a single factor, "n" observations are obtained for each level. The variable Y_{ij} represents the Jth observation taken under the ith factor level, whereas y_{io} reflects the overall number of observations under the ith intervention.

$\bar{y}_i$ represents the average of the observation under the ith intervention.

$\bar{y}$ represents the mean of all observations

Now the total sum of square is given by

$$ss_T = \sum_{i=1}^{k} \sum_{j=1}^{n} (y_{iJ} - \bar{y})^2 \text{ ---------- 2.17}$$

This variation usually divided in two different categories such as between group variation another is within group variation.

This can be written as

$$ss_T = ss_B + ss_w \text{ ---------- 2.18}$$

That means total sum of square = Sum of squares between groups + with in group sum of squares.

The idea of degrees of freedom generally describes the number of independent variables that are allowed to variation. When analysing variances or sums of squares, it is important to note that the total of deviations always equals zero. Therefore, if there is information about all the previous deviations, then can easily determine the value of the final deviation. If we have a total of n deviations, it is important to understand that only n - 1 of them have the freedom to vary.

SS_T = N observation to the total mean, now degrees of freedom is N-1

SS_B = k refers to overall mean, now degree of freedom is k-1

SS_W = N observation to k samples, so degree of freedom is N-k

Sums of square $= df_T = df_B + df_\omega$ ---------- 2.19

Mean of square $= Ms_B = \frac{ss_B}{(k-1)}$ and $Ms_w = \frac{ss_w}{(N-k)}$ ---------- 2.20

ANOVA is used to ascertain the significance of a model. If the P value is ≤ (less then equal) the chosen α value (confidence level) of 90% or above, then the model is deemed statistically significant. If the P value is greater than the α value, the model is considered non-significant [115,116]

In the present work, it is assumed that all responses features (bead width, UTS and microhardness) are equally important. Hence equal priority weightage was assigned to each of the responses. The corresponding domain of input parameters as suggested by the earlier researchers is given below.

Author's	Technique Used	Objective	Input Parameter Ranges
Rojas, et al. [117]	GRA, ANOVA	Optimize mechanical properties of Al-6061 T6 alloy.	Current:160-200 A; Voltage: 16-20 V; Gas Flow: 8-12 L/min
Wang and Chen [118]	GRA, TOPSIS	Maximize strength in TIG welding of magnesium alloys.	Current: 50-90 A, Voltage: 14-18 V, Gas Flow: 6-10 L/min
Ghosh [119]	GRA	Parametric optimization.	Current 100-124 A, gas flow rate 10-20 l/min, nozzle to plate distance 9-15 mm
Srirangan et al. [120]	TOPSIS	Optimize input process parameters using the TOPSIS technique to achieve desirable and acceptable mechanical properties.	Current 110 A, Voltage 10 V, and welding speed of 1.5 mm/sec.
Chellappan et al. [121]	TOPSIS	Analyse the influence of TIG welding parameters on bead geometry and hardness.	Current 140 -180 A, Voltage 14-18 V, Travel speed 55-75 mm/min, Gas flow rate 12- 16 *l*pm

Chapter 3 outline will provide extensive information about the experimental planning, procedure, and setup of the experiments. In addition, it included an in-depth discussion of the many numbers of equipment used in this investigation, such as the welding machine, milling machine, Instron machine, microhardness tester, optical and Scanning Electron Microscopy microscope, and so on.

3.1 Experimental Methodology

TIG welding was performed on FSS 409M and ASS 304L, in addition to dissimilar welding ASS 304L and FSS 409M. The previous section defined the scope and aim of the present investigation. The parameters that have the most influence on this experiment are process characteristics like as weld current, travel speed and flow rate of gas. By utilizing the Taguchi method and TOPSIS, the most effective combination of parameters for achieving the good quality of the weld joint has been determined. Additionally, tensile and microhardness tests were conducted as part of this study. Additionally, optical microstructure analysis, scanning electron microscopy (SEM) analysis for evaluate the welded joint's grain structure, phase transformation, dislocation behaviour etc, and weld bead width and depth will be performed. This chapter presents the results and a discussion.

3.1.1 Materials Selection for Experimentation

For this experiment, a thickness of three millimetres has been chosen for both ASS 304L FSS 409M. The samples, which are three millimetres thick, are butt-welded utilizing Tungsten inert gas welding without any edge preparation being performed. ER 308L stainless steel filler wire with a diameter of 1.6 centimetres has been selected for welding. The filler rod and base material, as well as their chemical composition, are shown in Table 3.1.

Table 3.1: Base and filler materials chemical percentage

Base materials	C	Mn	Si	S	P	Cr	Ni	Mo	Ti	Fe
ASS 304L	0.028	1.52	0.60	0.02	0.040	18.45	8.12	0.05	----	Bal.
FSS 409M	0.028	1.17	0.45	0.02	0.058	11.0	0.4	----	0.008	Bal.
Filler (ER308L)	0.030	1.54	0.65	0.030	0.045	19.20	8.68	0.02	----	Bal.

According to the experimental designs suggested by Taguchi, the first set of testing included butt welding 304L ASS together. In the second series of testing, the Taguchi designs were used to weld 409M FSS with 308L filler wire. ASS 304L and FSS 409M were subjected to dissimilar welding in the third set of investigations. The experimental design used was the Taguchi L_9 design. Based on the face-centred central composite design of the experiment and the Taguchi L_9 Orthogonal Array design of the experiment, three different levels of current, gas flow rate, and travel speed have been chosen for the experiment. The current work defines the execution of tests in a planned sequence, known as the design of experiments. To create the experiment, a face cantered central composite design was used. The input parameters for consideration are the welding current, travel speed, and flow rate of gas. Each of these parameters is evaluated at three different levels. The input parameters values have been chosen using a combination of literature research and experimental trials. Table 3.2 displays the design matrix.

After the experiments, the welded samples pass a visual inspection, followed by an X-ray radiography test. Subsequently, specimens are derived from the welded samples for the purpose of conducting both tensile tests and Vickers microhardness tests. Much more detail about them has been addressed in later parts. Another series of tests is conducted using a well-designed experimental sequence. The Taguchi L_9 orthogonal array design is used as the experimental design. The input parameters for the study are chosen as welding current, gas flow rate, and travel speed. Each parameter is examined at three different levels. Table 3.3 displays the welding design matrix that is derived from the Taguchi L_9 orthogonal array design.

3.1.2 Experimental Setup and Procedure

The photographs of different equipment had been used in the present work are shown in the subsequent articles.

I. *Milling machine:* A milling machine is used for cutting a specific amount of strip from a welded sample to create microhardness and tensile samples. The milling machine's specifications are provided in below, and a photographic picture of the milling machine utilized in the study is shown in Figure 3.1.
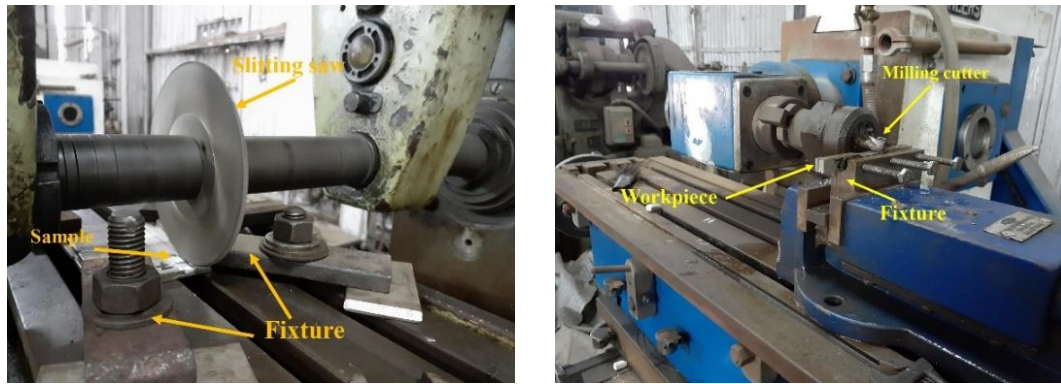
Figure 3.1 Milling machine for preparing welding samples

Type	Universal Milling Machine
Maker Name	B. S. Machine Tools Corporation
Serial Number	222484

II. **Welding machine:** For these experimental purposes, a TIG welding machine was used. Figure 3.2 shows a pictorial setup of a mechanized gas tungsten arc welding machine.
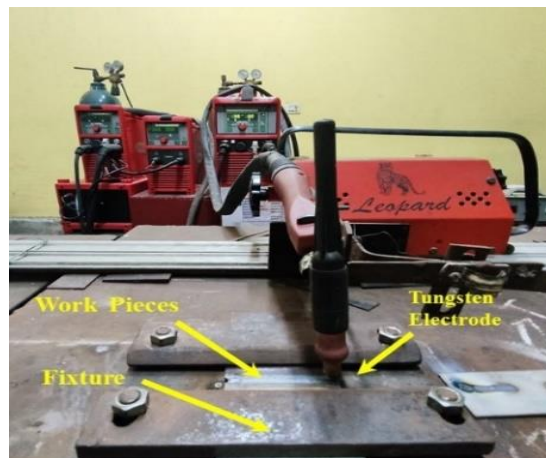

Figure 3.2 Welding set-up

Brand and Model	Fronius; Magic Wave 2500 TIG Welding Machine
Voltage and Frequency	220Volt and 50Hz
Automatic Grade	Semi-Automatic
Phase and Working voltage	3 Phase and 10.1-20.0 V

III. **Radiography equipment:** X-ray radiography examinations were conducted at SKB Metallurgical Services, situated in Salkia, Howrah, West Bengal. The instruments used for this purpose have the following main specifications:

Equipment and Source	XXQ-2005; X-ray
Voltage and Current	120 kV; 5 mV
Film	LASER NDT-7
Sensitivity and SOD	< 2% and 28"
Screen	0.15 mm (both)
Technique	S.W.S.I.
IQI	ASTM-1A
Exposure time	30 Sec
Processing temperature	200C

IV. ***Instron universal testing machine:*** Tensile tests were conducted using an Instron universal testing equipment in the mechanical laboratory of the Variable Energy Cyclotron Centre (VECC). The machine's major specifications are shown below. Figure 3.3 presents a pictorial image of the machine.
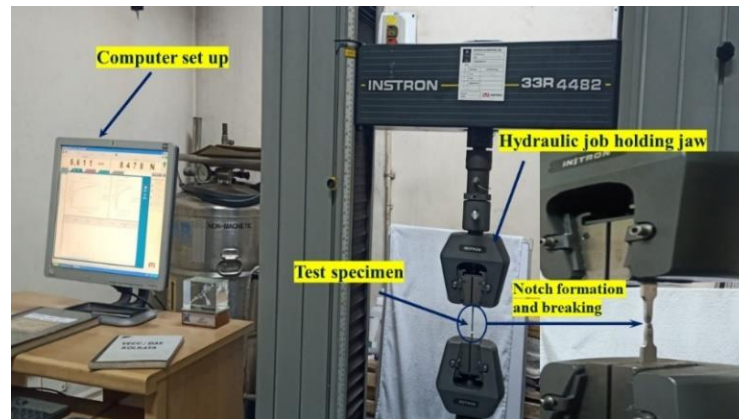
Figure 3.3 Universal testing machine (UTM)

Model and Load	Instron 4482, 100 kN
Max. speed and Min. speed	500 and 0.001 millimetre per minute
Max. force at full speed	75 kN
Max. speed at full force	250 millimetre per minute
Position measurement precision	± 0.10 mm or 0.15%
Return speed	600 millimetre per minute
Position control resolution	0.006 µm
Crosshead speed accuracy	$\pm$ 0.10 mm or 0.15% of displacement

V. *Polishing machine:* To facilitate the metallurgical analysis, all the welded samples were cut into the dimensions that were needed. After the cutting process, all samples undergo polishing using emery paper of varying grades. A LECO polishing machine have been used for the final polishing. Below is an image of the machine.

Figure 3.4 Auto polishing machine

VI. *Metallurgical optical microscope:* The Leica metallurgical microscope is used in this investigation to examine the microstructures of the welded samples. Description of machine specification are bellow. Figure 3.5 shows a photographic representation of a metallurgical microscope.

Figure 3.5 Metallurgical microscope

Model	Leica DMILM, 3 gears focusing mode
Incident light and Transmitted light	Reflector turrets at 4x and 5x on the light axis; 12 Volt, 100 W halogen
Power	12 Volt - 100 Watt, freq 50 - 60 Hz

VII. **Microhardness Tester:** The Microhardness Tester has been used to measure the hardness at different points of the weldment. Figure 3.6 depicts a UHLVMHT MOT micro-hardness tester, along with the machine's specifications.

Figure 3.6 Micro hardness testing machine

Model and Software	VMH-002V/1903001; IMS-VHMT
Zoom	10x – 50x
Indentation load	10 gf – 2000 gf

VIII. **Scanning Electron Microscopes (SEM):** SEM have been used to characterize the morphology, grains size, and distribution of particles, or other features within a welded sample. Figure 3.7 image of SEM machine and specifications of machine are given bellow.
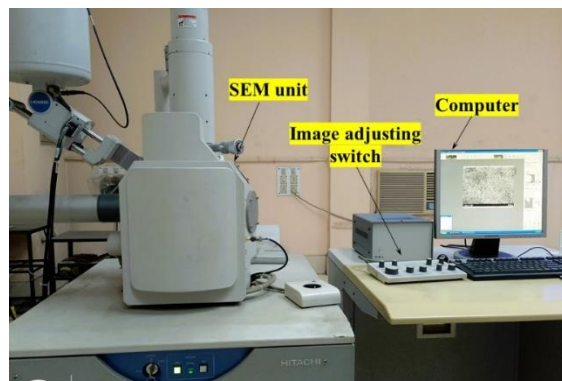
Figure 3.7 Scanning electron microscope (SEM) machine

Maker and Model	HITACHI and S-3400N
Secondary Electron Resolution	3.0 nm
Magnification	×5 to ×300,000 (magnification of image)
Accelerating Voltage	0.3 kV to 30 kV
Motor Drive	5-axis motor drive

IX. ***Stereo and Zoom Microscopes:*** This optical instrument, known as a zoom microscope, is used to analyse the weld bead profile. The weld region's width and depth are also measured by it. Figure 3.8 the pictorial view of this instrument is given bellow.
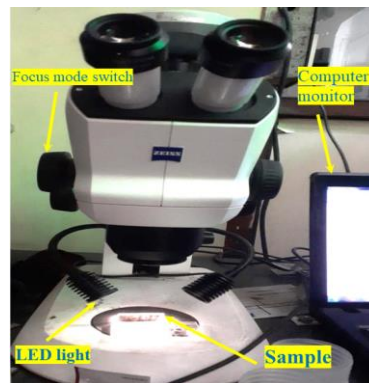
Figure 3.8 Stereo Microscopes

3.1.3 Experimental Procedure, Inspection, and Testing

In this present experimental work three sets of experiments have been carried out based on Taguchi L_9 designed, 3 mm thick rolled sheet are cut into the size of 60 mm × 100 mm. For this work 1.6 mm diameter filler wear has been used. The chemical compositions of the filler and base material are discussed earlier in table 1.

A rolled sheet of stainless steel (AISI 304L) was used as the workpiece material, and (ER308L) was used as the filler material. The schematic diagram of welded sample is shown in Figure 1. A stainless-steel soft wire brush with acetone is used to clean all plates. No edge preparation or grooving is necessary due to the plate's 3mm thickness.

Three sets of experiments were conducted using the L_9 orthogonal array, which was chosen based on three variables, each with three levels. The input factors considered in this study were current, flow rate of gas, and travel speed. Based on trial-and-error welding, the

appropriate parametric domain has been selected. During trial experiments, weld quality (bead geometry and defects) has been examined. The selected parametric domain ensures satisfactory quality bead without any major flaws detected through trial experiments. Table 3.2 presents a comprehensive list of the variables and their respective concentrations that were used in the studies. The welding parameters that have been almost same in all nine trials. The design of the experiment matrix for each component is shown in Table 3.3. Figure 3.5 displays a visual representation of one of the welded specimens.

Table 3.2: Parameters of the process and their levels

Process Parameters	Unit	Symbols	Level 1	Level 2	Level 3
Welding Current	A (Ampere)	C	95	105	115
Flow rate of Gas	liter/min	G	10	15	20
Travel Speed	mm/s	S	2	2.5	3

Table 3.3 Design of welding matrix based on Taguchi L$_9$ orthogonal array strategy

Sl. No.	Welding parameters		
	Current (A)	Gas flow rate (l/min)	Travel speed (mm/min)
1	95	10	2
2	95	15	2.5
3	95	20	3
4	105	10	2.5
5	105	15	3
6	105	20	2
7	115	10	3
8	115	15	2
9	115	20	2.5

Table 3.4: Fixed welding settings

Polarity and Arc Voltage	AC (alternating current); 25 V
Electrode Dia	2.4 mm
Shielding gas	99.99% pure Argon

The next chapter outlines and addresses the findings from all the above investigations. Based on the observed results, process optimisation has also been done. Chapter 5 covers this.
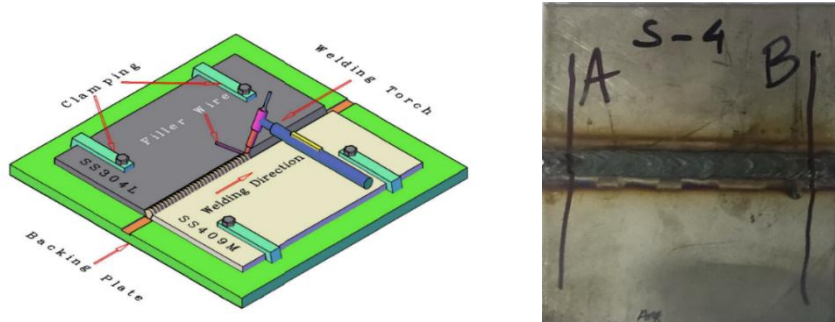
Figure 3.9 Schematic diagram of welding process and welded sample
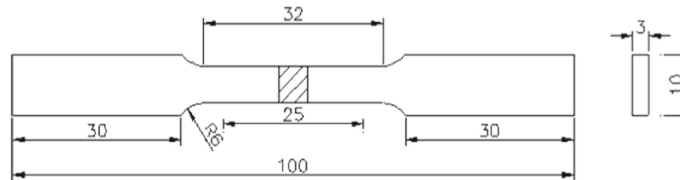
Figure 3.10 ASTM E8 standard sketch for sample designed

Figure 3.11 Tensile test specimen image

All the samples have been visually inspected after welding. Right after that, X-ray radiography tests are carried out. The welded samples are now machined to make tensile test specimens. The elementary specifications of the tensile test samples are shown in Figure 3.10 in a schematic diagram. An etchant consisting of 20 ml of ethylene glycol, 20 ml of HNO_3, and 100 ml of ethanol is used to etch Ferritic stainless-steel samples, whereas samples of Austenitic stainless steel are etched using a solution of aqua regia 3 HCL + 1 HNO_3. The samples were examined under a Leica microscope, and pictures of microstructures of the base metal, heat affected zone (HAZ), and weld metal were captured. Every one of these samples has also had hardness tested. Weld metal, heat affected zone

(HAZ), and base metal hardness measurements were taken at various regions and different times during the process.

The next chapter presents and discusses the findings from all the investigations. The data has also informed process optimization efforts. It is included in Chapter 5 in the book.

In last chapter, the details of experimental setup, procedure, and strategy had been covered. These are the portions where the results are discussed and given.

4.1 Results and Discussion

Results and discussion for ASS 304L and ASS 304L combination of welded samples.

4.1.1 Results and Discussion of TIG Welding of Austenitic SS 304L

The experimental design was based on the Taguchi L_9 orthogonal array, and three sets of experiments were conducted. In the first set of tests, the Taguchi L_9 orthogonal array design was used to butt welded Austenitic SS 304L. This section begins with an overview and discussion of the results in accordance with the Taguchi design of experiment.

4.1.1.1 Visual Inspection and X- ray Radiography Test Results for ASS 304L

 After the welding process, a visual examination was conducted to identify any visible defects on the weld specimens made of Austenitic stainless steel. Visual examination is crucial, as it serves as the primary criterion for approving various kinds of weldments. The type of inspection described is widely used because of its ease of application, quickness, affordability, ability to provide crucial information on the welds, and overall compliance with specification requirements. The results of the visual examination are shown in table 4.1. According to this table, no major defects have been identified.

Table 4.1 Results of X- ray test and visual inspection inspections ASS 304L as per Taguchi L_9 design of experiment

Sl. No.	Current (A)	Travel speed (mm/min)	Gas flow rate (l/min)	Visual inspection	X-ray test result
01	95	2	10	No defects	Porosity
02	95	2.5	15	Undercut	Lack of fusion
03	95	3	20	No defects	No defects
04	105	2.5	10	No defects	No defects
05	105	3	15	No defects	No defects
06	105	2	20	No defects	No defects
07	115	3	10	No defects	No defects
08	115	2	15	No defects	No defects
09	115	2.5	20	Lack of fusion	Lack of fusion

(a)   (b)   (c)

(d)   (e)   (f)

(g)   (h)   (i)
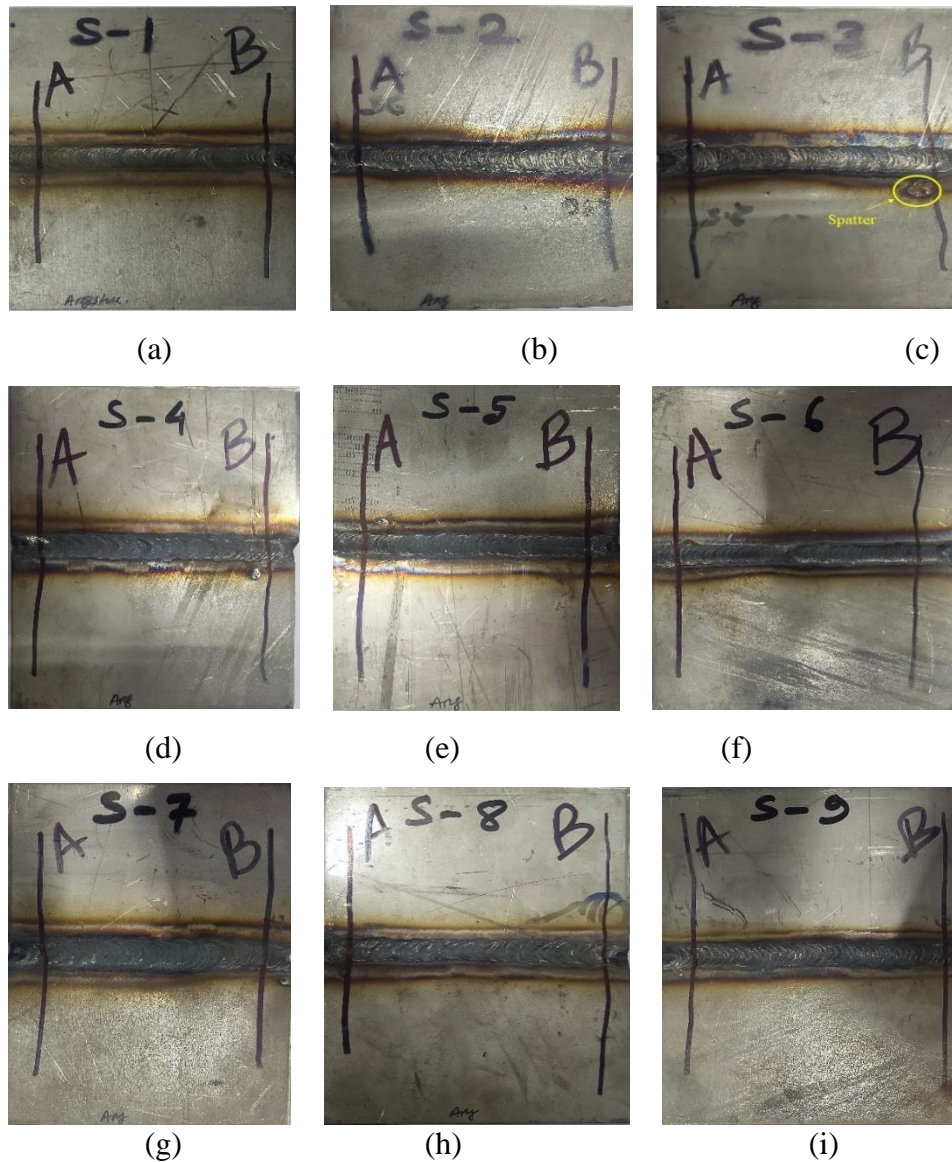
Figure 4.1 Austenitic SS 304L (a - i) total numbers of welding plates

4.1.1.2 X-ray Radiography Test Results and Discussions of ASS 304L

After visual inspection using XXQ-2005 X-ray defect detector, all-welded samples were X-ray to assess their interior soundness. In figure 4.1 (a – i), show the X-ray radiography image of all nine samples and in table 4.1 shows the results of the X-ray radiography study. On X-ray inspection, most weld samples are found to be flawless. Meanwhile, the porosity is in samples S1 occur. Pores in the metal may occur if airborne gases are caught inside of it while it solidifies. Also, as was mentioned up top in regards to visual examination, faults in the base metal or filler wire could lead to insufficient penetration. This issue could also be

brought on by an electrode angle that is too great. Better management of the gas flow and travel speed might have prevented this issue, which was likely caused by entrapped gas in the weld pool. Such a defect might also result from an excessively fast travel speed. Issues can arise if the welding parameters and their operating ranges are chosen incorrectly.
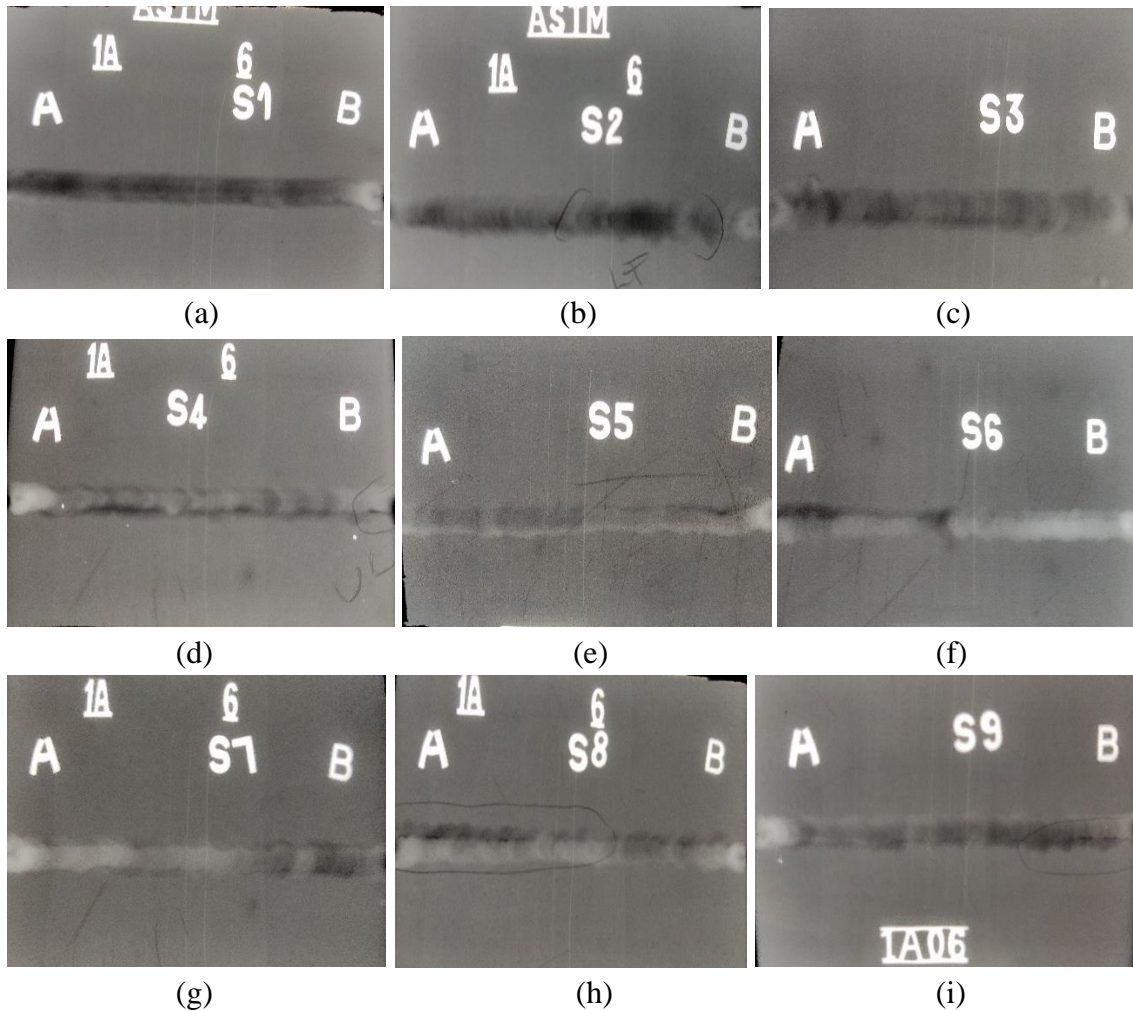
Figure 4.2 X-ray radiography film for Austenitic SS 304L (a-i) total welded samples

After adjusting the amount of welding current, flow rate of gas, and travel speed to their designated values, the visual and radiographic assessment tables indicate minimal flaws. Samples S4, S5, S6, S7, and S8 have also successfully undergone optical and X-ray radiographic examinations, revealing no significant defects. Figure 4.2 (a-i) displays X-ray radiographic film images of all nine samples of TIG-welded SS 304L stainless steel.

4.1.2 Tensile Test Results and Discussion of ASS 304L

After the completion of the non-destructive testing, the destructive testing was carried out. A table contains the results of the tensile test that was performed. A comprehensive range of tensile parameters, including UTS, and % of elongation, weld bead width and penetration depth were included into the results.

Table 4.2 Tensile test for ASS 304L

Sl. No.	UTS (MPa)	% of elongation	BW (mm)	DP (mm)	Fracture zone
S1	628.5	50.25	4.97	1.97	HAZ
S2	620.75	43.17	3.65	2.24	HAZ
S3	619.08	51.2	3.9	2.04	HAZ
S4	646.7	47.3	3.19	2.63	HAZ
S5	650.14	63.78	4.31	1.84	HAZ
S6	612.9	52.9	3.41	2.72	BM
S7	631.8	30.6	3.48	2.42	HAZ
S8	631.2	51.4	3.78	2.43	BM
S9	646.9	56.4	3.41	2.39	HAZ

The just-shown table 4.2 lists all the results as follows: The highest possible UTS was found at sample number S5, and the lowest possible UTS was identified at sample S6. All the samples are fractured from the base or heat-affected zone.

Stress vs Strain curves for welded samples

The stress vs strain curve provides vital insights into the mechanical characteristics of materials, allowing for improved material design, selection, and utilization in engineering and industry. Figures 4.3 to 4.11 display the stress-strain curves of all butt-welded samples numbered 1 through 9.
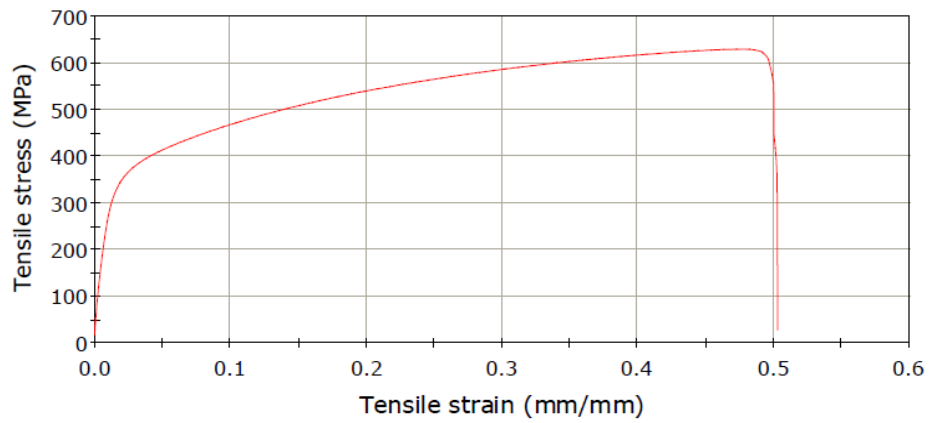
Figure 4.3 Stress vs Strain curves of welded sample no. S1
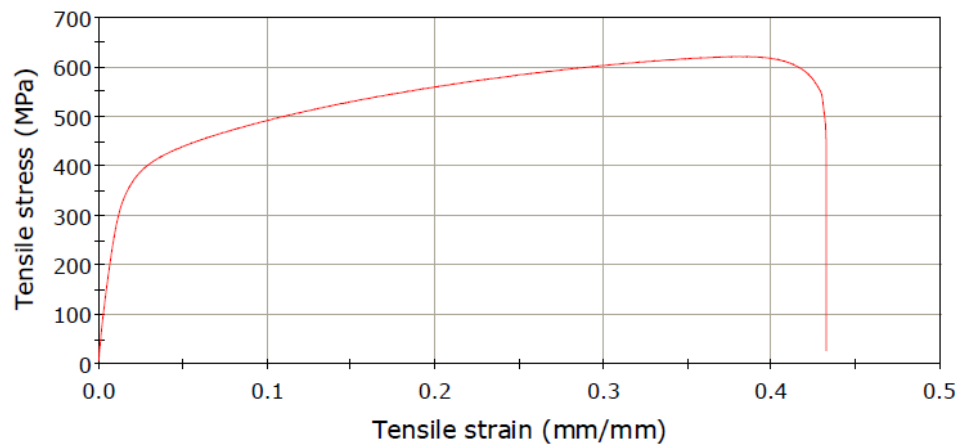
Figure 4.4 Stress vs Strain curves of welded sample no. S2
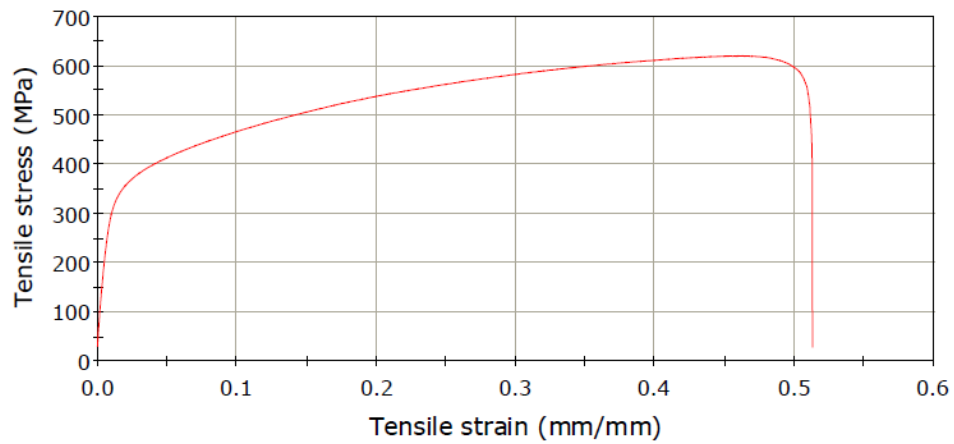
Figure 4.5 Stress vs Strain curves of welded sample no. S3
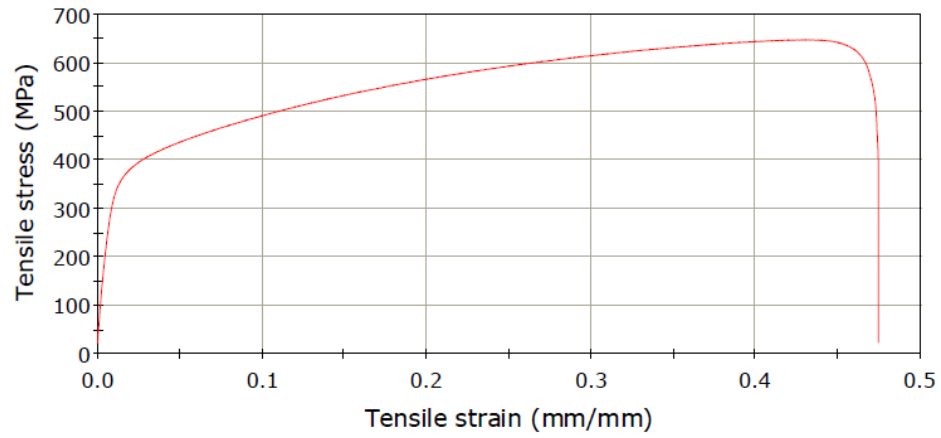
Figure 4.6 Stress vs Strain curves of welded sample no. S4
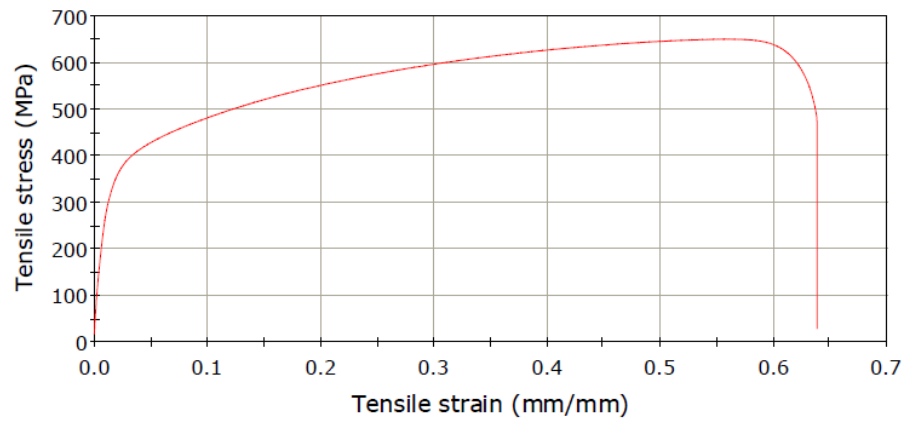
Figure 4.7 Stress vs Strain curves of welded sample no. S5
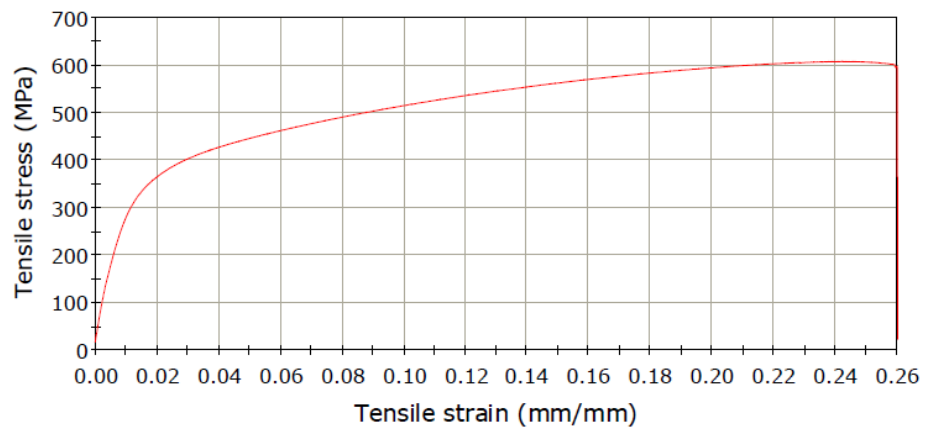
Figure 4.8 Stress vs Strain curves of welded sample no. S6
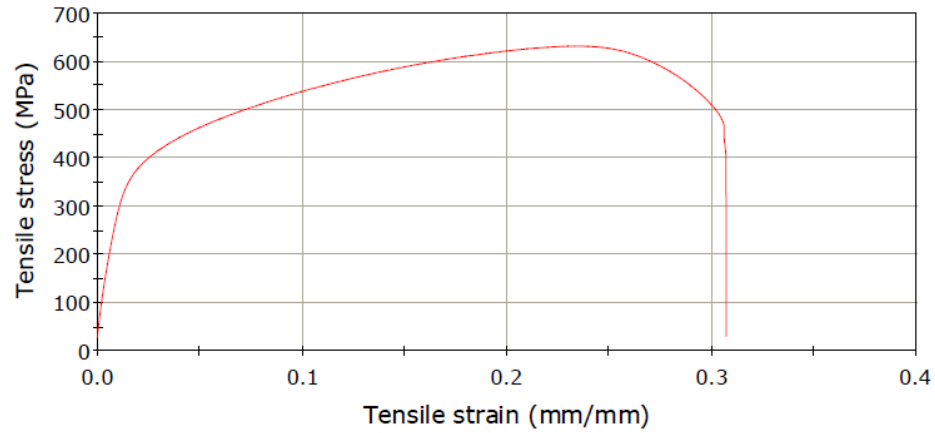
Figure 4.9 Stress vs Strain curves of welded sample no. S7
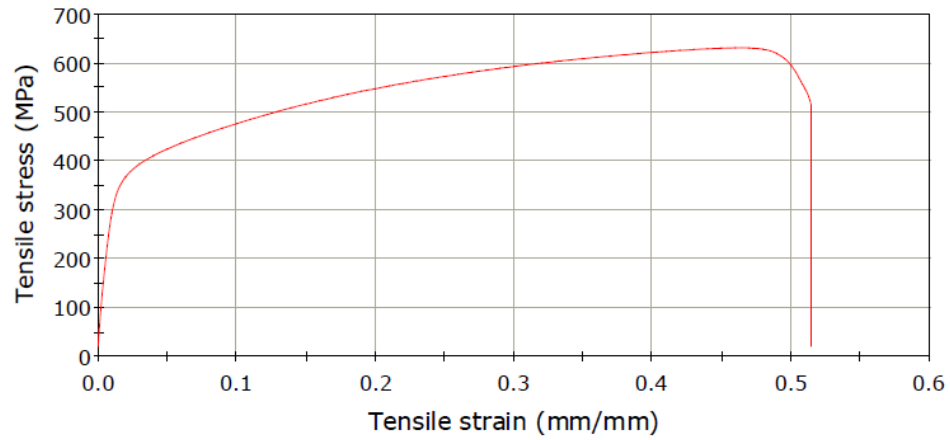
Figure 4.10 Stress vs Strain curves of welded sample no. S8
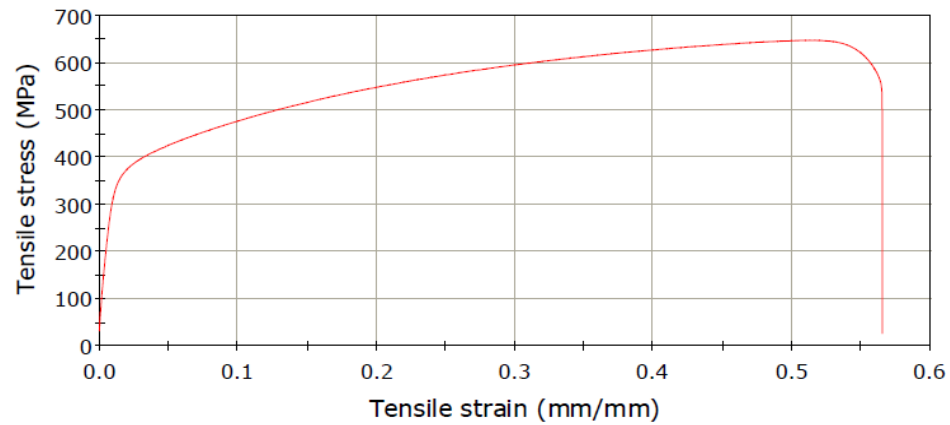
Figure 4.11 Stress vs Strain curves of welded sample no. S9

Figures 3.10 and 3.11, respectively, show the tensile test specimens in compliance with ASTM- standards E8. A tensile test has executed at room temperature using the Instron universal testing system. The experiment conducted three repetitions of tensile testing on

each sample, following the ASTM standard E8. Table 4.2 displays the outcomes of the average tensile test for each sample. Upon investigation, it is evident that samples S3, S6, S8, and S9 have had fractures in the base zone owing to inadequate heat input. This indicates that the parent material is much weaker than the welded zone and so many cause are there for breaking base zone like residual stress development, microstructural changes etc. Because the welding parameters heat input, travel speed, and gas flow rate are carefully managed to produce a balanced microstructure with little residual stresses, samples S1, S2, S4, S5, S7, and S9 have broken approximately within the HAZ (heat-affected zone). The figures 4.3 to 4.11 show the tensile stress vs strain curve for samples S1 to S9, respectively and all the graphs are ductile nature. The ultimate tensile strength achieved is 650.14 MPa, which is the greatest value achievable under moderate high heat input conditions. The sample labelled as S5 exhibited the most percentage elongation, with a value of 63.78%. The sample labelled as S7 demonstrates the lowest value of percentage elongation, which is 30.6.

4.1.3 Micro Hardness Analysis of the Specimen

Vickers microhardness testing machine, UHL VMTH figures 3.6, has been used for measuring microhardness. The Vickers hardness number is the ratio of applied force on the Vickers indenter to the contact surface area of the permanent imprint produce by the diamond indenter. The Vickers hardness, measured in kgf/mm^2, is obtained in practice using the formula [122].

$HV = 1.8544 \, P_1/d_1$

where

P1 represents the force measured in kilograms-force (kgf),

d1 represents the measurement of the long diagonal in millimetres (mm).

The indentation points are taken at ± two each nearest area at base zone, ± two for HAZ zone and ± two for fusion zone or weld zone total six points are taken. Micro hardness experiments on etched transverse cross sections of the welded specimens under a force of 500g for duration of 20 seconds, after micro structural analysis. The weld zone of the specimen welded with low and high heat input exhibits reduced hardness. The highest levels of hardness were seen in the specimen that was created with a moderate heat input, mostly because of its more refined grain structure. The micro-hardness results for all the samples are shown in table 4.3.

Some areas exhibit unsatisfactory results, which may be due to several factors such as the different materials properties and compositions of the base and filler materials, dilution, heating and cooling cycles, and other relevant parameters. The hardness in various areas of the weldment exhibits consistent results.
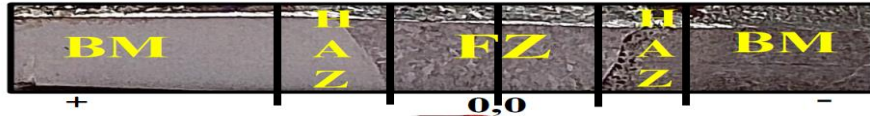
Figure 4.12 A schematic diagram of micro hardness measurements processes

Table 4.3 Micro hardness study of welded samples ASS 304L

Sl. No.	*Micro Hardness (HV) at position*					
	BM	*HAZ*	*FZ*	*FZ*	*HAZ*	*BM*
S1	284	290	305	326	295	282
S2	295	325	371	352	297	265
S3	265	275	290	284	233	232
S4	270	310	345	348	283	255
S5	218	252	423	400	248	235
S6	246	280	297	284	222	224
S7	238	268	290	295	225	220
S8	250	257	312	290	240	225
S9	280	292	318	292	284	254
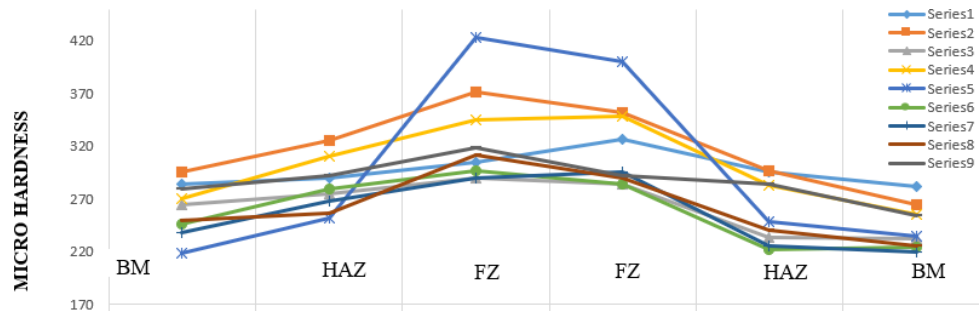
Figure 4.13 Micro hardness graph for Austenitic SS 304L sample S1 to S9

4.1.4 Microstructural Analysis of Austenitic SS 304L

The Leica DM LM metallurgical microscope (as depicted in figure 3.5) has been used for examining of microstructure of all the welded samples with 100X and 200X zoom scale. TIG welding results in distinct optical microstructures in both the transition and weld zones, as

seen in figures. 4.14 - 4.31. Regarding the microstructure of base metal passes, they exhibit pure Austenitic grains with double boundaries. Base metal, heat affected zone, and weld metal can all be easily distinguished from one another (WM). Regardless of the specified parameters, there is a noticeable disparity between the microstructure of a base metal and that of a weld metal. The fusion zone is dominated by materials like ferrite and austenite. The bright spots are austenite, and the darker spots are ferrite. Micrographs of TIG-welded samples no. S1 and S2 (figure 4.14, 4.15, figure 4.16, 4.17 and SEM figure 4.36) reveal epitaxial columnar dendritic development from the fusion border to the weld centre during the early stages of solidification. Yet, the HAZ region has coarser granules than the metal's base. Maybe it is because of how slowly the HAZ area cools. The dendrites of weld metals have been seen to include a lacy ferrite at their centre, which is surrounded by an interdendritic -phase.
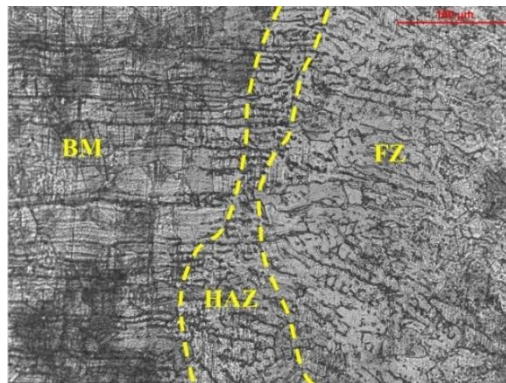
Figure 4.14 Metallographic image of S1   Figure 4.15 Metallographic image of S1
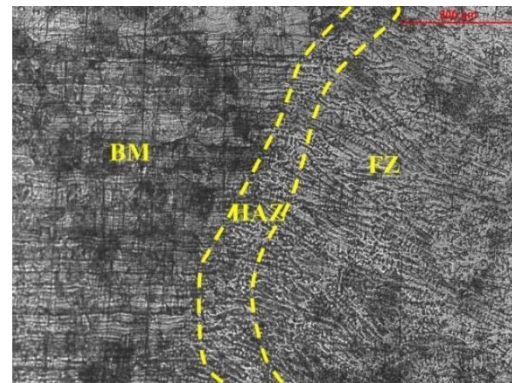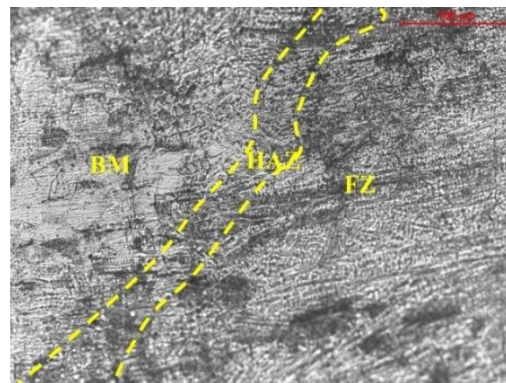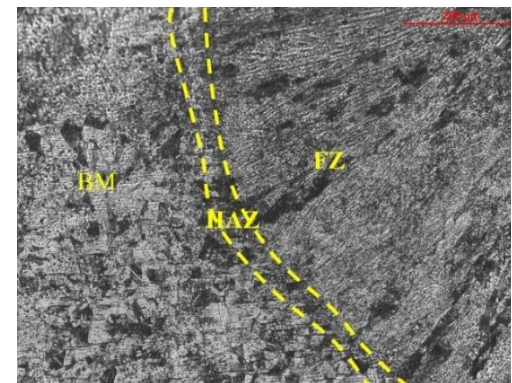
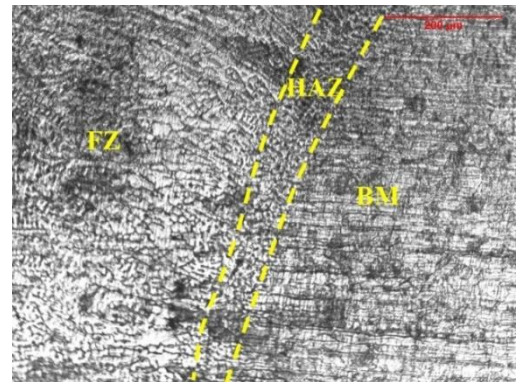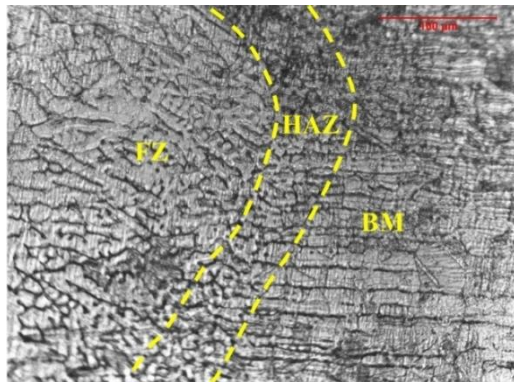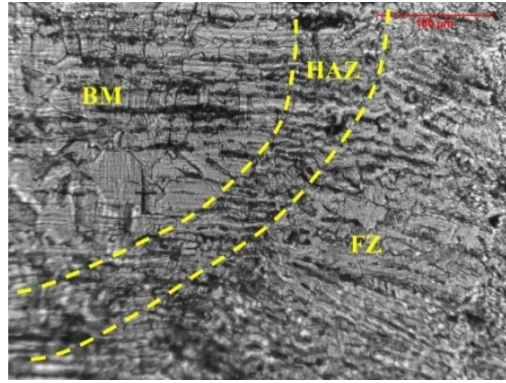Figure 4.16 metalographic image of S2   Figure 4.17 Metallographic image of S2
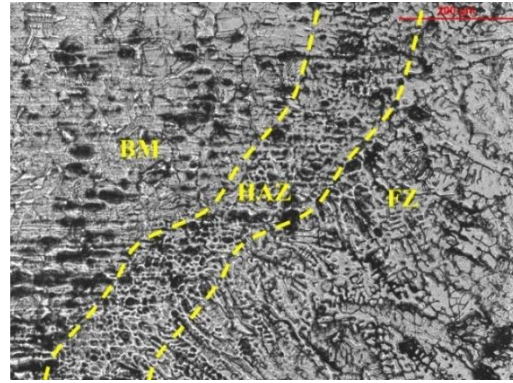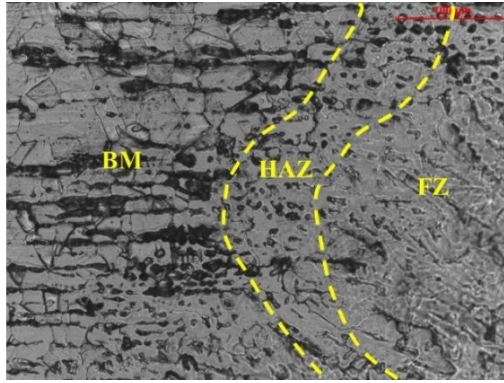
Figure 4.18 Metallographic image of S3   Figure 4.19 Metallographic image of S3

Sample no. S3 and S9 (figure 4.18, 4.19 and figure 4.30, 4.31) demonstrate that the larger the flow rate of the shielding gas, the faster the solidification rate, and hence the larger the grains. When the shielding gas flow increases, the grain structure becomes more distinct and coarser.
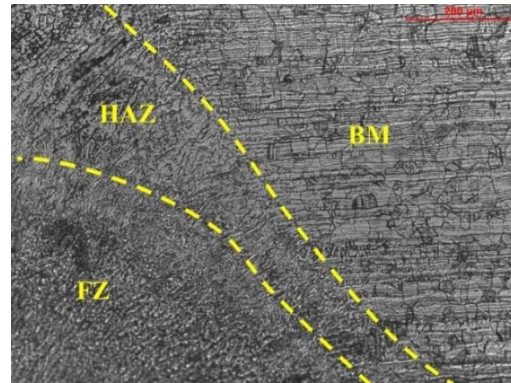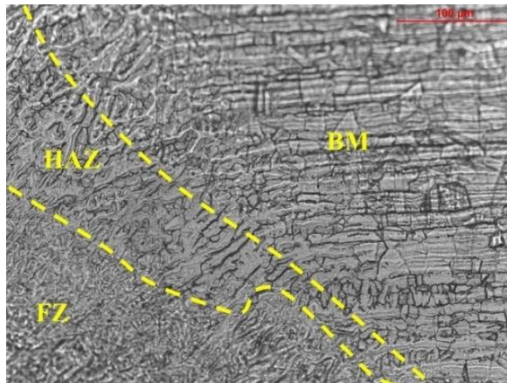
Figure 4.20 Metallographic image of S4 Figure 4.21 Metallographic image of S4
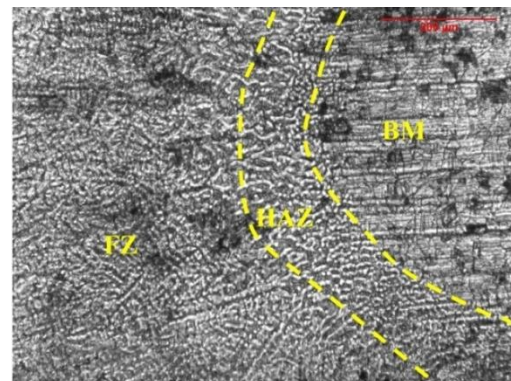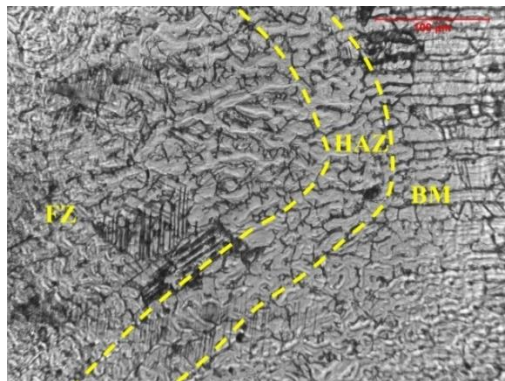
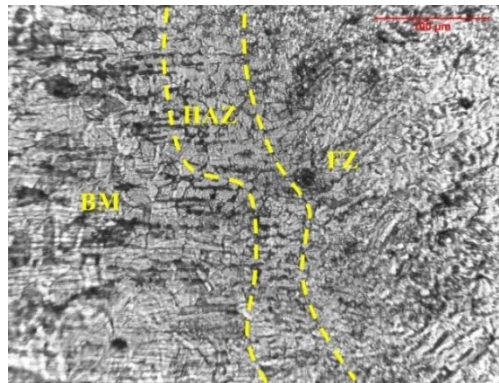Figure 4.22 Metallographic image of S5 Figure 4.23 Metallographic image of S5
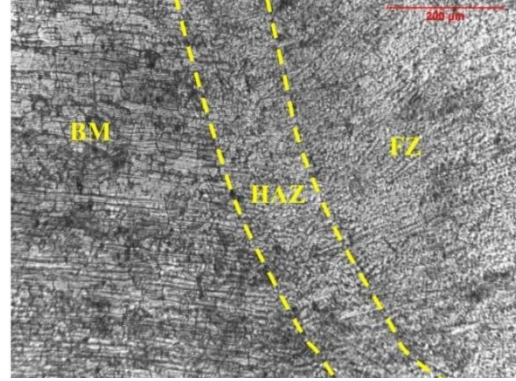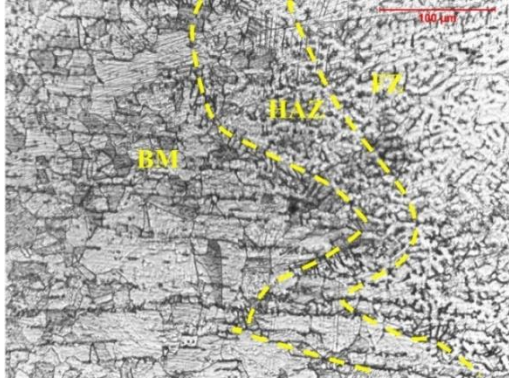
Figure 4.24 Metallographic image of S6   Figure 4.25 Metallographic image of S6

Figure 4.22, 4.23 (sample No. S5) shows weld metal microstructure on Austenitic joint side. SS304 stainless steel microstructure showed equiaxed austenite grains. Every sample had unmodified delta-ferrite at austenite grain boundaries on the Austenitic side of the HAZ (heat affected zone) microstructure. HAZ microstructures were typically finer than BM microstructures, which may have increased mechanical properties. When welding at lower speeds, the high solidification restrictions induced by the grains in the innermost region of the weld being oriented longitudinally allow for the formation of a nearly circular weld pool. Raising the welding rate likewise raises the cooling rate, causing the grains to grow and disperse over a greater area. The structure illustrated in figure 4.24, 4.25 (sample no. S6) is made up of smaller, equiaxed grains.

Figure 4.26 Metallographic image of S7   Figure 4.27 Metallographic image of S7

Figure 4.28 Metallographic image of S8 Figure 4.29 Metallographic image of S8
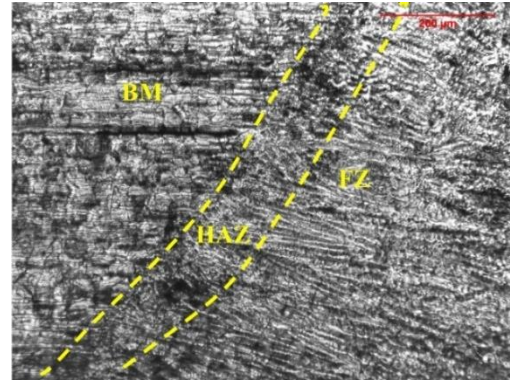
Figure 4.30 Metallographic image of S9   Figure 4.31 Metallographic image of S9
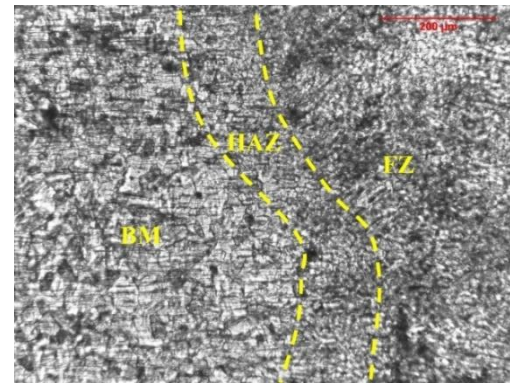
Coarse grains were found in the weld zone of sample no. S7 and S8 (figure 4.26, 4.27, figure 4.28, 4.29 and SEM figure 4.34, 4.35) weld at high welding current. Due to FZ (fusion zone) and HAZ phase variations, microhardness and tensile strength affect TIG welded junction quality. Because of the moderate heat input and cooling rate, the weld zone in sample S4 (figure 4.20, and 4.21) and sample S1 (figure 4.14, and 4.15) matrix exhibit very thin skeletal-ferrite, grain, sub grain, and migrating boundary structures. This is because the matrix is Austenitic. Sample 3 (figure 4.18, 4.19) weld microstructure has coarse equiaxed grains. Welding current changes weld joint microstructure and mechanics. Heat input affects TIG welding microstructural phase shift in the FZ and HAZ due to cooling rate. High heat input slows cooling, affecting microstructural properties. High heat input raises weld zone and base metal temperatures, decreasing the thermal gradient between them and slowing cooling. Low heat input reverses. Cooling accelerates microstructural phase change in the fusion zone and HAZ.
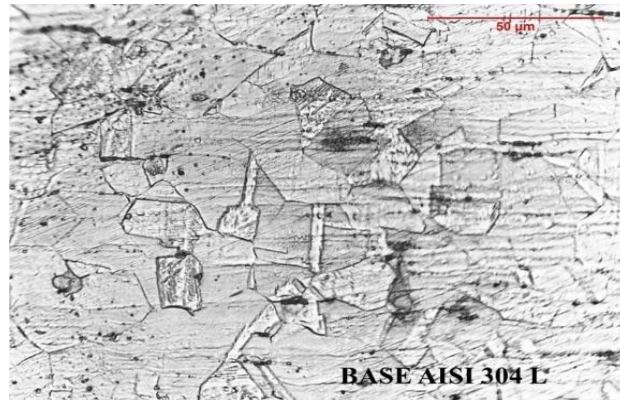
Figure 4.32 Metallographic image of parent material Austenitic SS 304L

All the samples exhibit pure Austenitic grains with twin's boundaries, indicating that the Austenitic phase is the primary component of SS 304L stainless steel, which has an FCC crystal structure throughout. Figure 4.30 illustrates the typical microstructure of a base metal. All the input parameters are chosen from trial and run process. The input parameters are selected from the trial-and-run procedure. In TIG welding, the correlation between current and travel speed is critical to providing high-quality welds. Both factors have a substantial impact on the heat input, weld bead characteristics, and overall weld quality. The impact of current during welding is that increasing the current will lead to an increase in heat input, resulting in a wider and deeper weld bead profile. Conversely, reducing the current would decrease the heat input, resulting in a narrower and shallower weld bead profile. The travel speed influences the welding process by determining the heat input. Decreasing the travel speed leads to an increase in heat input, resulting in a broader and more profound weld bead. Conversely, increasing the travel speed reduces the heat input, resulting in a smaller and shallower weld bead. However, by properly adjusting the current and travel speed, we can achieve a higher-quality weld. Shielding gas plays a crucial role during the welding process. It keeps the weld pool from oxidizing. In this experiment no heat treatment process is performed. The change of microstructure has been seen by using optical microscope. The HAZ (Heat affected Zone) of all the samples seen very minimum amount. In most cases, the microstructures of HAZ are not found to be significantly different from the microstructure of base zone. On the other hand, the grains in HAZ have been found to be significantly larger than those in base metal. It is possible that the slower rate of cooling in the HAZ region is to blame. Also, in the HAZ of each and every sample, Austenitic twins were found.

In the HAZ region of sample no. S6, dispersed carbide phases have been discovered (figure 4.24, and 4.25). During the tensile test, this sample had the lowest UTS value. The HAZ region's sample numbers S4 and S5, which correspond to figures 4.20, 4.21 and 4.22, 4.23 respectively, display the highest values in the region, respectively. However, the microstructural study of HAZ has not been able to uncover any significant causes for this phenomenon. When all the samples' weld metal microstructures are compared with either the HAZ microstructures or the base metal microstructures, it is discovered that the appearance of the weld metal microstructures is very different from the appearance of the HAZ and base metal microstructures. Columnar-dendritic grain growth has seen in most of the samples. When a metal solidifies very slowly in the presence of a sharp temperature gradient, it forms columnar grains, which are long, thin, coarse grains. Ferrite and austenite make up the bulk of the fusion zone's composition. The zone that is white is called austenite, and the zone that is dark is called ferrite. Epitaxial columnar dendritic growth has seen in the micrographs of TIG-welded samples during the primary stages of solidification. This growth can be seen moving from the fusion boundary toward the weld centre. However, it was discovered that the grains in the HAZ zone are significantly larger compared to those in the base metal. It is possible that the slower rate of cooling in the HAZ region is to blame for this. It is common knowledge that raising the welding current also raises the amount of heat produced. When there is a greater amount of heat input, the molten weld metal takes a long time to solidify. As a direct consequence of this, the grain size expands and becomes coarser in comparison to the samples that were welded using low welding currents. Moste of the cases found the δ-ferrite can have a vermicular morphology with a coarse dendritic structure when subjected to higher heat inputs, which results in slower cooling rates. Because of the slow solidification rate, figure 4.22, 4.24, and 4.26 grain structures show similar types of grain structures as well. This is because of the higher welding current. The elliptical shape of the weld pool can be transformed into a teardrop shape by increasing the welding current as well as the welding speed. As a direct consequence of this, there is a radial increase in the depth of penetration. Due to the increased speed of the welding process, the width of the heat-affected zone shrinks to an extremely narrow range as the weld pool rapidly cools down. There are a variety of different structures that can be seen in the weld region depending on the welding speed. Both the amount of heat that is introduced and the rate at which the weld is performed can have a

significant impact on the solidification mode of the weld metal. The characteristics of the weld metal's solidification process have the greatest influence on the quality of the weld that is produced. It controls the microstructure, grain structure, and other properties of the weld metal, among other things. Because of this, the grains in the central-most portion of the weld are aligned in a longitudinal direction when the welding speeds are low. This indicates that the solidification constraints are high. In addition to this, a more compact equiaxed grain structure is produced, which is depicted in some Figure. The microstructures of the various zones of the weldment have been influenced by the variation in the parametric condition is not very straightforward. More ever, the effect of the change in the welding parameters on responses has been studied and presented in this chapter.
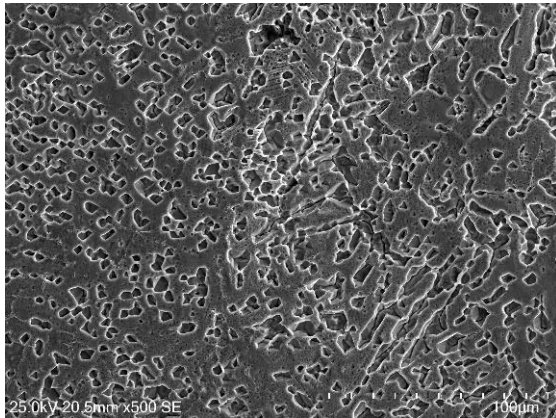
Figure 4.33 SEM image of SS 304L S3   Figure 4.34 SEM image of SS 304L S4
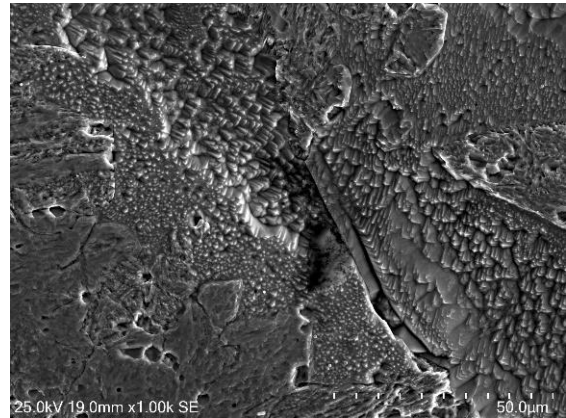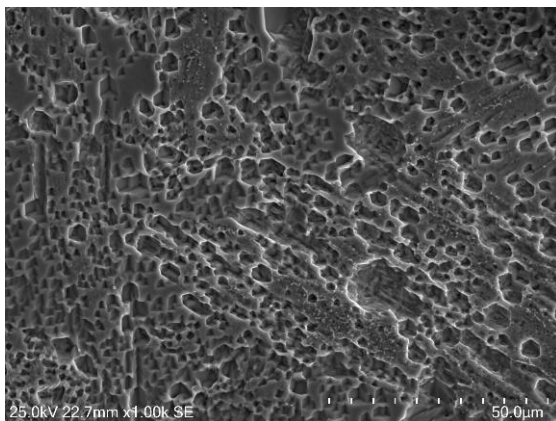
Figure 4.35 SEM image of SS 304L S7   Figure 4.36 SEM image of SS 304L S8
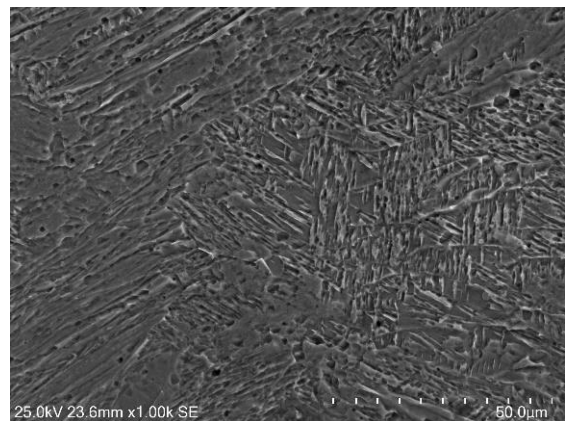
4.1.5 Weld Bead Profile Measurement and Discussion

Stereo microscopes measure the weld bead profile (figure 3.7). Table 4.2 lists the welding configurations and related weld bead geometry; all weld bead figures are provided below.
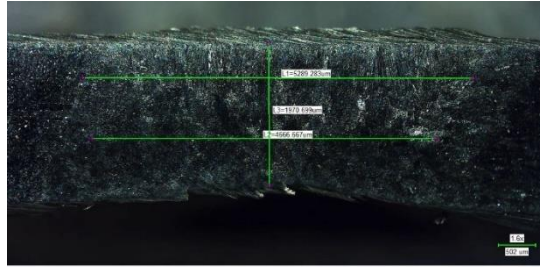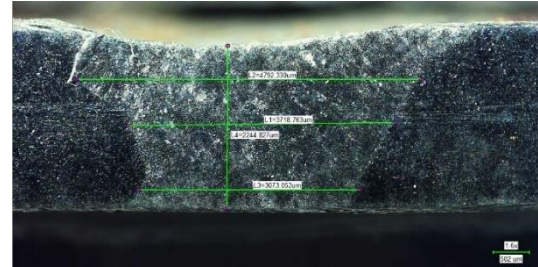
Figure 4.37 weld bead profile S1
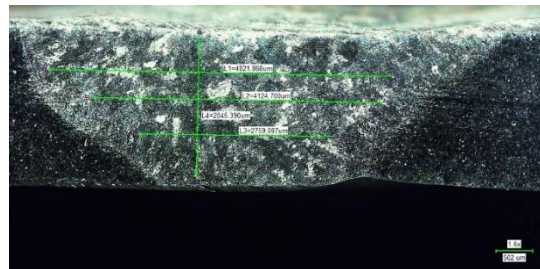
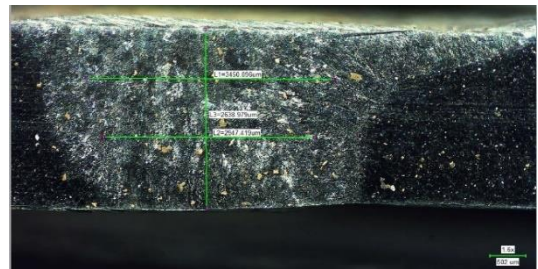Figure 4.38 weld bead profile S2

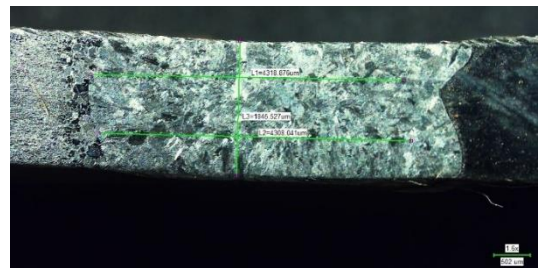Figure 4.39 weld bead profile S3

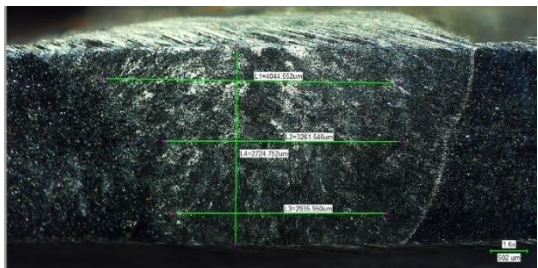Figure 4.40 weld bead profile S4

Figure 4.41 weld bead profile S5

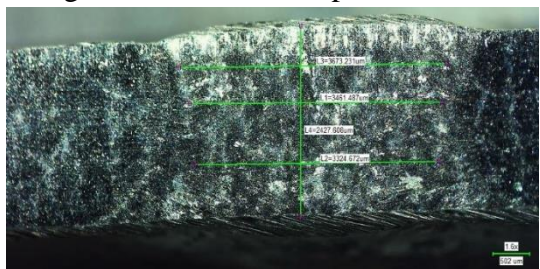Figure 4.42 weld bead profile S6

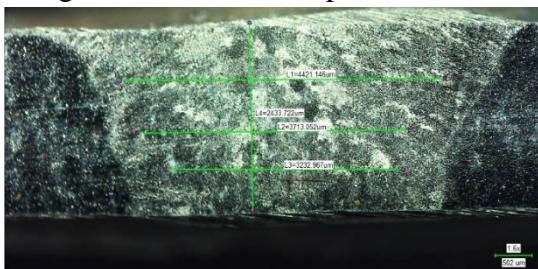Figure 4.43 weld bead profile S7
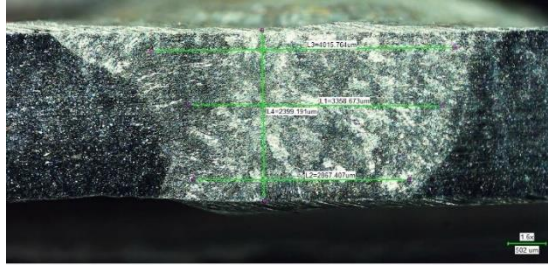
Figure 4.44 weld bead profile S8

Figure 4.45 weld bead profile S9

From figure 4.37, S1 bead width found maximum and depth of penetration is minimum on other hand figure 4.42, S6 depth of penetration is maximum and bead width minimum. TIG welding produces maximum bead width and minimal depth of penetration mostly because to the reduced heat input, concentrated and steady current, and exact control over welding settings. Wider beads are produced by the equal distribution of heat across the surface, but the depth of penetration is restricted by the low heat input as well as the rapid cooling rate. The objective of studying weld bead geometry is to identify the optimal parameters for attaining the intended weld bead form.

4.2 Results and Discussion

Results and discussion for FSS 409M and FSS 409M combination of welded samples.

4.2.1 Results and Discussion of TIG Welding of Ferritic SS 409M

The first series of tests mentioned earlier pertain to the process of welding Austenitic stainless steel. The second series of experiments included welding SS 409 M Ferritic stainless steel using ER308L filler wire, following the experiment's L_9 Taguchi orthogonal design. The following paragraphs present and analyse the outcomes.

4.2.1.1 Visual Inspection and X- ray Radiography Test Results for FSS 409M

After the welding process, Ferritic stainless steel weld specimens underwent a visual inspection and X-ray radiography testing to identify any potential surface flaws. The significance of these examinations was discussed before. A visual examination was performed, and the findings are shown in table 4.4

Based on the results of a visual examination table 4.4, it has been determined that under certain welding circumstances, no defects were discovered.

Table 4.4 Results of X- ray test and visual inspection on Ferritic SS 409M as per Taguchi L$_9$ design of experiment

Sl. No.	Current (A)	Travel speed (mm/min)	Gas flow rate (l/min)	Visual inspection	X-ray test result
S1B	95	2	10	No defects	No defects
S2B	95	2.5	15	Excessive deposition	Porosity
S3B	95	3	20	No defects	No defects
S4B	105	2.5	10	No defects	No defects
S5B	105	3	15	No defects	No defects
S6B	105	2	20	No defects	No defects
S7B	115	3	10	Excessive deposition	Lack of penetration
S8B	115	2	15	No defects	No defects
S9B	115	2.5	20	No defects	No defects

(a)   (b)   (c)

(d)   (e)   (f)
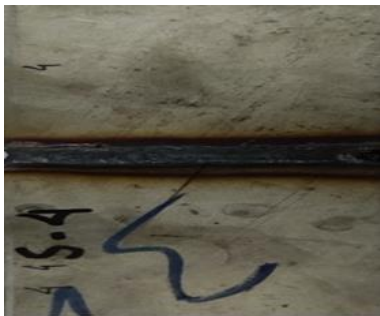
<div align="center">
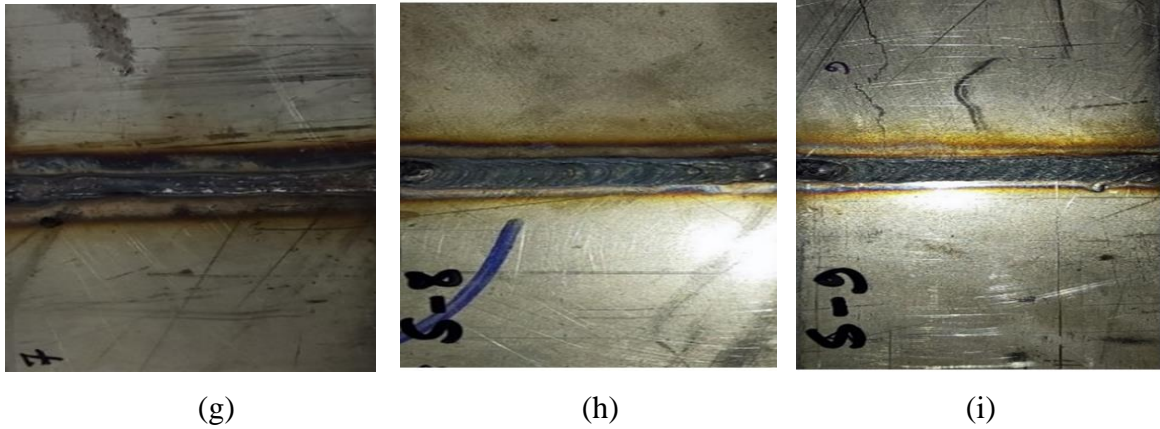
(g)   (h)   (i)
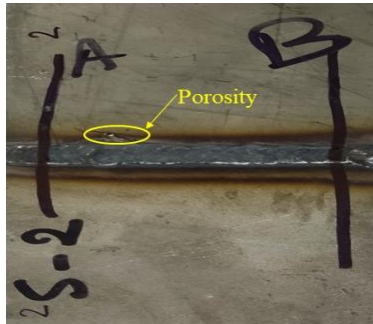
Figure 4.46 Ferritic SS 409M (a to i) total numbers of welding plates

</div>

4.2.1.2 X Ray Radiography Test Results and Discussions of FSS 409M

After visual inspection using XXQ-2005 X-ray defect detector, all-welded samples were X-ray to assess their interior soundness. Figure 4.46 show X-ray radiographs of all samples (S1, to S9 respectively), and table 4.4 shows the findings of visual inspection and X-ray radiography. The pictorial views of the X-ray films are shown in figures 4.47.

<div align="center">

(a)   (b)   (c)

(d)   (e)   (f)
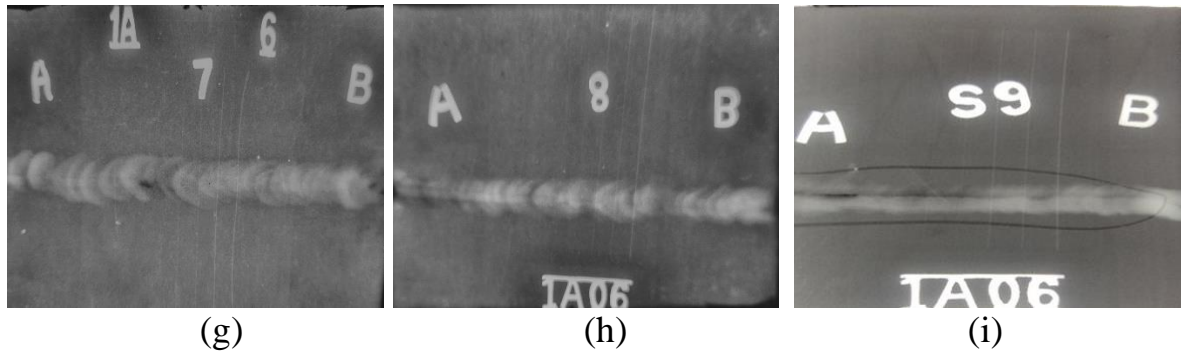
</div>

| (g) | (h) | (i) |
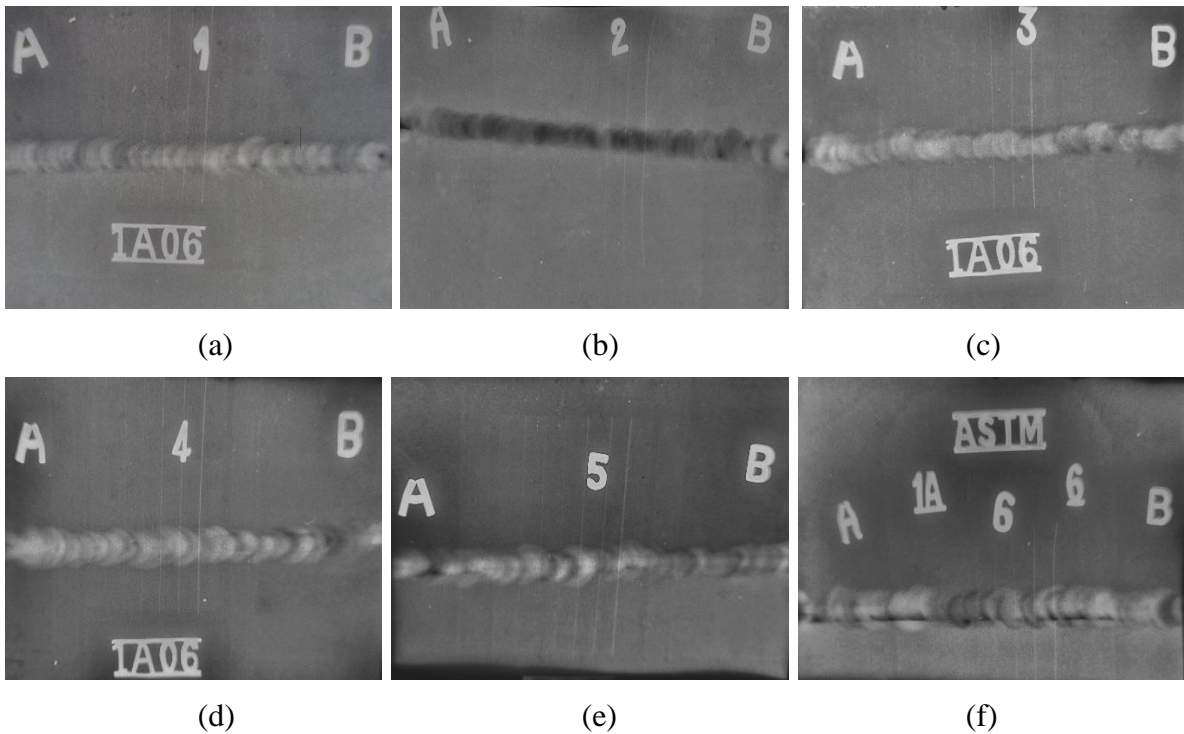
Figure 4.47 X-ray radiographic film for Ferritic SS 409M (a - i) total welded samples

The lack of root or lack of side wall fusion of the weld may have happened because of to the insufficient current flow, inadequate cleaning, high speed of the welding torch, and the presence of oxides, scale, and other impurities that prevent appropriate fusion among the deposited metal and the base metal. The lack of penetration problem may also be caused by any imperfections in the base metal or filler wire, as previously indicated during visual examination. This kind of problem may also be caused by an abnormal electrode angle.

 An insufficient heat input cannot ensure sufficient melting of the weld material. During the process of the metal's solidification, sample number 3 shows porosity, which is probably the result of gas being trapped within the composition of the metal. Porosity is a big problem that should be resolved, yet doing so is a considerable task itself. Initially the contamination of the shielding gas, secondly the contamination of the filler metal, and finally the contamination of the parent metal are probably the most important reasons that are contributing to this problem. Some samples are found lack of fusion and some porosity has been observed. During welding the different factors are affect the weld quality, one of the most important factors is heat input if heat input is insufficient then the metals are not fuse in properly due to this some defects are occurring. Other cause can be the found travel speed is more or slow then different defects are found, shielding gas also an important factor for TIG welding. All the images of X-ray film are given in figure 4.47.

4.2.2 Tensile Test Results and Discussion of FSS 409M

After the completion of non-destructive testing, all samples undergo destructive testing. Below is a table presenting the data for the results of a tensile test.

Table 4.5 Tensile test for FSS 409M

Sl. No.	UTS (MPa)	% of elongation	BW (mm)	DP (mm)	Fracture zone
S1B	432.5	20.4	4.96	2.81	BM
S2B	480.8	14.9	5.38	3.02	BM
S3B	438.1	20.8	5.10	2.65	BM
S4B	435.5	24.7	4.30	2.65	HAZ
S5B	450.9	18.0	4.87	2.87	HAZ
S6B	441.2	27.7	4.18	2.80	BM
S7B	498.6	18.9	4.72	2.44	HAZ
S8B	490.6	18.5	4.65	2.36	BM
S9B	498.9	22.2	4.34	2.81	BM

Stress vs Strain curves for welded samples

The stress against strain curve provides crucial insights into the mechanical properties of materials, enabling enhanced material design, selection, and utilisation in engineering and industry. All butt-welded samples numbered from 1 to 9 have their stress vs strain curves depicted in figures 4.48 through 4.56.
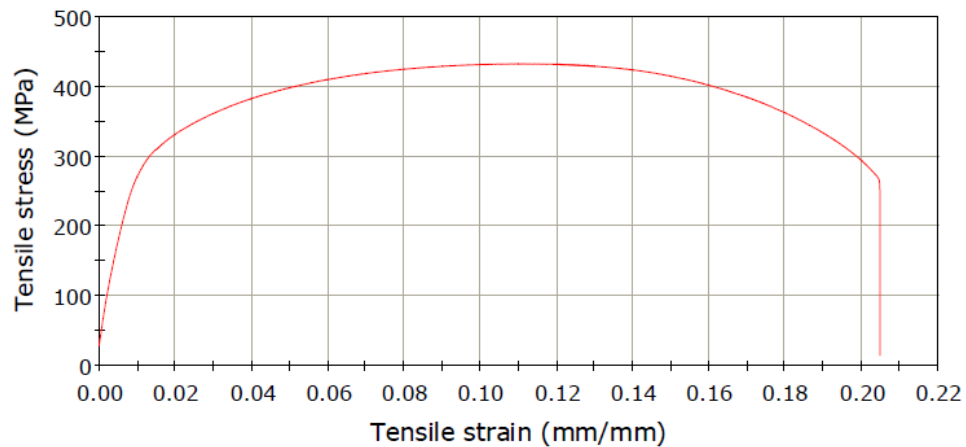

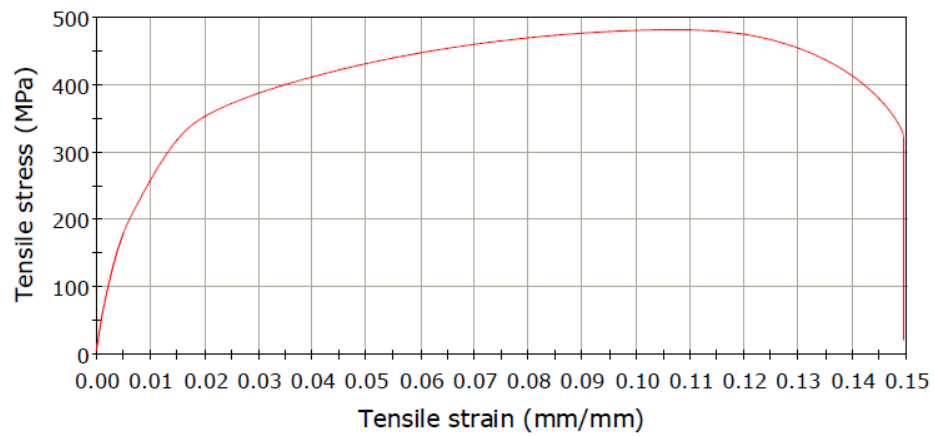Figure 4.48 Stress vs Strain curves of welded sample no. S1B

Figure 4.49 Stress vs Strain curves of welded sample no. S2B
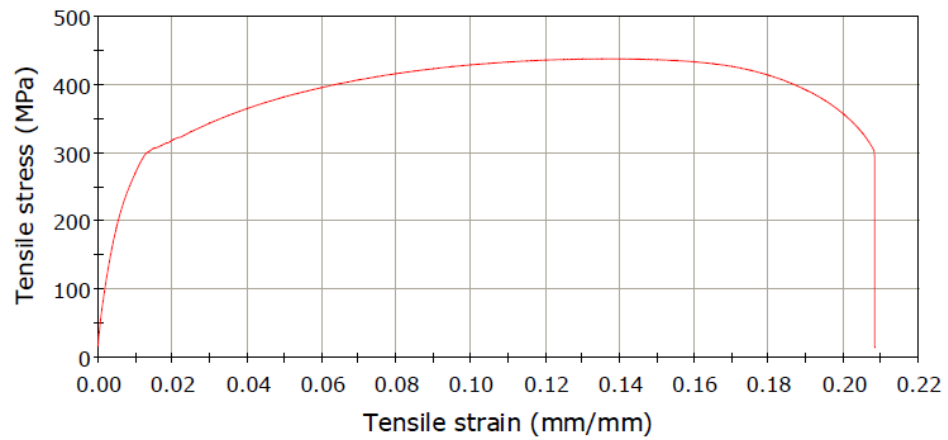

Figure 4.50 Stress vs Strain curves of welded sample no. S3B
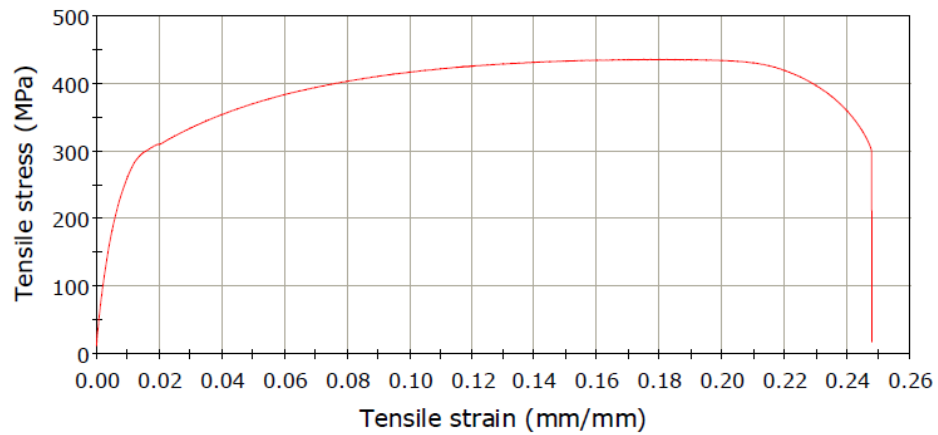

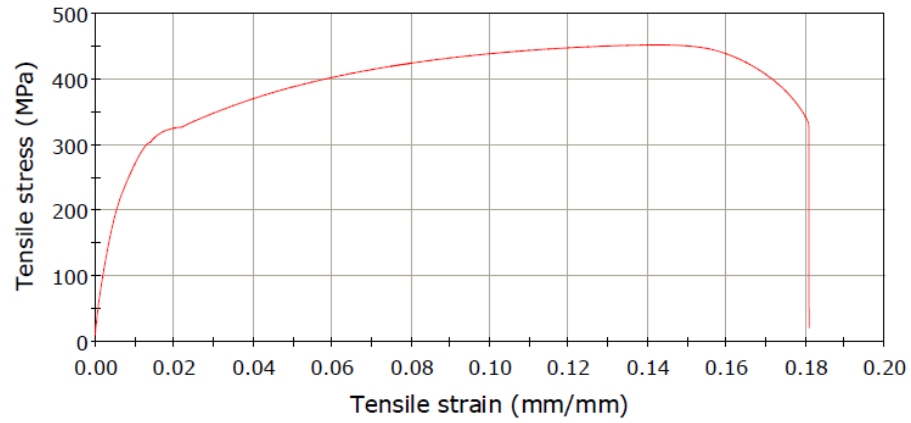Figure 4.51 Stress vs Strain curves of welded sample no. S4B

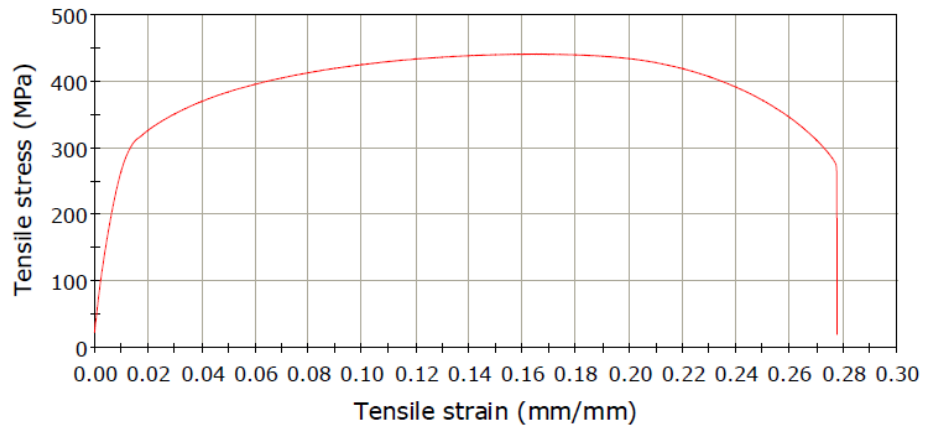Figure 4.52 Stress vs Strain curves of welded sample no. S5B

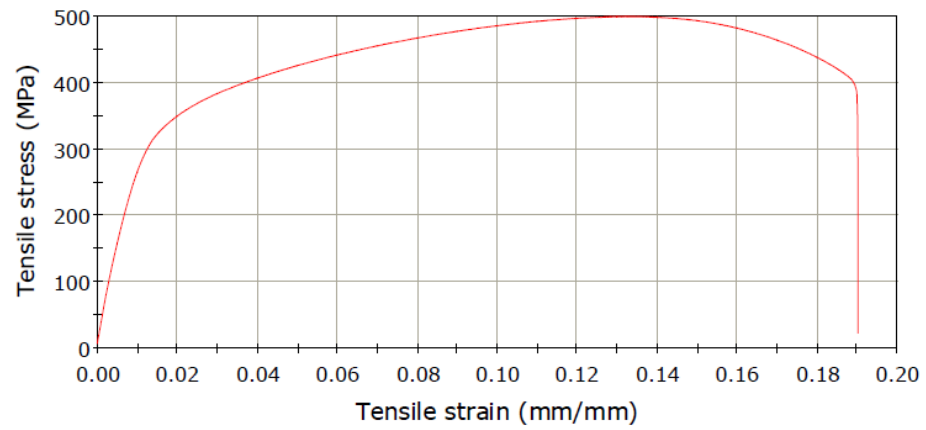Figure 4.53 Stress vs Strain curves of welded sample no. S6B

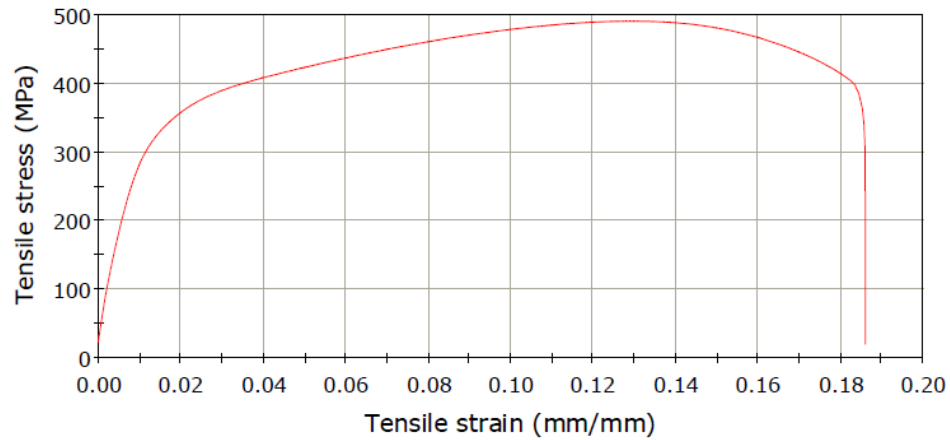Figure 4.54 Stress vs Strain curves of welded sample no. S7B

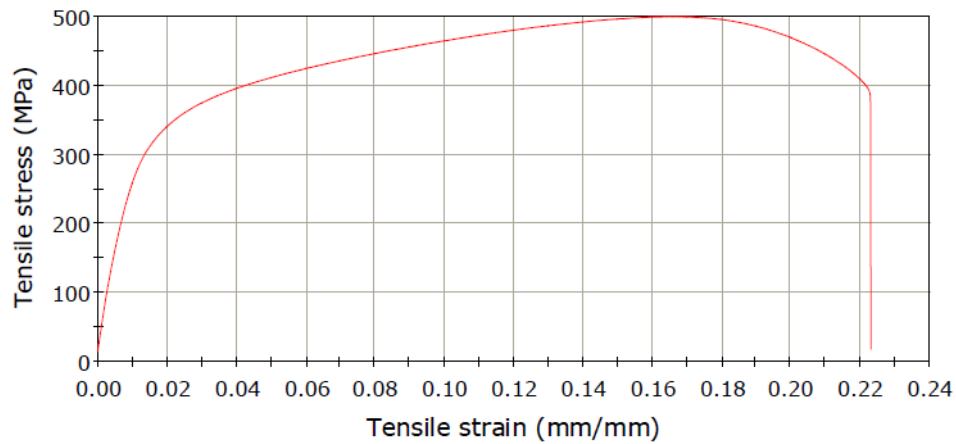Figure 4.55 Stress- Strain curves of welded sample no. S8B

Figure 4.56 Stress vs Strain curves of welded sample no. S9B

Figures 3.10 and 3.11 illustrate the formation of the tensile test specimens by ASTM -E8 standard. The experiments are conducted using room-temperature tensile testing using the Instron universal testing equipment. On each sample, the experiment tested tensile strength three times using ASTM-E8. For every sample, table 4.5 lists the results of the average tensile test. Upon investigation, it is evident that samples S1B, S2B S3B, S6B, S8B, and S9B have had fractures in the base zone due to inadequate heat input. This shows that there are many reasons for breaking the base zone, such as residual stress generation and microstructural changes, and that the base material is much weaker than the welded zone. Because the welding parameters precisely control heat input, travel speed, and gas flow rate to create a balanced microstructure with minimum residual stresses, samples S5B and S7B have broken about inside the heat-affected zone (HAZ). Figures 4.48 through 4.56 show the tensile stress versus strain curves for samples S1 through S9; all the graphs are ductile. Under moderately

high heat input conditions, the highest ultimate tensile strength is 498.9 MPa. At a value of 27.7%, the sample designated as S6B showed the highest percentage elongation. At 14.9%, the sample designated S2B has the lowest percentage elongation value.

4.2.3 Microhardness Analysis of Specimen

Micro hardness is measured using a Vickers micro hardness testing machine, UHL VMTH (Figure 3.5). The applied force on the Vickers indenter and the contact surface area of the permanent impression made by the diamond indenter are divided to get the Vickers hardness number (VHN).

The Vickers hardness, measured in kgf/mm^2, is obtained in practice using the formula:

$HV = 1.8544\ P_1/d_1$

where

P1 represents the force measured in kilograms-force (kgf),

d1 represents the length of the long diagonal measured in millimetres (mm).

Six points in all ± two for the base zone, ± two for the HAZ zone, and ± two for the fusion or weld zone are regarded as indentation points. Micro structural analysis is followed by 20 seconds of 500 g force applied to etched transverse cross sections of the welded specimens for micro hardness testing. Hardness of the specimen welded with low and high heat input is lowered at the weld zone. For the most part due to its more refined grain structure, the specimen produced with a moderate heat input exhibited the greatest levels of hardness. Table 5.3 presents the micro-hardness values for every sample. The varied qualities and compositions of the base and filler materials, dilution, heating and cooling cycles, and other pertinent parameters may be the cause of the poor results in certain places. Results of the hardness in different parts of the weldment are uniform.
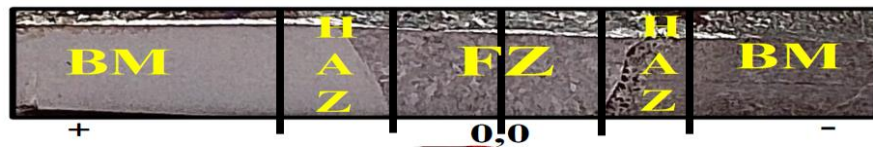

Figure 4.57 A schematic diagram of micro hardness measurements processes

Table 4.6 Micro hardness value for Ferritic SS 409M

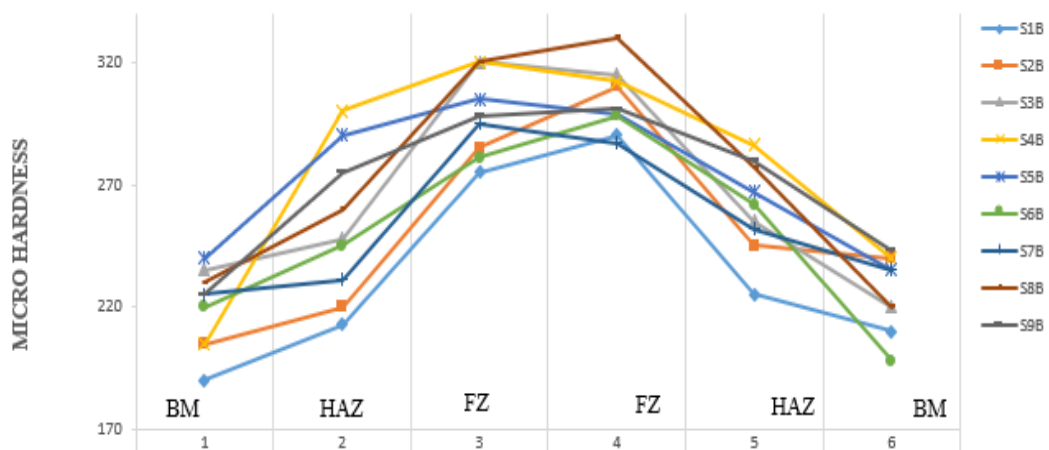| Sl. No.	Micro Hardness (HV) at position					
	BM	HAZ	FZ	FZ	HAZ	BM
S1B	190	213	275	290	225	210
S2B	205	220	285	310	245	240
S3B	235	248	320	315	255	220
S4B	205	300	320	312	286	240
S5B	240	290	305	299	267	235
S6B	220	245	281	298	262	198
S7B	225	231	295	287	252	235
S8B	230	260	320	330	277	220
S9B	225	275	298	301	280	243

Figure 4.58 Micro hardness graph for Ferritic SS 409M sample S1A to S9A

4.2.4 Microstructural Analysis of Ferritic SS 409M

The microstructure of the welded samples was analysed using the Leica DM LM metallurgical microscope (Figure 3.4). All the images were captured with a 100X and 200X zoom.
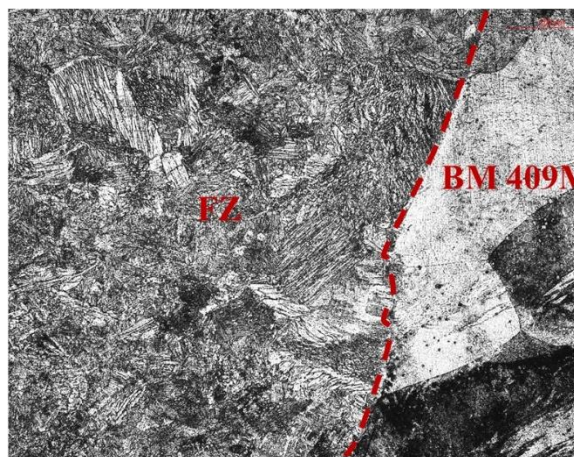
Figure 4.59 Metallographic image of S1B

Figure 4.60 Metallographic image of S1B

Figure 4.61 Metallographic image of S2B

Figure 4.62 Metallographic image of S2B

Figure 4.63 Metallographic image of S3B

Figure 4.64 Metallographic image of S3B

Figure 4.65 Metallographic image of S4B

Figure 4.66 Metallographic image of S4B

Figure 4.67 Metallographic image of S5B

Figure 4.68 Metallographic image of S5B

Figure 4.69 Metallographic image of S6B
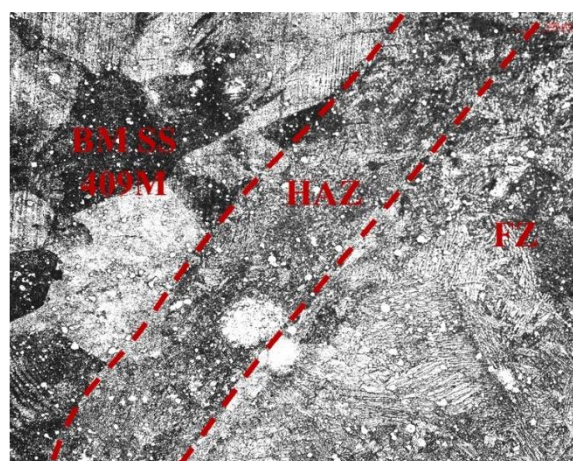
Figure 4.70 Metallographic image of S6B
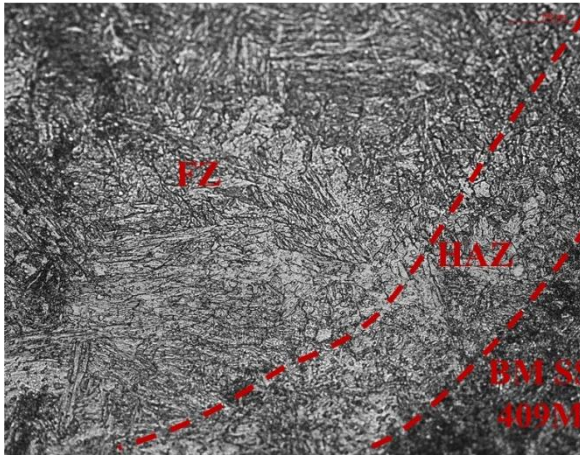
Figure 4.71 Metallographic image of S7B
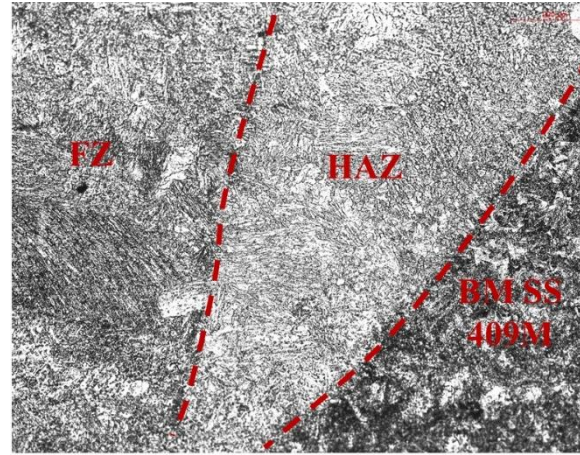
Figure 4.72 Metallographic image of S7B
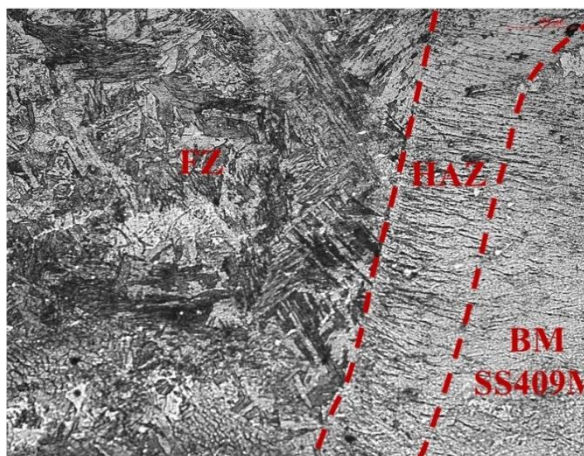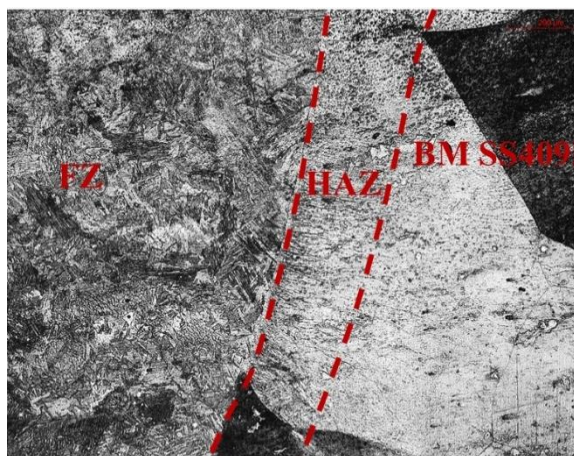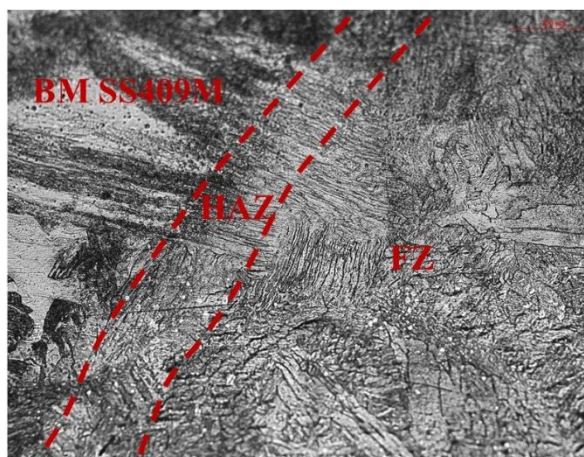

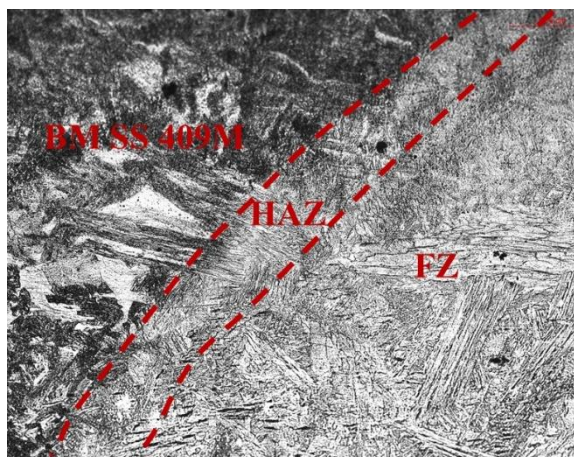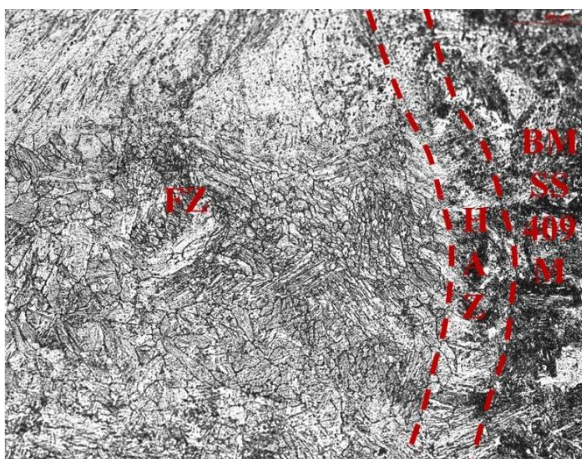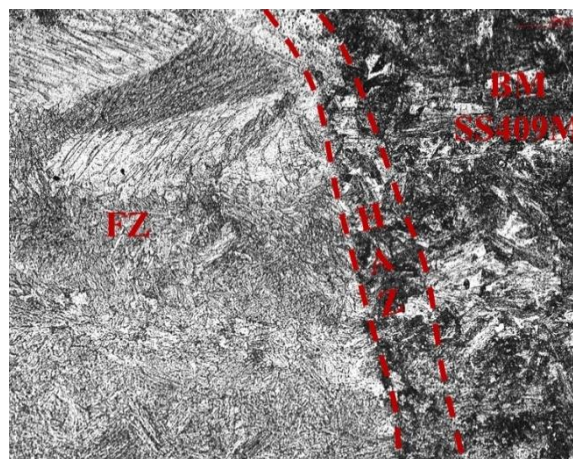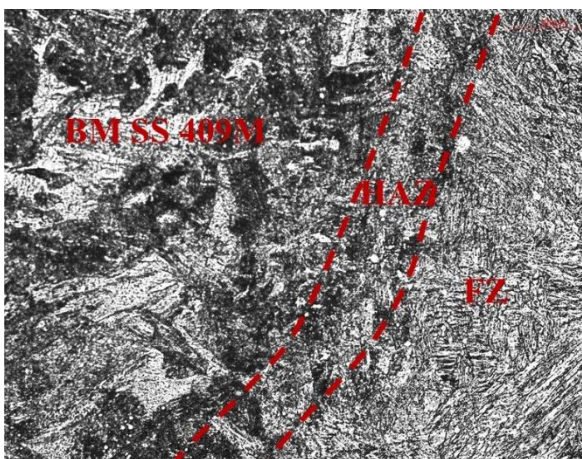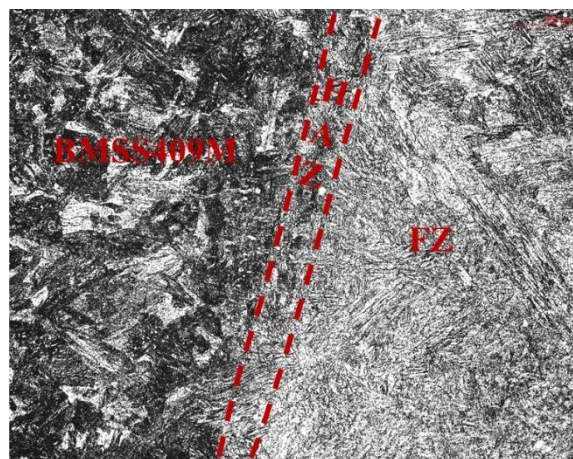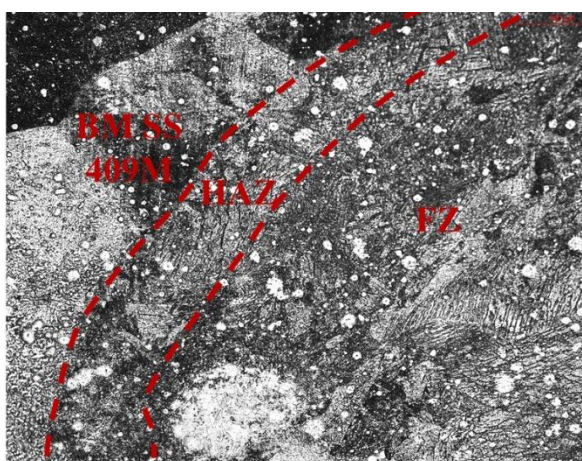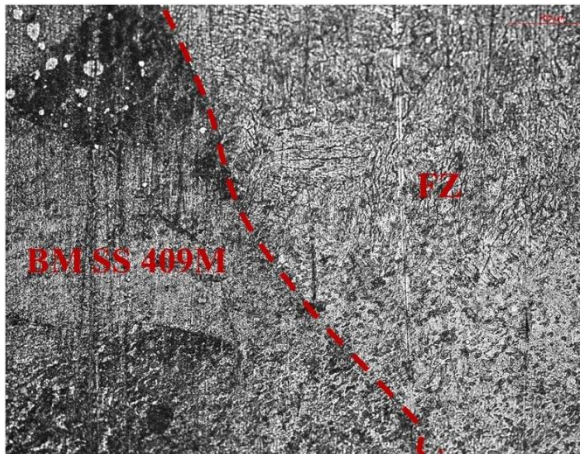Figure 4.73 Metallographic image of S8B
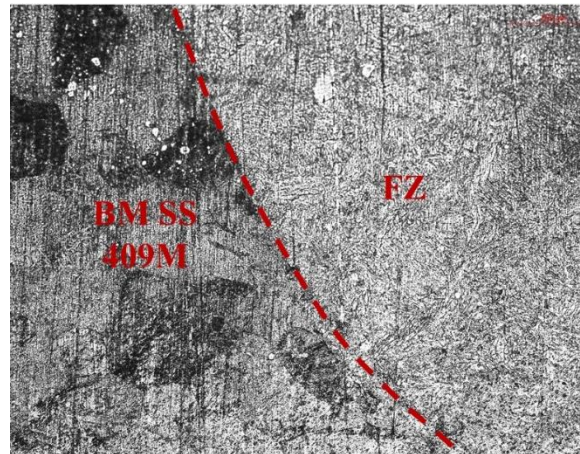
Figure 4.74 Metallographic image of S8B
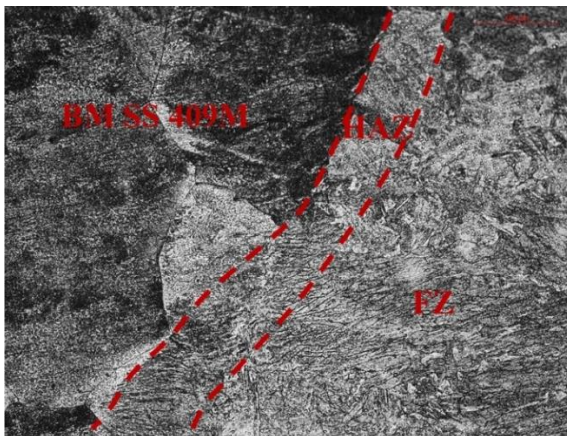
Figure 4.75 Metallographic image of S9B
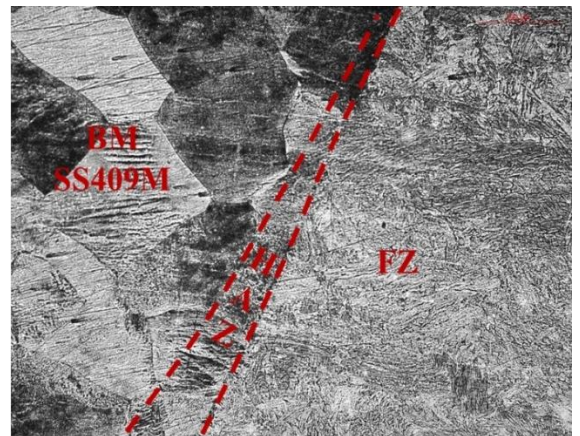
Figure 4.76 Metallographic image of S9B
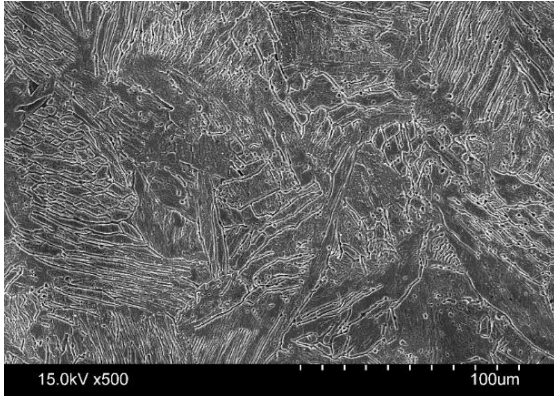
Figure 4.77 SEM image of SS 409M S9B   Figure 4.78 SEM image of SS 409M S1B
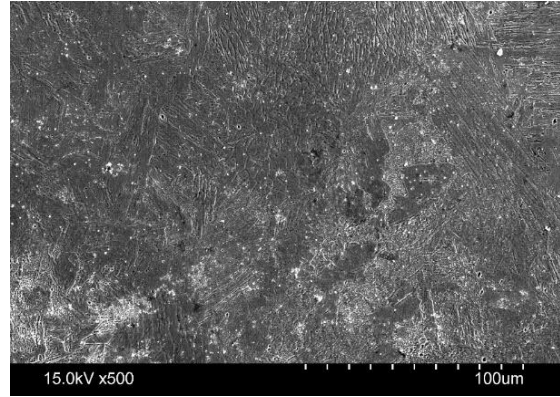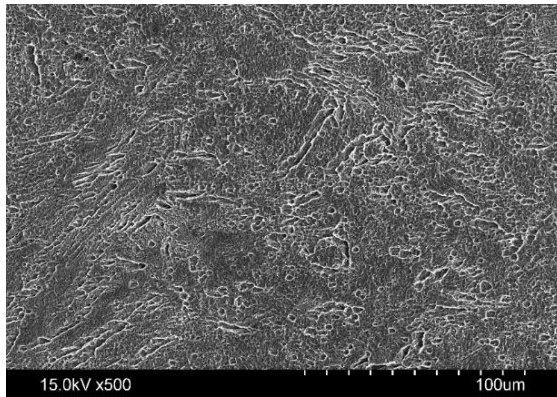
Figure 4.79 SEM image of SS 409M sample S5B

The SS 409M parent area showed alloy carbide particles mixed in with the ferrite grains. The thermodynamic stability of carbides, formed by various alloying elements in steels, is significantly greater than that of cementite. The microstructure of the base metal also exhibits a ferrite matrix in the longitudinal direction, which includes an extended layer of martensite. Figures 4.59 to 4.76 respectively, show the microstructure of nine samples. The Austenitic grains in HAZ are typically coarser compared to the base metal. This could be due to the slower cooling rate in the HAZ area. Figures 4.59, 4.63, and 4.65 display martensite structures, with some martensite present in HAZ. Also, close to the weld side, ferrite inclusions between the solid solution and austenite are visible in some figures. The microstructures of the weld metals in all the samples were compared to those of the base metal or the HAZ. The microstructures of the weld metals were seen to exhibit notable distinctions compared to both the base metal and the HAZ. Most of the samples demonstrated columnar dendritic growth with visible grain formations. The weld metal microstructures in all samples were compared to the base metal or the heat-affected zone (HAZ). The weld

metals' microstructures differed significantly from those of the base metal and HAZ. Most of the samples exhibited columnar dendritic growth and clear grain forms in samples S1B, S3B, S4B, S6B, S7B, and S8B, respectively. The microstructure analysis revealed that S1B and S9B had the lowest and highest UTS in the tensile test results. It was during TIG welding that the cooling rate, heat gradient, and unique properties of Ferritic steel came together to make columnar dendritic growth structures. The heat gradients and cooling rates inside the weld pool determine the direction of dendritic development, resulting in columnar formations.

Several different characteristics, such as the composition of the base and filler materials, the amount of dilution, the heating and cooling cycles, and a few elements, influence the microstructures generated in different regions of the weld beads. Each of the nine samples exhibited minimal variations in their microstructures. Various parametric parameters, especially those related to heating and cooling variations, influence the welding combinations. These factors include heat input, travel speed, and cooling cycle characteristics. As a result, microstructures are directly influenced by this process.

4.2.5 Weld Bead Profile Measurement and Discussion

Stereo microscopes measure the weld bead profile (Figure 3.7). Table 4.5 lists the welding configurations and related weld bead geometry; all weld bead figures are provided below.
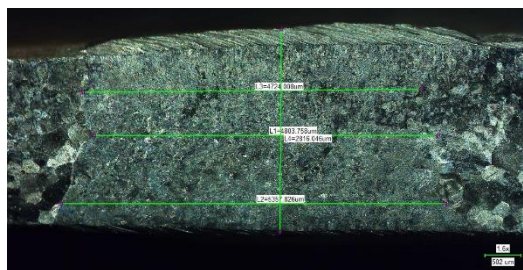
Figure 4.80 weld bead profile S1B   Figure 4.81 weld bead profile S2B
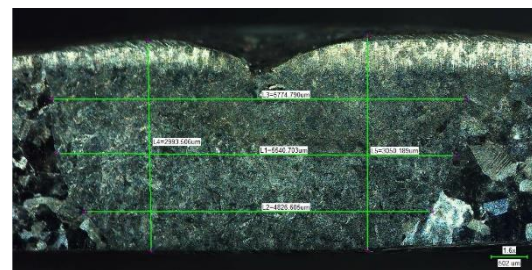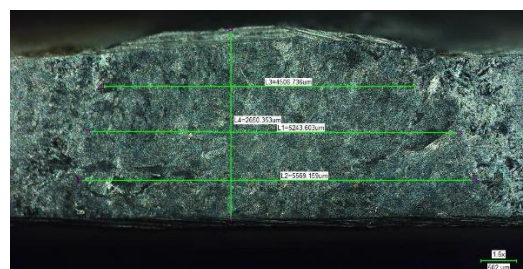
Figure 4.82 weld bead profile S3B   Figure 4.83 weld bead profile S4B
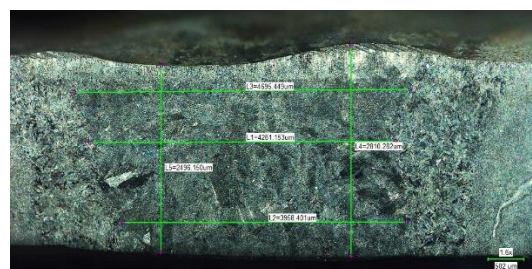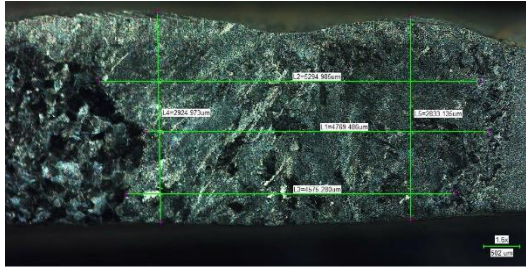
| Figure 4.84 weld bead profile S5B | Figure 4.85 weld bead profile S6B |

| Figure 4.86 weld bead profile S7B | Figure 4.87 weld bead profile S8B |
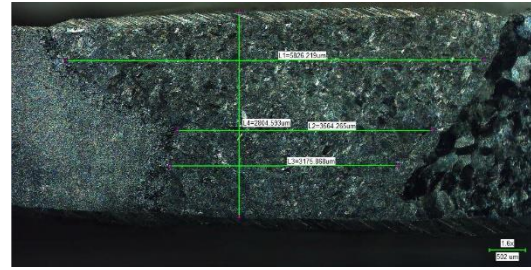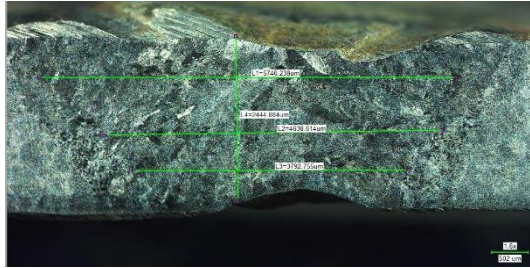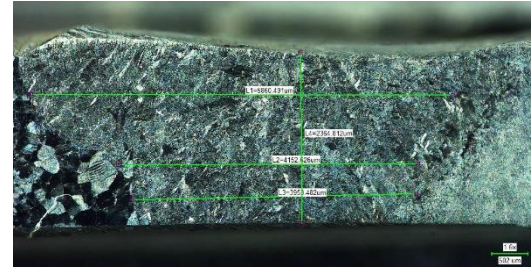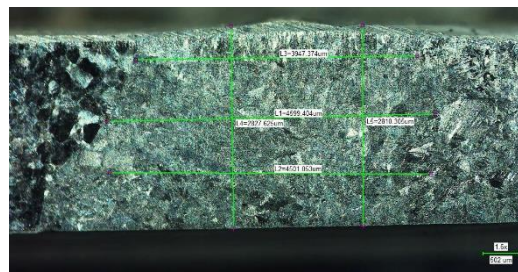
Figure 4.88 weld bead profile S9B

From figure 4.81 sample number S2B bead width found maximum and depth of penetration is maximum and minimum beads width found figure 4.85 sample number S6B, minimum depth of penetration observed on sample figure 4.87 sample number S8B. TIG welding produces maximum bead width and minimal depth of penetration mostly because to the reduced heat input, concentrated and steady arc, and exact control over welding settings. Wider beads are produced by the equal distribution of heat across the surface, but the depth of penetration is restricted by the low heat input as well as the rapid cooling rate. The analysis of weld bead geometry is performed with the objective of identifying the factors that are most effective in producing the anticipated shape of the weld bead.

4.3 Results and Discussion

Results and discussion for ASS 304L and FSS 409M combination of dissimilar welded samples.

4.3.1 Results and Discussion of Dissimilar TIG Welding of ASS 304L and FSS 409M

The dissimilar welding of Austenitic and Ferritic stainless steel using ER308L filler wire was carried out in the third set of experiments, following the completion of the first and second sets of experiments. Using Taguchi L$_9$ orthogonal design, the experiments are constructed. The results are presented and described in the following paragraphs.

4.3.1.1 Visual Inspection and X-ray Radiography Test Results for the Dissimilar Welding of ASS 304L and FSS 409M

After performing the all experiments all the samples are examined by X ray radiography test to finding the quality of weld. All the samples are seen defect free but same samples are found minor defects. All results are given bellow.

Table 4.7 Results of X- ray test and visual inspection on Austenitic SS 304L and Ferritic SS 409M as per Taguchi L$_9$ design of experiment

Sl. No.	Current (A)	Travel speed (mm/min)	Gas flow rate (l/min)	Visual inspection	X-ray test result
S1A	95	2	10	No defects	Porosity
S2A	95	2.5	15	Excessive deposition	Lack of Fusion
S3A	95	3	20	No defects	No defects
S4A	105	2.5	10	No defects	No defects
S5A	105	3	15	No defects	No defects
S6A	105	2	20	No defects	No defects
S7A	115	3	10	No defects	No defects
S8A	115	2	15	No defects	No defects
S9A	115	2.5	20	No defects	No defects
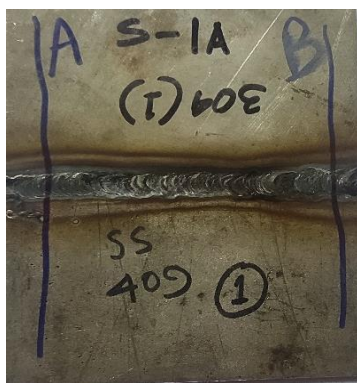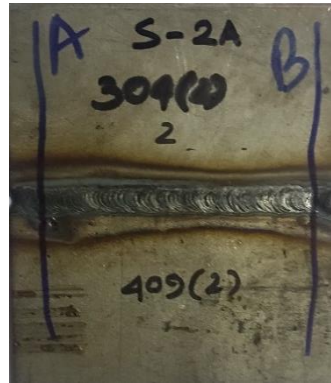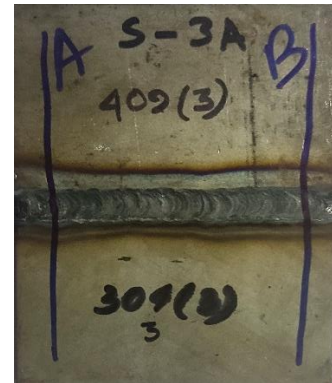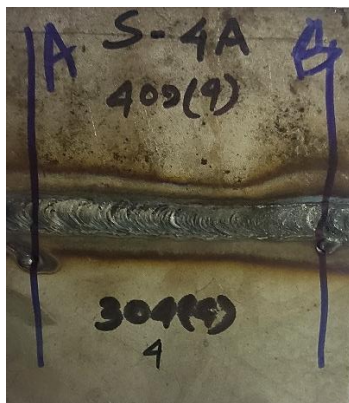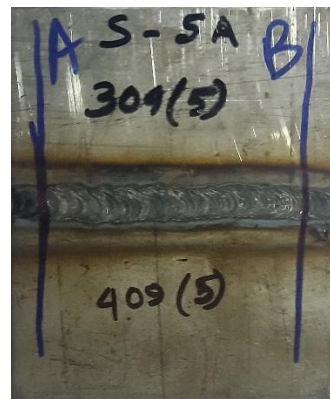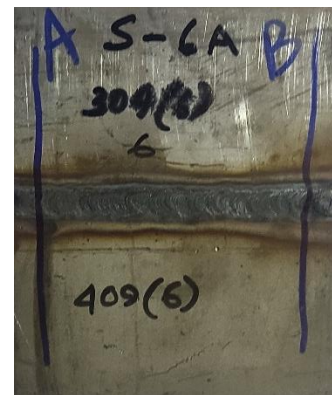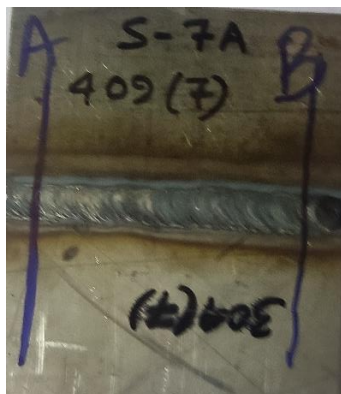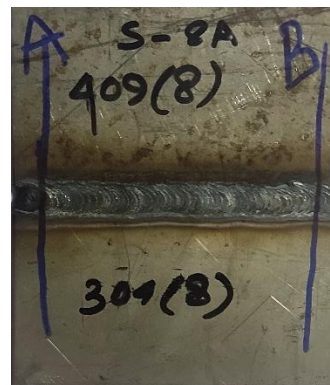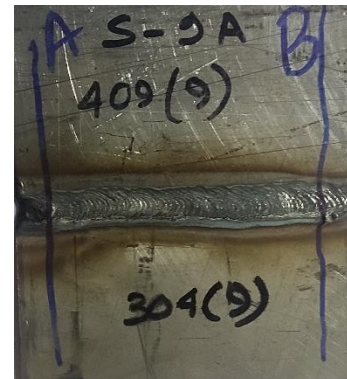
Figure 4.89 Disimilar welding of Austenitic SS 304 L and Ferritic SS 409 M (a- i) total numbers of welding plates

4.3.1.2 X-ray Radiography Test Results and Discussions of Dissimilar welding of ASS 304L and FSS 409M

After visual inspection using XXQ-2005 X-ray defect detector, all-welded samples were X-ray to assess their interior soundness. Figure 4.90 show X-ray radiographs of all samples (S1 to S9 respectively), and Table 4.7 shows the findings of visual inspection and X-ray radiography. The pictorial views of the X-ray films are shown in figures 4.90.

(a)	(b)	(c)
(d)	(e)	(f)
(g)	(h)	(i)
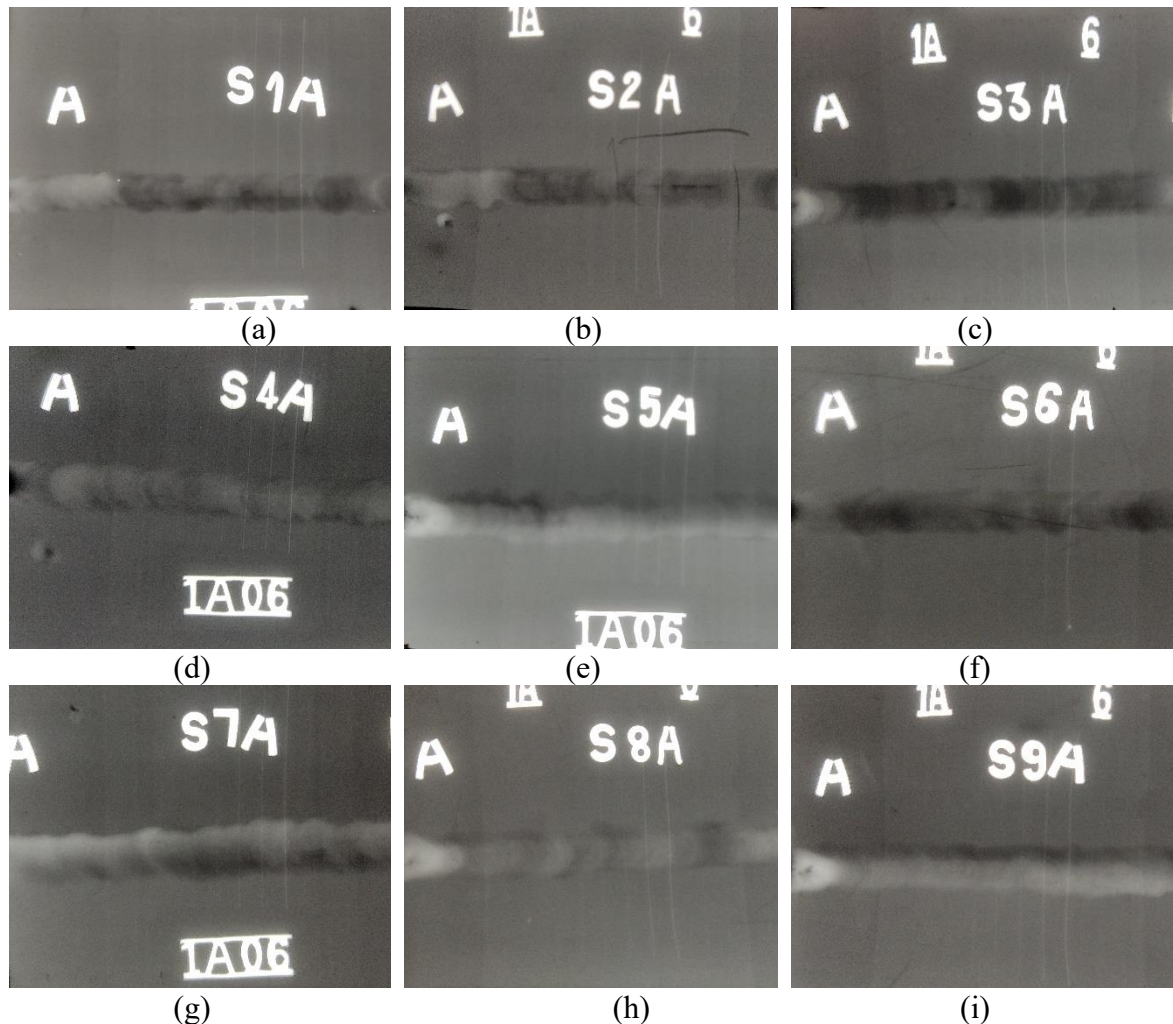
Figure 4.90 X-ray radiographic film for dissimilar welding of Austenitic SS 304L to Ferritic SS 409M (a - i) total samples

The lack of root or lack of side wall fusion of the weld may have happened because of to the insufficient current flow, inadequate cleaning, high speed of the welding torch, and the presence of oxides, and other impurities that prevent appropriate fusion between the

deposited metal and the base metal. The lack of penetration problem may also be caused by any imperfections in the base metal or filler wire, as previously indicated during visual examination. This kind of problem may also be caused by an abnormal electrode angle.

An insufficient heat input cannot ensure sufficient melting of the weld material. During the process of the metal's solidification, sample number S2A shows porosity, which is probably the result of gas being trapped within the composition of the metal. Porosity is a big problem that should be resolved, yet doing so is a considerable task itself. Initially the contamination of the shielding gas, secondly the contamination of the filler metal, and finally the contamination of the base metal are probably the most important reasons that are contributing to this problem.

4.3.2 Tensile Test Results and Discussion of Dissimilar Welding

After the completion of the non-destructive testing, the destructive testing was carried out. A table contains the results of the tensile test that was performed. A comprehensive range of tensile parameters, including UTS, and % of elongation, were included into the results.

Table 4.8 Tensile test table for dissimilar welding of Austenitic SS 304L and Ferritic SS 409M

Sl. No.	UTS (MPa)	PE % of elongation	BW (mm)	DP (mm)	Fracture zone
S1A	525.33	20.40	5.900	2.537	BM
S2A	522.33	18.76	4.912	2.456	BM
S3A	542.68	19.40	6.032	2.440	BM
S4A	536.50	17.69	6.732	2.593	BM
S5A	597.14	25.9	6.300	2.804	BM
S6A	644.53	30.66	5.037	2.770	BM
S7A	590	33	5.403	2.045	BM
S8A	542.6	20.4	5.723	2.359	BM
S9A	632.92	48.10	5.438	2.164	BM

Stress vs Strain Plots for welded samples

The stress vs. strain curve offers essential insights into the mechanical properties of materials, enabling the enhancement of material design, selection, and utilisation in industry and

engineering. All butt-welded samples numbered from 1 to 9 have their stress vs strain curves depicted in figures 4.91 through 4.99.
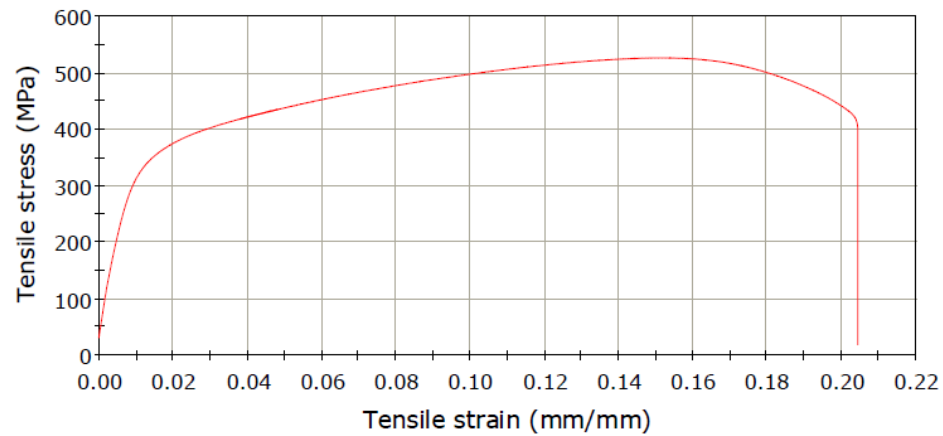
Figure 4.91 Stress vs Strain curves of welded sample no. S1A
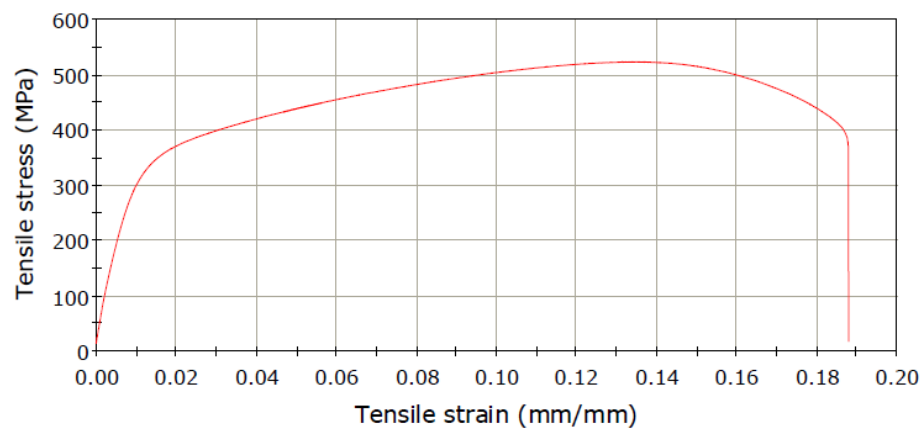
Figure 4.92 Stress vs Strain curves of welded sample no. S2A
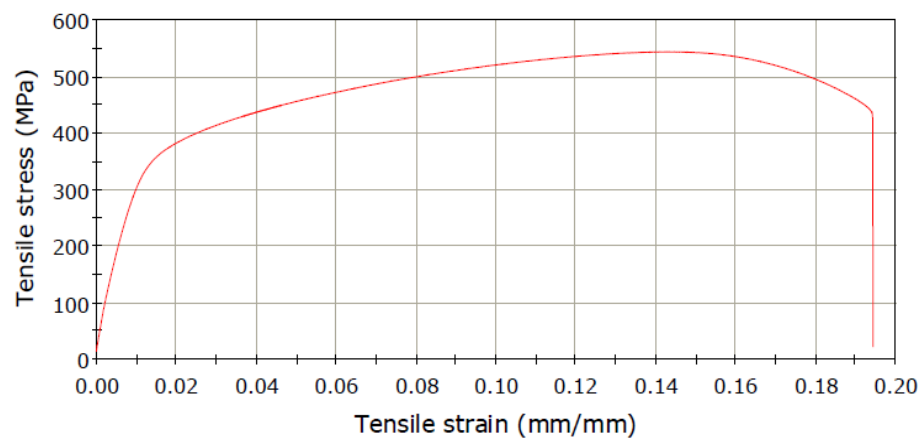
Figure 4.93 Stress vs Strain curves of welded sample no. S3A
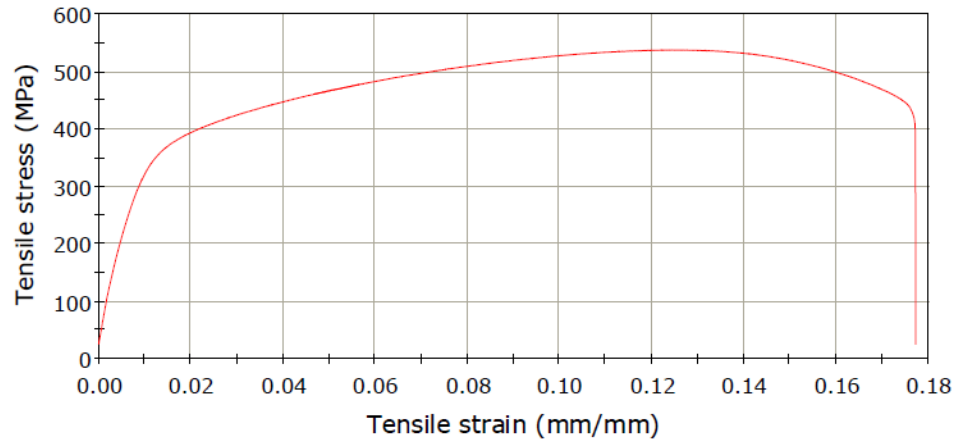
Figure 4.94 Stress vs Strain curves of welded sample no. S4A
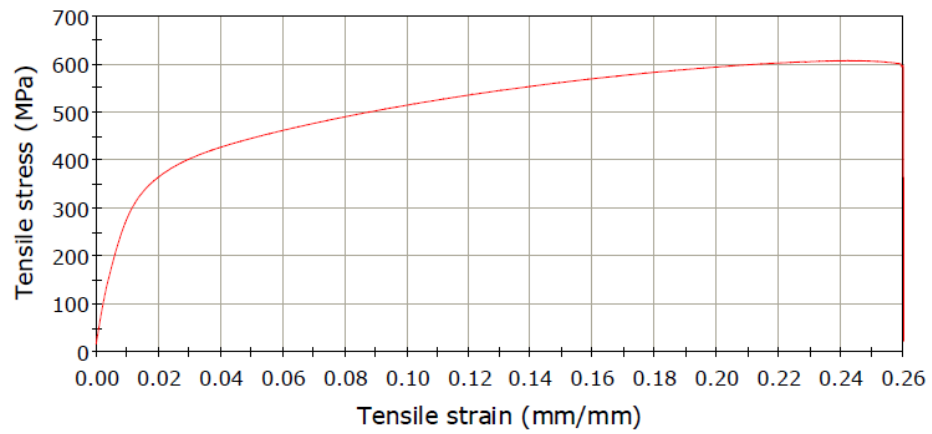
Figure 4.95 Stress vs Strain curves of welded sample no. S5A
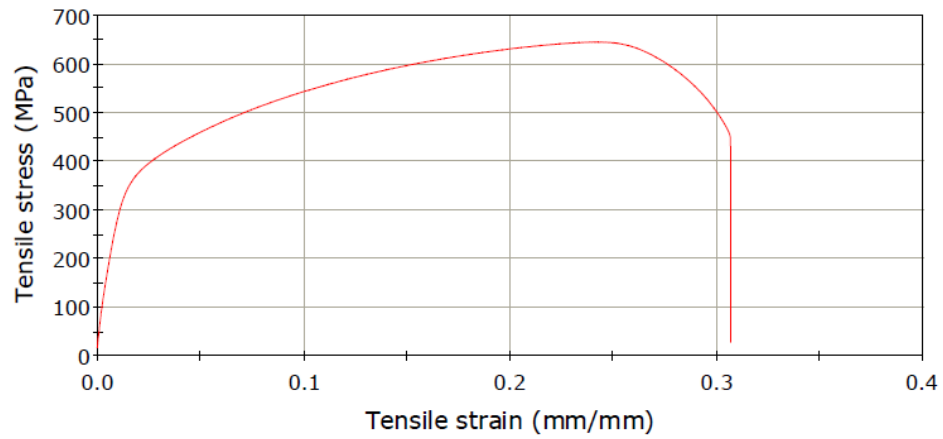
Figure 4.96 Stress vs Strain curves of welded sample no. S6A

90
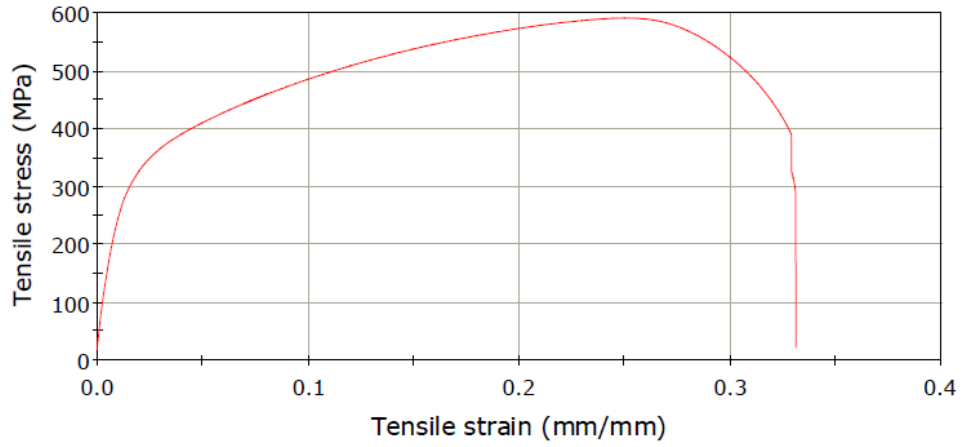
Figure 4.94 Stress vs Strain curves of welded sample no. S7A
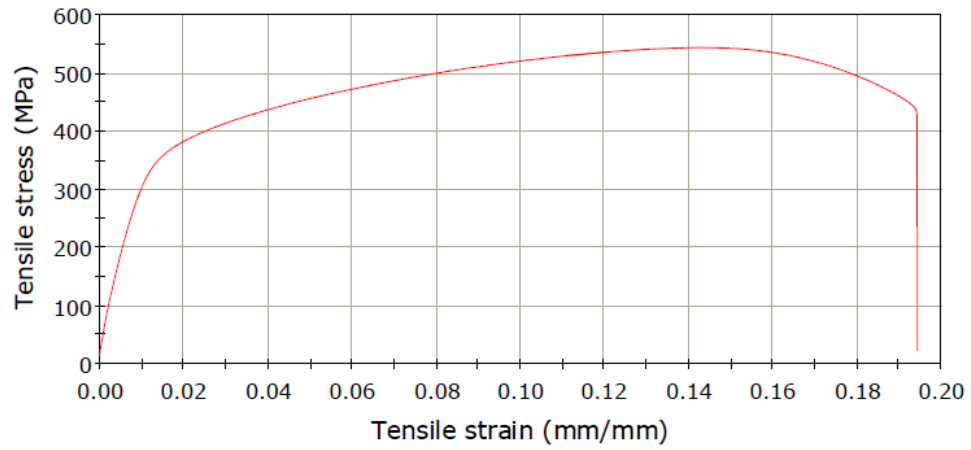
Figure 4.98 Stress vs Strain curves of welded sample no. S8A
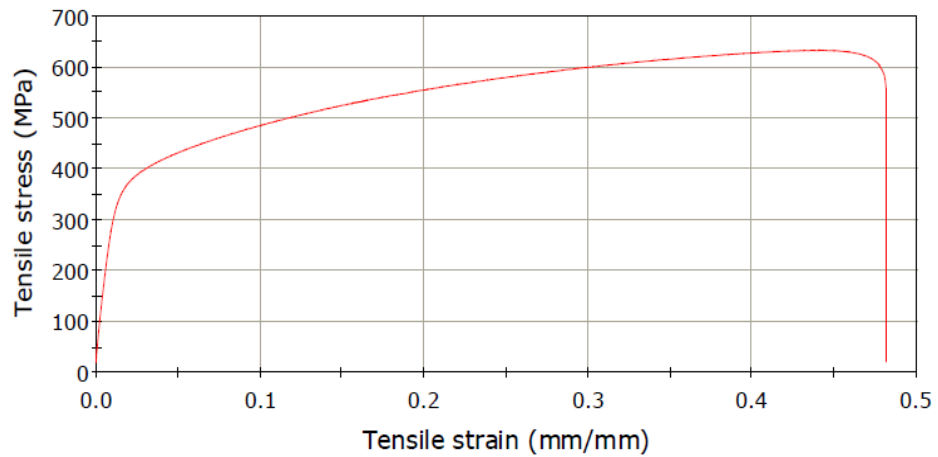
Figure 4.99 Stress vs Strain curves of welded sample no. S9A

Figures 3.9 and 3.4 depict the creation of the tensile test specimens following the guidelines of ASTM E8M-04. The tensile test has been carried out at room temperature using the Instron universal testing system. The experiment conducted three repetitions of tensile testing on each sample, following the ASTM-E8 standard. Table 4.8 displays the outcomes of the average tensile test for each sample. Upon investigation, it is evident that all samples are fractures from the base zone due to inadequate heat input. This indicates that the parent material is much weaker than the welded zone and so many cause are there for breaking base zone like residual stress development, microstructural changes etc. The Figures 4.91 to 4.99 show the tensile stress vs strain curve for samples S1A to S9A, respectively and all the graphs are ductile nature. The UTS achieved is 644.53 MPa, which is the greatest value achievable under moderate high heat input conditions. The sample labelled as S9A exhibited the most percentage elongation, with a value of 48.10%. The sample labelled as S4A demonstrates the lowest value of percentage elongation, which is 17.69.

4.3.3 Micro Hardness Analysis of Dissimilar welding

Vickers micro hardness testing machine, UHL VMTH (Figure 3.5) are used for measuring micro hardness. The VHN is calculated by dividing the applied force on the Vickers indenter by the contact surface area of the permanent imprint produced by the diamond indenter. The Vickers hardness, measured in kgf/mm^2, is obtained in practice using the formula:

HV = 1.8544 P_1/d_1

Where,

P1 represents the force measured in kilograms-force (kgf),

d1 represents the length of the long diagonal measured in millimetres (mm).

The indentation points are taken at ± two each nearest area at base zone, ± two for HAZ zone and ± two for fusion zone or weld zone total six points are taken. Micro hardness experiments on etched transverse cross sections of the welded specimens under a force of 500 g for duration of 20s, after micro structural analysis. The weld zone of the specimen welded with low and high heat input exhibits reduced hardness. The highest levels of hardness were seen in the specimen that was created with a moderate heat input, mostly because of its more refined grain structure. The micro-hardness results for all the samples are shown in table 4.9. Some areas exhibit unsatisfactory results, which may be due to several factors such as the

different materials properties and compositions of the base and filler materials, dilution, heating and cooling cycles, and other relevant parameters. The hardness in various areas of the weldment exhibits consistent results.
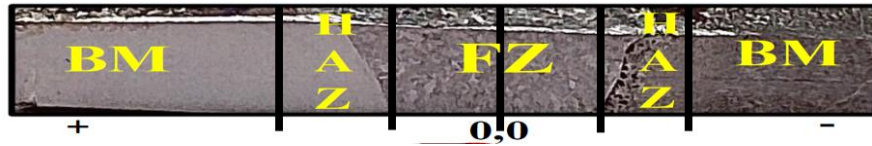
Figure 4.100 A schematic diagram of micro hardness measurements processes

Table 4.9 Micro hardness value for dissimilar welding Austenitic SS 304L and Ferritic SS 409M

Sample No.	Micro Hardness (HV) at position					
	BM	HAZ	FZ	FZ	HAZ	BM
S1A	192	215	278	289	225	208
S2A	205	218	286	308	244	228
S3A	235	245	318	315	255	220
S4A	225	305	320	312	286	230
S5A	235	290	303	299	267	245
S6A	220	245	281	298	262	198
S7A	225	231	292	287	252	235
S8A	240	287	340	339	277	248
S9A	228	290	298	301	283	243
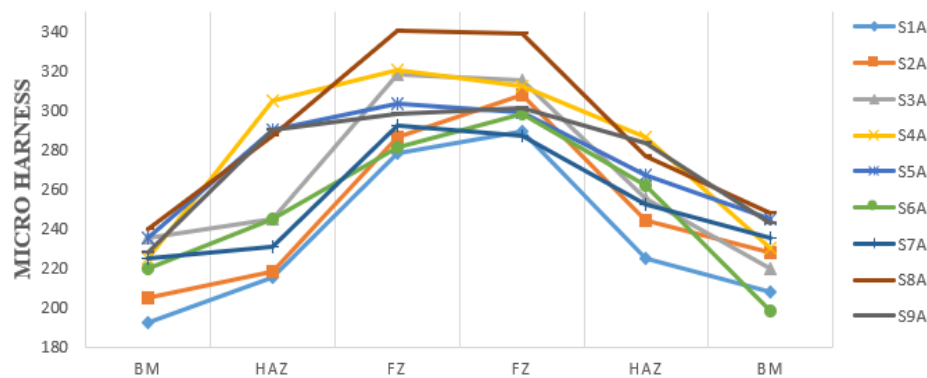
Figure 4.101 Micro hardness graph for Austenitic SS 304L to Ferritic SS 409M dissimilar welding

93

4.3.4 Microstructural Studies of Austenitic SS 304L and Ferritic SS 409M Specimens

The Leica DM-LM metallurgical microscope have been used to investigate the microstructure of the welded samples (Figure 3.4). The photographs were taken with 100X and 200X magnification. Figures 4.102 to 4.119 display the optical microscope study of the microstructural development during TIG welding of SS 304L and SS 409M stainless steels. The samples examined are labelled S1A to S9A. Three distinct microstructures are detected in the base zone, heat-affected zone and fusion zone. The microstructural analysis shows that there are three separate phases in the fusion zone of the different places where SS 304L and SS 409M stainless steel meet. The three phases are austenite, ferrite, and martensite. Furthermore, this region exhibits consistent columnar dendritic formations. In the welded metal area, widmanstatten ferrite has formed. Ferrite has a coarse and extended morphology. Higher cooling rates are known to accelerate the formation of ferrite, namely polygonal ferrite, at temperatures somewhat lower than those required for equiaxed ferrite formation. Figure 4.02, 4.106, and 4.108 illustrates the microstructure of the weld metal of SS 304L and SS 409M dissimilar joint.
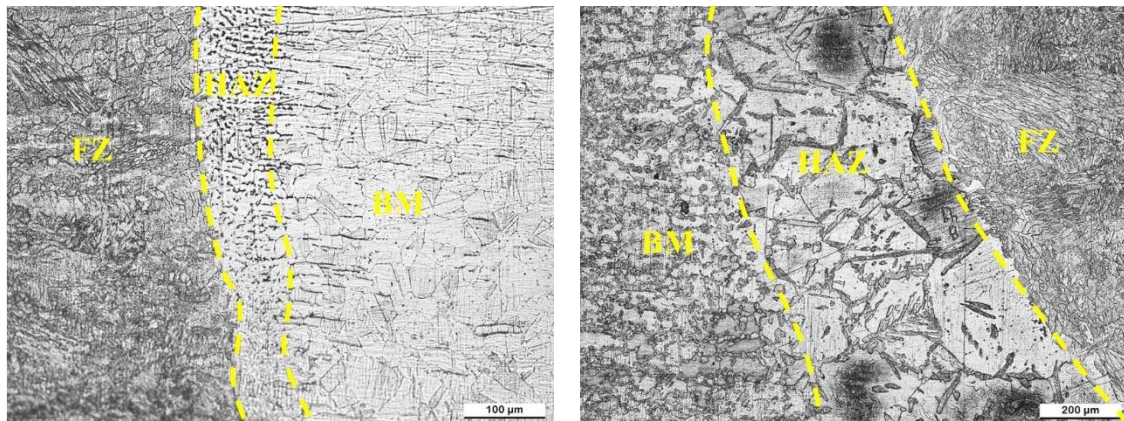
Figure 4.102 Metallographic image of S1A   Figure 4.103 Metallographic image of S1A
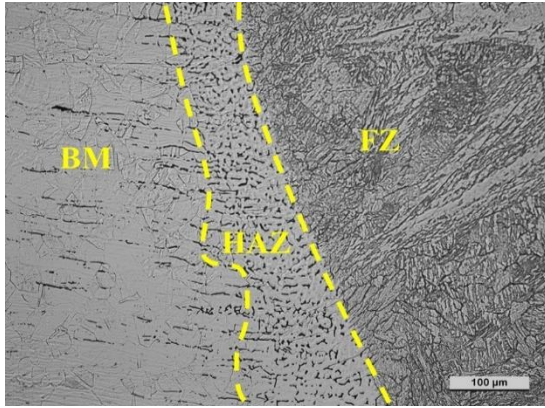
Figure 4.104 Metallographic image of S2A
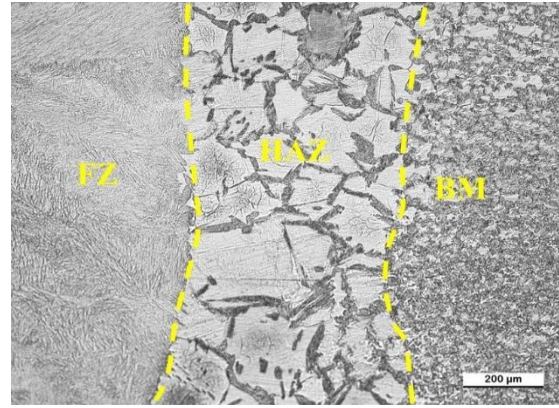
Figure 4.105 Metallographic image of S2A
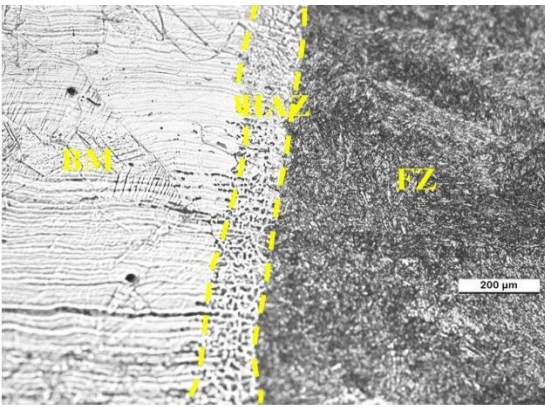
Figure 4.106 Metallographic image of S3A
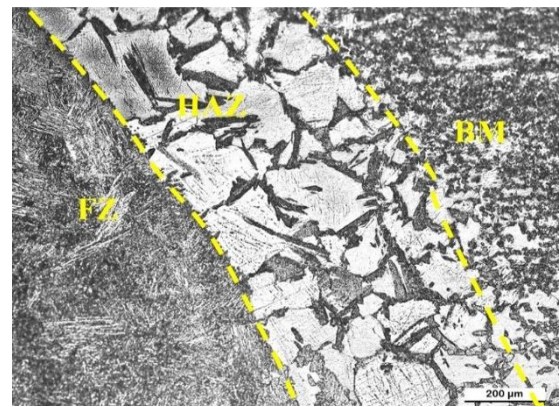
Figure 4.107 Metallographic image of S3A

The examination of 304L and 409M stainless steel's microstructure revealed the presence of equiaxed austenite grains. All of them on the Austenitic side exhibited the same HAZ microstructure: δ-ferrite, which remained unaffected at the austenite's grain boundaries. Compared to the microstructure of the base metal (BM), the heat-affected zone (HAZ) often had a finer structure, which might lead to improved mechanical characteristics.
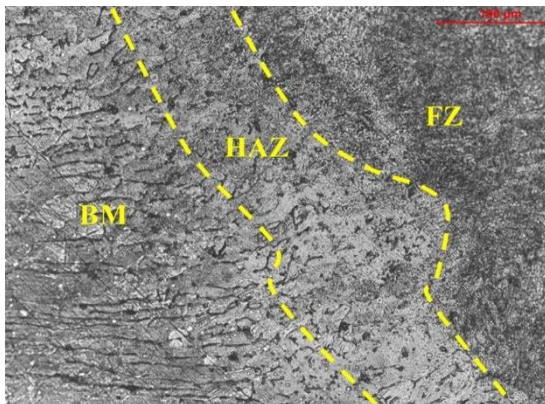
Figure 4.108 Metallographic image of S4A
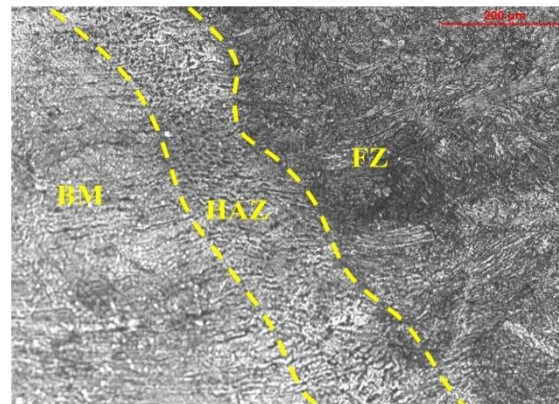
Figure 4.109 Metallographic image of S4A

95
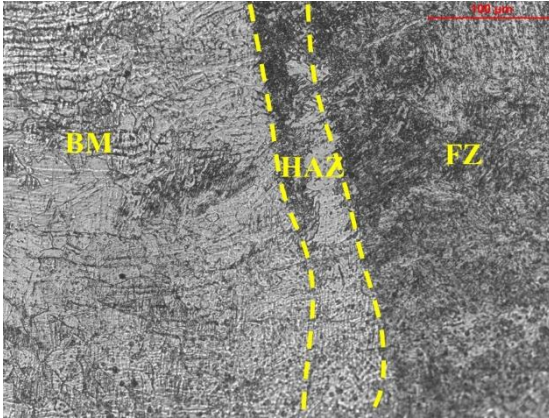
Figure 4.110 Metallographic image of S5A   Figure 4.111 Metallographic image of S5A
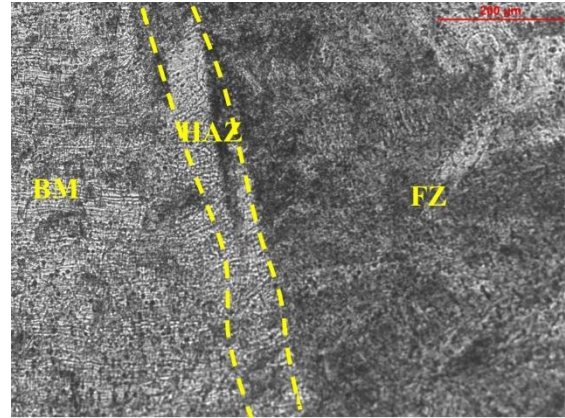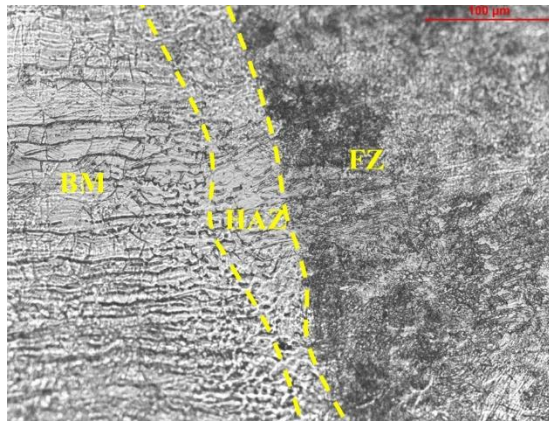
Figure 4.112 Metallographic image of S6A   Figure 4.113 Metallographic image of S6A
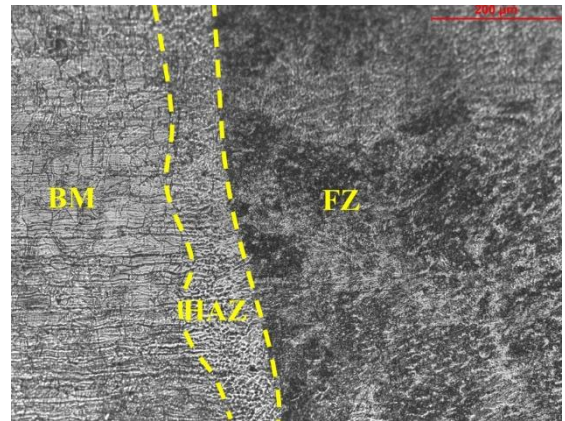
The figure also displays columnar dendritic structures. Figure 4.104 shows that sample S2A, S9A exhibits a columnar dendritic structure. In dissimilar welding, the join of two different metals may result in the formation of distinct microstructural characteristics, such as columnar dendrites. These features are a result of variations in the thermal properties and solidification rates of the used metals.
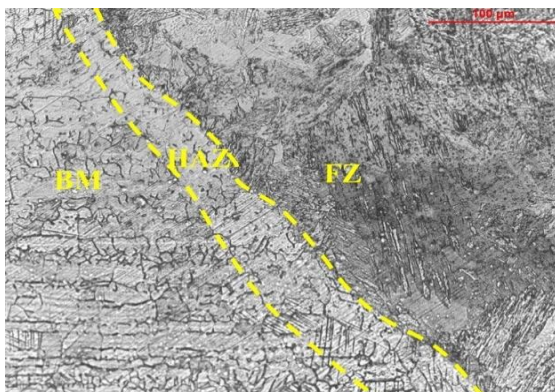
Figure 4.114 Metallographic image of S7A   Figure 4.115 Metallographic image of S7A
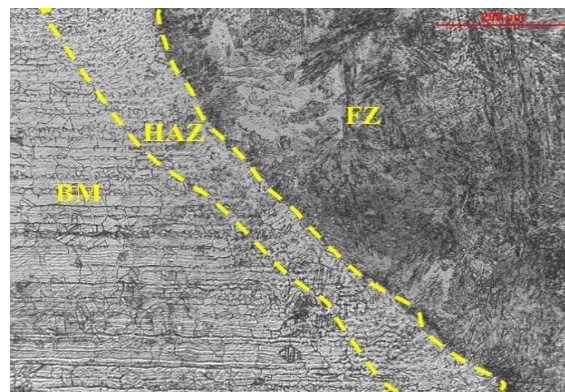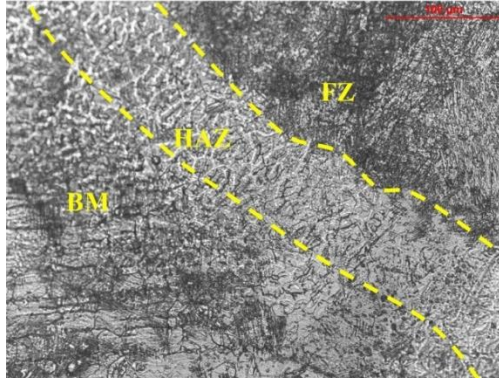
Figure 4.116 Metallographic image of S8A
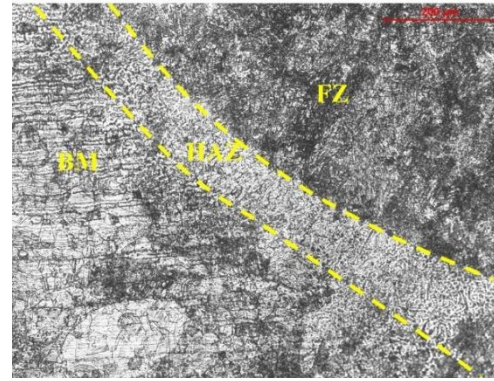
Figure 4.117 Metallographic image of S8A
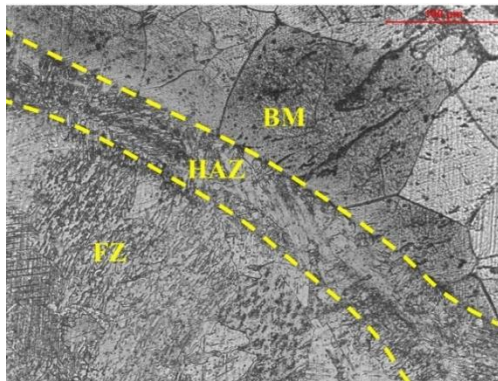
Figure 4.118 Metallographic image of S9A
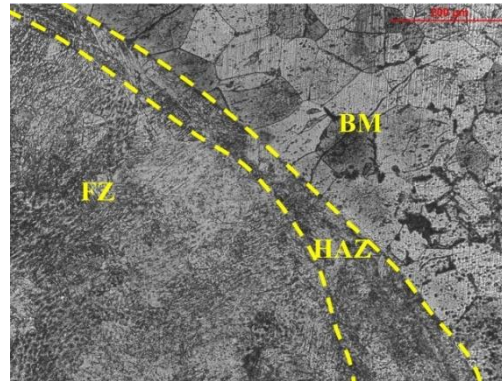
Figure 4.119 Metallographic image of S9A

Additionally, the cycles of heating and cooling conditions strongly impact the microstructure. The Heat Affected Zone is affected when high amounts of heat are introduced into the material because this increases the flowability of the substance. In general, the formation of smaller grains occurs when the cooling rate is increased, and the generation of a coarse grain structure occurs when the cooling rate is decreased. In general, the microstructures of the welds that were found in this site display a consistent distribution of very small grains with very little variance.
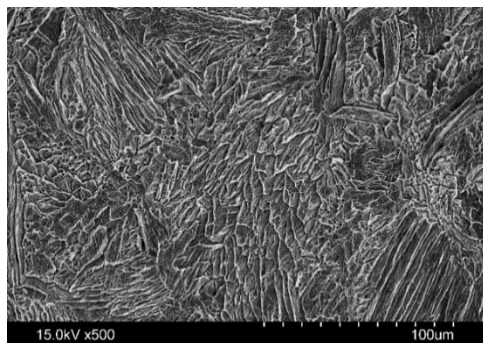
Figure 4.120 SEM image of S6A
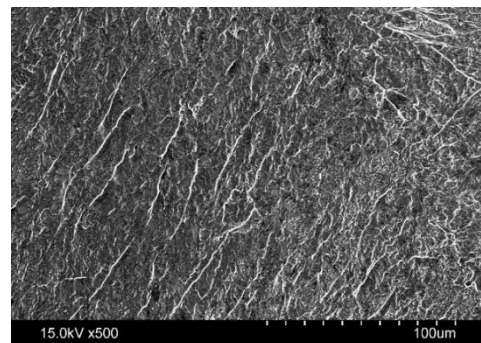
Figure 4.121 SEM image of S2A
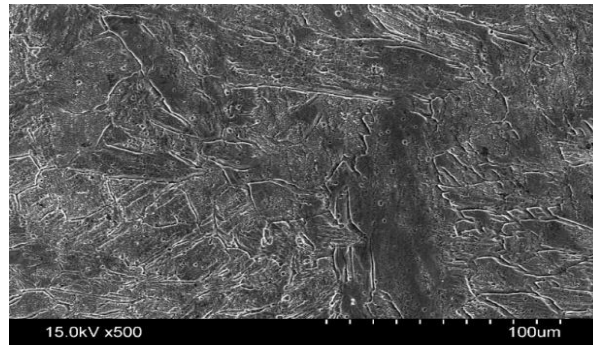
Figure 4.122 SEM image of S5A

4.3.5 Weld Bead Profile Measurement and Discussion

Stereo microscopes measure the weld bead profile (Figure 3.7). Table 4.2 lists the welding configurations and related weld bead geometry; all weld bead figures are provided below.
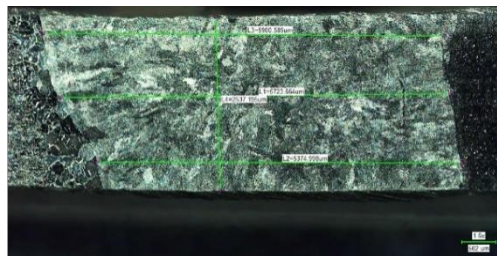
Figure 4.123 weld bead profile S1A
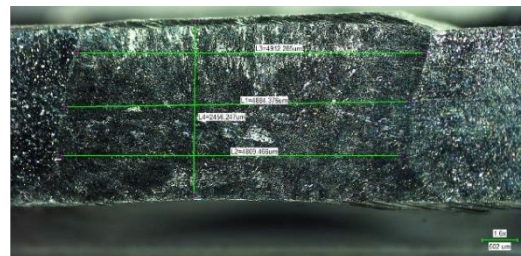
Figure 4.124 weld bead profile S2A
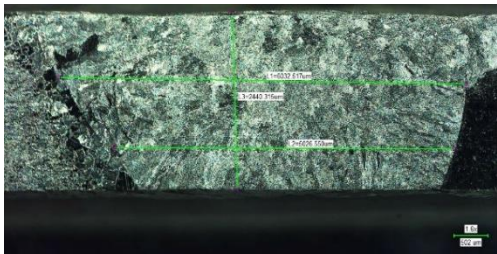
Figure 4.125 weld bead profile S3A
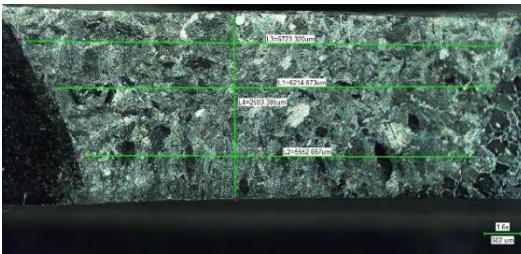
Figure 4.126 weld bead profile S4A
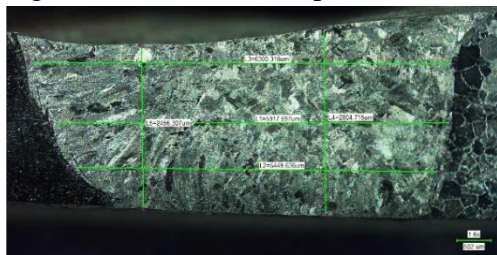
Figure 4.127 weld bead profile S5A
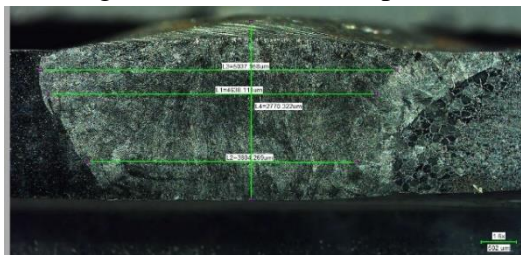
Figure 4.128 weld bead profile S6A

From figure 4.126, S4A bead width found maximum and depth of penetration is minimum S7A, on other hand figure 4.124 sample S2A bead width is minimum and maximum depth of penetration found S5A figure 4.127. TIG welding produces maximum bead width and

minimal depth of penetration mostly because to the reduced heat input, concentrated and steady arc, and exact control over welding settings.
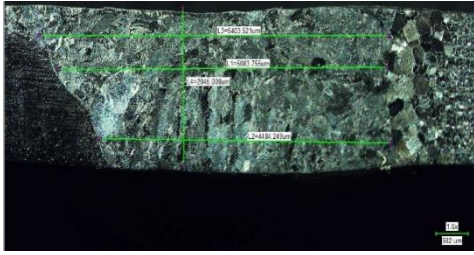
Figure 4.129 weld bead profile S7A   Figure 4.130 weld bead profile S8A
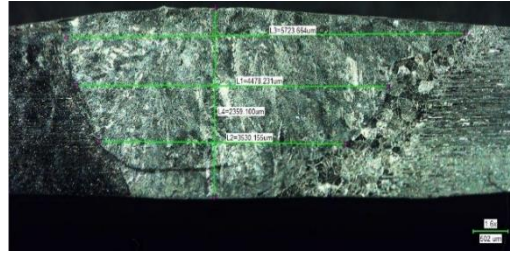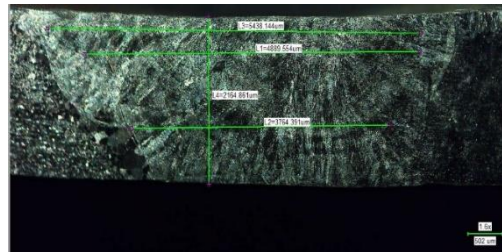
Fig 4.131 weld bead profile S9A

Wider beads are produced by the equal distribution of heat across the surface, but the depth of penetration is restricted by the low heat input as well as the rapid cooling rate. By analysing the geometry of weld beads, one can ascertain the parameters that are most effective in producing the desired shape of the weld beads.

The summary of this chapter may be drawn in this way that in case of similar welding (i.e. ASS 304L with ASS 304L) of defect-free samples were obtained under optimum welding conditions, exhibiting high tensile strength ranging from 612.9 MPa to 650.14 MPa and a hardness of 423 HV in the weld zone. For studying microstructure view analysis, the base metal is pure Austenitic stainless steel, and it was observed that the weld metal features equiaxed grains formed along with areas of columnar dendritic growth. In case of other similar welding (i.e. FSS 409M with FSS 409M) most of the defect-free samples were obtained under optimum conditions, with ultimate tensile strength (UTS) ranging from 432.5 MPa to 498.9 MPa. The base material comprises of Ferritic matrix containing coarser Austenitic grains. It was observed that the gas flow rate and travel speed had more significant impact on the tensile properties than the welding current. In case of dissimilar welding for defect free joints the ultimate tensile strength was obtained 644.53 MPa for SS 304L and SS 409 combination. The ferrite matrix comprises of austenite along the grain boundaries, while the weld metal is mainly composed of austenitic grains.

In this chapter analysis of the experimental results has been discussed.

5.1 Experimental investigation of three different steel materials

The analyses have been carried out individually for three sets of experimental results: TIG welding of i) Austenitic SS 304L to Austenitic SS 304L similar welding ii) Ferritic SS 409M to Ferritic SS 409M similar welding and iii) Austenitic SS 304L to Ferritic SS 409M dissimilar welding. For this experimental purpose, two optimization tools are utilized: i) GRA (Grey Taguchi technique), ii) TOPSIS (Technique for Order of Preference by Similarity to Ideal Solution) technique.

5.1.1 Results and analysis of SS 304L using L$_9$ Array

The Grey based Taguchi approach has been utilized for multi-objective optimization. The experimental data is linearly normalized within the range of "0" to "1", this process also known as Grey relational generation. The experimental data is derived from Table 4.2 in chapter 4. The normalization of experimental data is determined using equation (2.2), which follows the larger-the-better principle. The process of normalizing experimental data is illustrated in Table 4.2.

Table 5.1 Data normalization using the Taguchi L$_9$ orthogonal array experimental design

Sl. No	UTS (MPa)	Elongation %	BW (mm)	DP (mm)
S1	0.4189	0.59222	0.85227	1
S2	0.21079	0.37884	0.54545	0.73224
S3	0.16595	0.62086	0.77273	0.74863
S4	0.90763	0.50332	0.10227	0
S5	1	1	1	0.46995
S6	0	0.67209	0	0.3224
S7	0.50752	0	0.34091	0.12022
S8	0.49141	0.62688	0.32955	0.53005
S9	0.913	0.77758	0.375	0.30601

Grey Relation Coefficients for 304L were designed by Taguchi L$_9$ array matrix and calculated through the equation (2.6) is shown in table 5.2

Table 5.2 Experimental design based on the Grey relational coefficient and the Taguchi L$_9$ orthogonal array

Sl. No	UTS (MPa)	Elongation %	BW (mm)	DP (mm)
S1	0.462494	0.550797	0.77193	1
S2	0.387836	0.445968	0.52381	0.651246
S3	0.374799	0.568735	0.6875	0.665455
S4	0.844062	0.501663	0.357724	0.333333
S5	1	1	1	0.485411
S6	0.333333	0.603932	0.333333	0.424594
S7	0.503788	0.333333	0.431373	0.362376
S8	0.49574	0.572661	0.427184	0.515493
S9	0.851784	0.692115	0.444444	0.418764

The grey relational grade γ_i in the table 5.3 has computed by using eq. (2.7) in the post-averaging stage of the grey relation coefficients.

Table 5.3 The GRG and rank based on Taguchi L$_9$ Orthogonal Array Design of experiment

Sl. No.	Grey Relational Grade	Rank
S1	0.696305	2
S2	0.502215	7
S3	0.574122	4
S4	0.509195	5
S5	0.871353	1
S6	0.423798	8
S7	0.407717	9
S8	0.50277	6
S9	0.601777	3
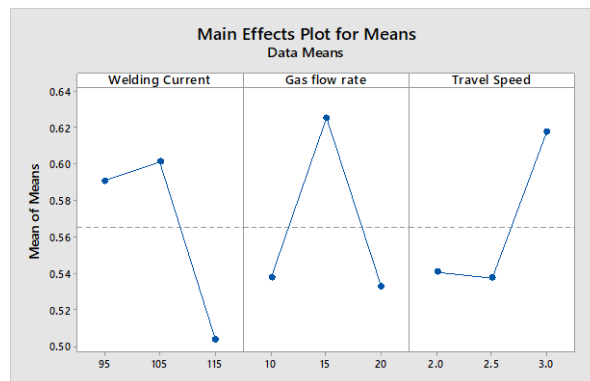
Figure 5.1 Mean Effect Plot for GRG
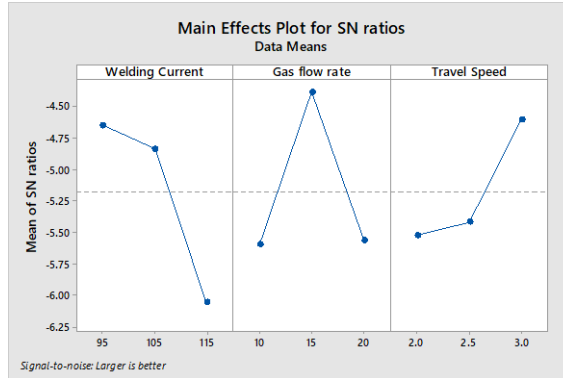
Figure 5.2 S/N ratio Plot for GRG

Using S/N ratio plots, the most effective combination of parameters has been determined. The suggested factor settings are as follows: welding current set to 95 A, gas flow rate set to 15 l/min, and travel speed set to 3 mm/min.

Table 5.4 ANOVA for overall GRG

Source	DoF	Seq.-SS	Adj.-SS	Adj.-MS	F	P
Current (A)	2	0.022281	0.022281	0.011141	0.80	0.556
Gas flow rate (l/min)	2	0.000899	0.000899	0.000449	0.03	0.969
Travel speed (mm/min)	2	0.001803	0.001803	0.000902	0.06	0.939
Residual Error	2	0.027957	0.027957	0.013979		
Sum	8	0.052940				

The co-relation value R^2 and adjusted value R^2 is lying between 0 to 1. In this present work the value is found 0.85.

Pie - Chart diagram for percentage of contribution in GRA: Austenitic SS 304L are shown in figures 5.3.
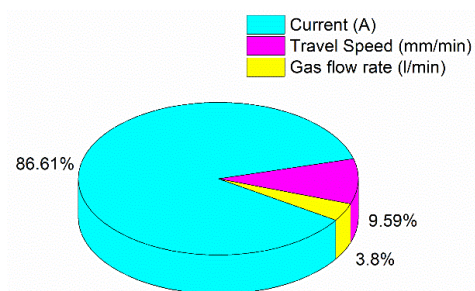
Figure 5.3 Pie Chart for Percentage of contribution

5.1.2 Results and Analyses of Austenitic SS 304L using TOPSIS Method

When there are multiple goals to achieve, we use TOPSIS, a type of multi-criteria decision-making (MCDM). The idea behind it is that the best solution is the one that is least like the ideal solution and most like the undesirable ideal solution. To normalize the choice matrix, use eq. (2.10).

Table 5.5 Normalization of the experimental data by TOPSIS method experiment

SL No.	UTS (MPa)	Elongation %	BW (mm)	DP (mm)
S1	0.331	0.332	0.433	0.284
S2	0.327	0.285	0.318	0.323
S3	0.326	0.339	0.340	0.294
S4	0.341	0.313	0.278	0.379
S5	0.343	0.422	0.376	0.265
S6	0.323	0.350	0.297	0.392
S7	0.333	0.202	0.303	0.348
S8	0.333	0.340	0.329	0.350
S9	0.341	0.373	0.297	0.344

A weight is assigned to each criterion that is considered during optimisation. Eq. (2.11) is used to include all input factors with equal weight percentages. Table 5.6 presents the weighted normalised value of the experimental data obtained by the TOPSIS technique.

Table 5.6 Weighted and normalized value of the experimental data by using TOPSIS

SL. No.	UTS (MPa)	% Elongation	BW (mm)	DP (mm)
S1	0.083	0.083	**0.108**	0.071
S2	0.082	0.071	0.080	0.081
S3	0.082	0.085	0.085	0.073
S4	0.085	0.078	*0.070*	0.095
S5	**0.086**	0.105	0.094	*0.066*
S6	*0.081*	0.087	0.074	**0.098**
S7	0.083	0.051	0.076	0.087
S8	0.083	0.085	0.082	0.087
S9	0.085	0.093	0.074	0.086

The positive ideal solution, also known as Zenith (A*), represents the best possible performance for each normalized criterion, with the uppermost value for each criterion. Conversely, the (-) ve ideal solution, sometimes called Nadir or anti-ideal (A-), represents the worst performance, with the lowermost value for each criterion. To find this solution, equations (2.12 and 2.13) are used, and table 5.7 provides the positive and negative ideal solutions for all output responses.

Table 5.7 Positive and negative ideal solutions for all output responses

UTS (MPa)	% Elongation	Bead width (mm)	Depth of penetration (mm)
0.086	0.105	0.070	0.098
0.081	0.051	0.108	0.066

The values for separation measure are tabulated shown in Table 5.8.

Table 5.8 Separation measure for the total experimental run

SL. No.	S^+	S^-
S1	0.035174	0.050848
S2	0.047974	0.027214
S3	0.039899	0.038097
S4	0.047509	0.039882
S5	0.034789	0.060232
S6	0.038768	0.048839
S7	0.06469	0.021955
S8	0.034732	0.042477
S9	0.03802	0.047475

The relation is used to determine the closeness values for a particular option, which are determined using equation (2.16). The following table presents the values and rankings for relative closeness. The experimental data has been weighted and normalised using the TOPSIS approach.

Table 5.9 Relative closeness value and rank

SL. No.	Relative closeness value	Rank
S1	0.591	6
S2	0.362	9
S3	0.488	7
S4	0.456	5
S5	0.634	4
S6	0.557	2
S7	0.253	3
S8	0.550	8
S9	0.555	1

Table 5.10 displays the response tables for the mean and S/N ratios in relation to the closeness value. From the mean effect plots in figures. 5.4 and 5.5 the main effect plots for S/N ratios identify the optimal factor setting as the most suitable parametric combination. The optimal factor setting is 105 A welding current, 20 l/min gas flow rate, and 2 mm/min travel speed. The current contributes 51 percent more than the gas flow rate and travel time. In TOPSIS figure 5.6, the percentage contribution of input parameters is displayed.

Table 5.10 Response Means closeness value

Level	Current(A)	Travel speed (mm/min)	Gas flow rate (l/min)
1	0.1863	0.2783	0.2693
2	0.3220	**0.3990**	0.2403
3	**0.4837**	0.3147	**0.4823**
Delta	0.2973	0.1207	0.2420
Rank	1	3	2
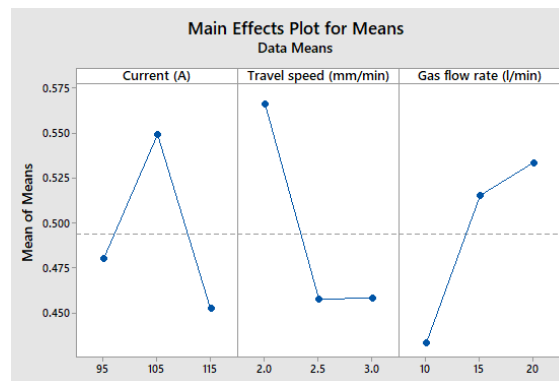
Figure 5.4 Main effects plot for means of closeness value
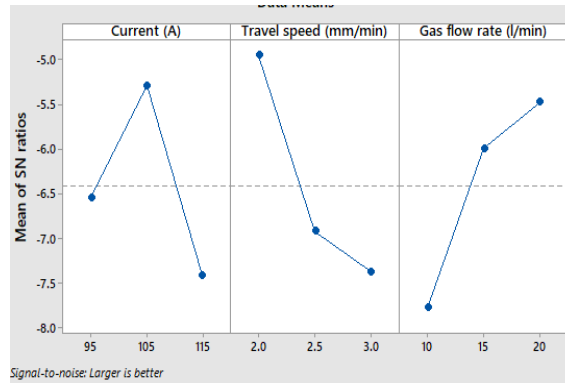
Figure 5.5 Main effect plot for S/N ratios for closeness value

Table 5.11 Response table for S/N ratio of closeness value

Source	DoF	Seq-SS	Adj-SS	Adj-MS	F	P
Current (A)	2	6.863	6.863	3.431	0.27	0.787
Gas flow rate (l/min)	2	8.733	8.733	4.367	0.34	0.744
Travel speed (mm/min)	2	9.992	9.992	4.996	0.39	0.717
Residual Error	2	25.329	25.329	12.664		
Sum	8	50.916				
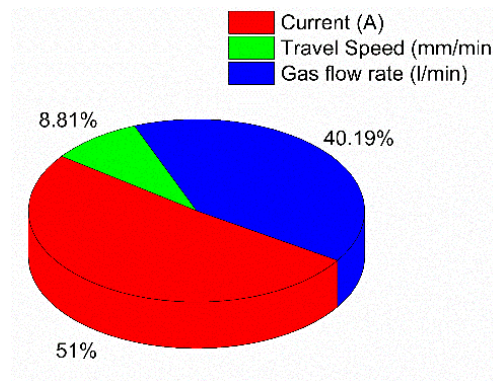
Figure 5.6 Percentage of contribution of input parameters in TOPSIS

5.2 Analysis of Results of Ferritic SS 409M

The results of TIG welding of Ferritic SS409M as per L_9 Taguchi orthogonal array design and TOPSIS design of experiment are analyzed, in the following sections.

5.2.1 Multi-Objective Optimization using Grey Based Taguchi Method

The experimental data from Table 4.5 is linearly normalized within the range of zero to one, this process also known as Gray relational generation. The normalization of the experimental data is determined by employing the eq. (2.2). which follows the larger-the-better principle. The process of normalizing experimental data is illustrated in Table 5.12

Table 5.12 Data normalization using Taguchi L$_9$ Orthogonal Array design of experiment

Sl. No	UTS (MPa)	Elongation %	Bead Width (mm)	Depth of penetration (mm)
S1B	0	0.4296875	0.653523	0.687976
S2B	0.72741	0	1	1
S3B	0.084337	0.4609375	0.770134	0.435312
S4B	0.045181	0.765625	0.098154	0.439878
S5B	0.277108	0.2421875	0.579698	0.783866
S6B	0.131024	1	0	0.669711
S7B	0.995482	0.3125	0.450503	0.121766
S8B	0.875	0.28125	0.391779	0
S9B	1	0.5703125	0.135067	0.69102

Table 5.13 displays the Grey Relation Coefficients. The coefficients of grey relations for 304L: Equation (2.6) is used to compute the L$_9$ Taguchi orthogonal array design of experiments.

Table 5.13 Experimental design based on Grey relational coefficient and the Taguchi L$_9$ Orthogonal Array

Sl. No	UTS (MPa)	Elongation %	Bead Width (mm)	Depth of penetration (mm)
S1B	0.333333	0.467153285	0.590684	0.615745
S2B	0.647173	0.333333333	1	1
S3B	0.353191	0.481203008	0.685057	0.469621
S4B	0.343685	0.680851064	0.356673	0.471644
S5B	0.408867	0.397515528	0.5433	0.698193
S6B	0.365237	1	0.333333	0.6022
S7B	0.991045	0.421052632	0.476419	0.362783
S8B	0.8	0.41025641	0.451173	0.333333
S9B	1	0.537815126	0.366318	0.618062

The average result of the grey relation coefficients including its relational grade γ_i has computed by using equation (2.7) which is presented in Table 5.14.

Table 5.14 The GRG and rank based on Taguchi L$_9$ orthogonal array design of experiment

SL. No.	Grey Relational Grade	Rank
S1B	0.501728886	6
S2B	0.745126706	1
S3B	0.497268282	8
S4B	0.463213237	9
S5B	0.511968961	5
S6B	0.575192418	3
S7B	0.562824816	4
S8B	0.498690774	7
S9B	0.630548898	2
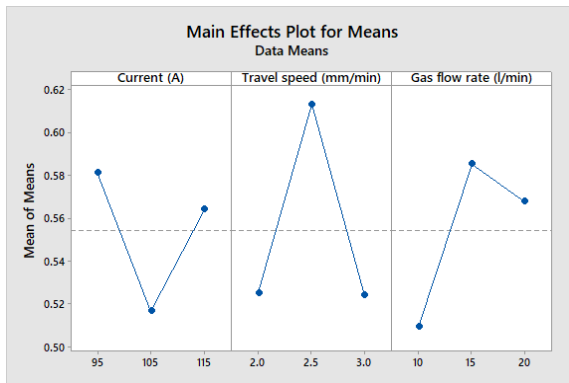
Figure 5.7 Mean Effect Plot for GRG   Figure 5.8 S/N ratio Plot for GRG
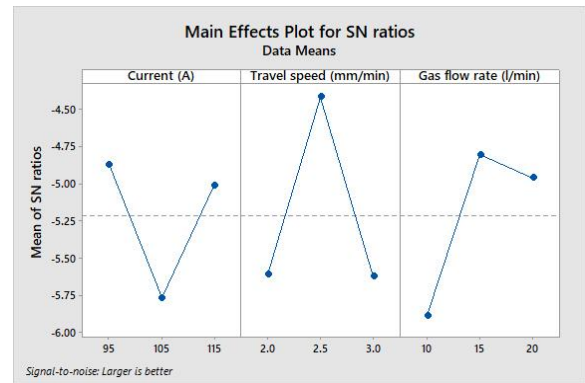
From the S/N ratio plots optimum parametric combination has been determined. The optimal factor setting becomes welding current 95 A, Gas flow rate 15l/min and Travel speed 2.5 mm/min.

Table 5.15 ANOVA for overall GRG

Source	DoF	Seq.-SS	Adj.-SS	Adj.-MS	F	P
Current (A)	2	0.006703	0.006703	0.003351	0.22	0.818
Gas flow rate (l/min)	2	0.009499	0.009499	0.004749	0.32	0.760
Travel speed (mm/min)	2	0.015614	0.015614	0.007807	0.52	0.659
Residual Error	2	0.030120	0.030120	0.015060		
Sum	8	0.061935				

Pie - Chart diagram of Percentage of contribution in GRA: 409M Ferritic stainless steel are shown in figures 5.9.
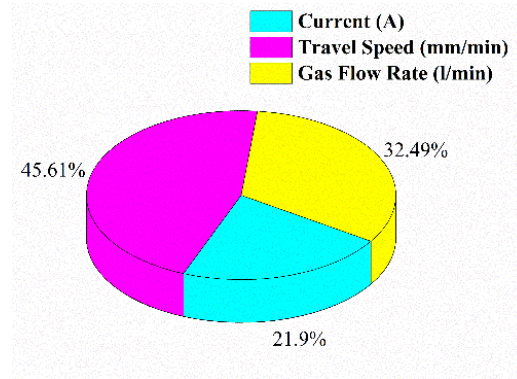
Figure 5.9 Pie Chart for Percentage of contribution

5.2.2 Results and Analyses of Ferritic SS 409M using TOPSIS Method

TOPSIS is a multi-criteria decision-making (MCDM) approach for addressing situations with many goals. It is founded on the assumption that the best response is the one that differs the most from the perfect solution while also being the closest to the undesirable ideal alternative. Normalising the decision matrix through equation (2.15).

Table 5.16 Normalization of the experimental data by TOPSIS method experiment

SL. No.	UTS (MPa)	% Elongation	BW (mm)	DP (mm)
S1B	0.311	0.324	0.349	0.345
S2B	0.346	0.237	0.378	0.370
S3B	0.315	0.330	0.359	0.324
S4B	0.313	0.392	0.303	0.325
S5B	0.324	0.286	0.343	0.352
S6B	0.317	0.440	0.294	0.343
S7B	0.358	0.300	0.332	0.299
S8B	0.353	0.294	0.327	0.289
S9B	0.359	0.353	0.306	0.345

A weight is assigned to each criterion that is considered during optimization. Equation (2.16) is employed to account for all input factors with equal weight percentages. Table 5.6 illustrates the weighted normalized value of the experimental data obtained through the TOPSIS approach.

Table 5.17 Weighted normalized value of the experimental data by TOPSIS method

SL. No.	UTS (MPa)	% Elongation	BW (mm)	DP (mm)
S1B	*0.078*	0.081	0.087	0.086
S2B	0.086	0.059	**0.095**	**0.092**
S3B	0.079	0.083	0.090	0.081
S4B	*0.078*	0.098	0.076	0.081
S5B	0.081	0.071	0.086	0.088
S6B	0.079	0.110	*0.074*	0.086
S7B	**0.090**	0.075	0.083	0.075
S8B	0.088	0.073	0.082	*0.072*
S9B	**0.090**	0.088	0.076	0.086

Zenith (A*), also known as the (+ve) positive ideal solution, is the optimal performance for each normalized criterion, with the highest value for each criterion. Conversely, the (-ve) negative ideal solution, which is occasionally referred to as the Nadir or anti-ideal (A-), is the worst possible solution, as it has the lowest value for each criterion. Equations (2.17 and 2.18) are employed to determine this solution, and table 5.7 contains the (+ve) and (-ve) ideal solutions for all output responses.

Table 5.18 Positive and negative ideal solutions for all output responses

UTS	% of elongation	Bead Width	Depth of Penetration
0.090	0.110	0.074	0.092
0.078	0.059	0.095	0.072

The values for separation measure are tabulated shown in table 5.19.

Table 5.19   Separation measure for the total experimental run

Sample no.	S+	S-
S1B	0.032779	0.029248
S2B	0.050926	0.030298
S3B	0.031968	0.029774
S4B	0.02748	0.039959
S5B	0.04067	0.023624
S6B	0.024293	0.052598
S7B	0.040803	0.022097
S8B	0.043622	0.019509
S9B	0.029044	0.0344

The relation is used to find the relative closeness values for a specific alternative are calculated using the eq. (2.21). Below the table visualized the relative closeness value and rank.

Table 5.20 Relative closeness value and rank

SL. No.	Relative closeness value	Rank
S1B	0.472	6
S2B	0.373	9
S3B	0.482	7
S4B	0.593	5
S5B	0.367	4
S6B	0.684	2
S7B	0.351	3
S8B	0.309	8
S9B	0.542	1

Tables 5.10 display the response table containing the mean and S/N ratios for the closeness value. figures 5.10 and 5.11 display the mean effect plots. The main effect plots for S/N ratios identify the optimal factor setting as the optimum parametric combination. The optimal factor setting is 105 A welding current, 20 l/min gas flow rate, and 2 mm/min travel speed.

The current contributes 51 percent more than the gas flow rate and travel speed. Fig. 5.6 displays the percentage contribution of input parameters in TOPSIS.

Table 5.21 Response Means closeness value

| Level	Current(A)	Travel speed (mm/min)	"Gas flow rate (l/min)"
01	0.4423	0.4883	0.4720
02	0.5480	0.5027	0.3497
03	0.4007	0.4000	0.5693
Delta	0.1473	0.1027	0.2197
Rank	2	3	1
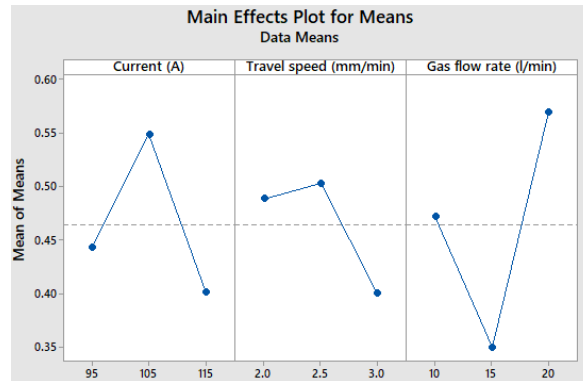
Figure 5.10 Main effects plot for means of closeness value
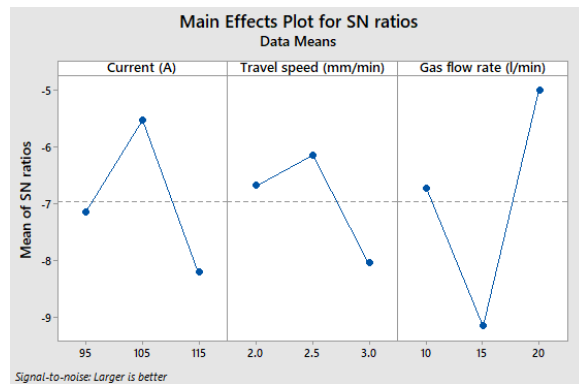
Figure 5.11 Main effect plot for S/N ratios for closeness value

Table 5.22 Response table for S/N ratio of closeness value

Source	DoF	Seq-SS	Ad-SS	Adj-MS	F	P
Current (A)	2	0.034609	0.034609	0.017304	237.05	0.004
Gas flow rate (l/min)	2	0.072693	0.072693	0.036346	497.89	0.002
Travel speed (mm/min)	2	0.018549	0.018549	0.009274	127.05	0.008
Residual Error	2	0.000146	0.000146	0.000073		
Sum	8	0.125996				
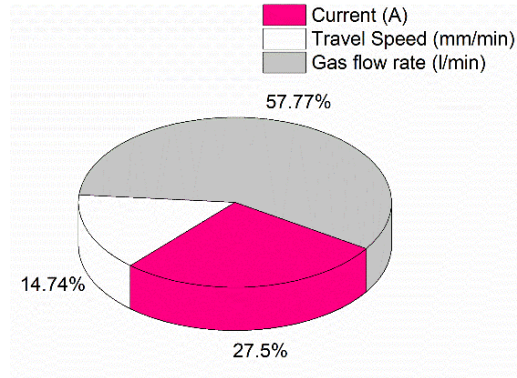
Figure 5.12 Percentage of contribution of input parameters in TOPSIS

5.3 Experimental Investigation of Austenitic SS 304L and Ferritic SS 409M

In the following paragraphs the results of dissimilar TIG welding of Austenitic SS 304L and Ferritic SS 409M are analysed in different technique.

5.3.1 Analyses of Results as per Taguchi L$_9$Orthogonal Array

The experimental data from Table 4.8 is linearly normalized within the range of zero to one. The normalization of the experimental data is determined by employing the eq. (2.2). which follows the larger-the-better principle. The process of normalizing experimental data is illustrated in Table 5.23

Table 5.23   Data normalization using Taguchi L$_9$ orthogonal array experimental design of dissimilar welding on Austenitic SS 304L to Ferritic SS 409M

Sl. No.	UTS (MPa)	Elongation %	Bead Width (mm)	Depth of penetration (mm)
S1A	0.02455	0.089115423	0.542857	0.648221
S2A	0	0.035185794	0	0.541502
S3A	0.16653	0.056231503	0.615385	0.467721
S4A	0.115957	0	1	0.722003
S5A	0.612193	0.269976981	0.762637	1
S6A	1	0.426504439	0.068681	0.955204
S7A	0.553764	0.503452812	0.26978	0
S8A	0.165876	0.089115423	0.445604	0.413702
S9A	0.904992	1	0.289011	0.156785

113

Refer to Table 5.24 for the Grey Relation Coefficients. The following are the grey relation coefficients for welding ferritic stainless steel 409M to austenitic stainless steel 304L: Equation (2.6) is used to determine the Taguchi L$_9$ orthogonal array design of this experiment.

Table 5.24 Experimental design based on Grey Relational Coefficient and Taguchi L$_9$ orthogonal array design of experiment

Sl. No.	UTS (MPa)	Elongation %	BW (mm)	DP (mm)
S1A	0.33888	0.354387601	0.522388	0.587007
S2A	0.333333	0.341340218	0.333333	0.521649
S3A	0.374962	0.346315909	0.565217	0.484365
S4A	0.361261	0.333333333	1	0.642676
S5A	0.563186	0.406496458	0.678092	1
S6A	1	0.465768112	0.349328	0.917775
S7A	0.52841	0.501732387	0.406431	0.333333
S8A	0.374778	0.354387601	0.474205	0.460279
S9A	0.840325	1	0.412886	0.372241

The grey relational grades γi is depicted in Table 5.25**.** The mean of the grey relation coefficients (grade γ$_i$) has computed by applying the equation (2.7)

Table 5.25 GRG and rank based on L$_9$ Taguchi orthogonal array design of experiment

Sl. No.	Grey Relational Grade	Rank
S1A	0.450665566	5
S2A	0.382414092	9
S3A	0.442714994	6
S4A	0.5843174	4
S5A	0.661943601	2
S6A	0.683217854	1
S7A	0.442476686	7
S8A	0.41591238	8
S9A	0.656362884	3
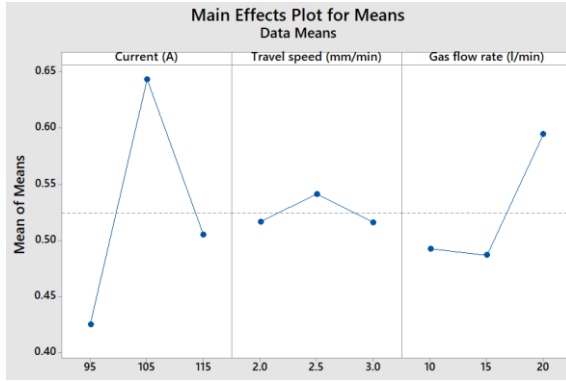
Figure 5.13 Mean Effect Plot for GRG   Figure 5.14 S/N ratio Plot for GRG
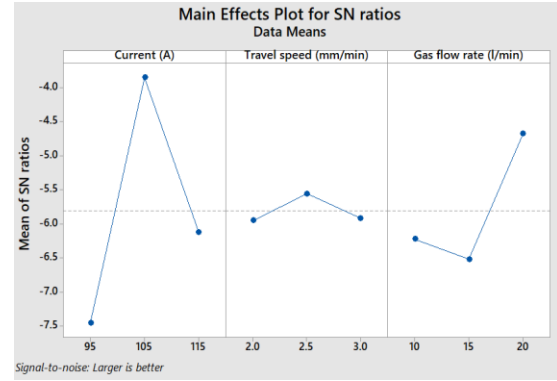
With the help of S/N ratio plots, optimum parametric combination has been determined. The optimal factor setting becomes welding current = 105 A, Gas flow rate = 20 *l*/min and Travel speed =2.5 mm/min.

Table 5.26 ANOVA for overall GRG

Source	DoF	Seq.-SS	Adj.-SS	Adj.-MS	F	P
Current (A)	2	0.072934	0.072934	0.036467	3.68	0.214
Gas flow rate (l/min)	2	0.021880	0.021880	0.010940	1.10	0.476
Travel speed (mm/min)	2	0.001239	0.001239	0.000619	0.06	0.941
Residual Error	2	0.019843	0.019843	0.009922		
Sum	8	0.115896				

Pie - Chart diagram of Percentage of contribution in GRA: Dissimilar welding on Austenitic SS 304L to Ferritic SS 409M are shown in figures 5.15.

Figure 5.15 Pie Chart of Percentage of contribution of all input parameters

5.3.2 Analyses of Results as per TOPSIS Method

TOPSIS is a type of multi-criteria decision-making (MCDM) that is used when there is more than one goal to achieve. The idea behind it is that the best solution should be the one that is the furthest from the ideal solution and the closest to the unwanted ideal solution. Making the choice matrix more uniform by using equation (2.15).

Table 5.27 Normalization of the experimental data by TOPSIS method experiment

Sl. No.	UTS (MPa)	Elongation %	BW (mm)	DP (mm)
S1A	0.306	0.246	0.342	0.342
S2A	0.304	0.226	0.285	0.331
S3A	0.316	0.234	0.350	0.329
S4A	0.313	0.213	0.390	0.349
S5A	0.348	0.312	0.366	0.378
S6A	0.375	0.369	0.292	0.373
S7A	0.344	0.398	0.313	0.275
S8A	0.316	0.246	0.332	0.318
S9A	0.369	0.580	0.315	0.292

Each of the criteria that are used for optimisation is given a weight. Equation (2.16), which gives each input factor an equal weight percentage, is used to account for them all. Table 5.28 displays the normalised weighted value of the trial data from the TOPSIS method.

Table 5.28 Weighted normalized value of the experimental data by TOPSIS

Sl. No.	UTS (MPa)	Elongation %	BW (mm)	DP (mm)
S1A	0.077	0.061	0.086	0.085
S2A	0.076	0.057	0.071	0.083
S3A	0.079	0.058	0.087	0.082
S4A	0.078	0.053	0.098	0.087
S5A	0.087	0.078	0.091	0.094
S6A	0.094	0.092	0.073	0.093
S7A	0.086	0.099	0.078	0.069
S8A	0.079	0.061	0.083	0.079
S9A	0.092	0.145	0.079	0.073

The Zenith (A*), sometimes referred to as the positive ideal solution, is the best possible performance for each normalised criteria, achieving the maximum value for each criterion. On the other hand, the negative ideal solution, also known as the Nadir or anti-ideal (A-), is the most unfavourable solution since it has the lowest value for every criterion. The solution is determined using equations 2.17 and 2.18. Table 5.7 provides the positive and negative ideal solutions for all output responses.

Table 5.29 Positive and negative ideal solutions for all output responses.

UTS	% of elongation	BW (mm)	DP (mm)
0.094	0.145	0.071	0.094
0.076	0.053	0.098	0.069

The values for separation measure are tabulated shown in Table 5.30.

Table 5.30 Separation measure for the total experimental run

Sl. No.	S^+	S^-
S1A	0.086533	0.023382
S2A	0.094637	0.014211
S3A	0.089139	0.021821
S4A	0.093222	0.032168
S5A	0.067512	0.042297
S6A	0.057961	0.049425
S7A	0.056144	0.047697
S8A	0.087284	0.018043
S9A	0.028544	0.093413

The relation is used to determine the estimated values of closeness for a particular alternative, using equation (2.21). The table below displays the values and ranks of relative closeness.

Table 5.31 Relative closeness value and rank

Sl. No.	Relative closeness	Rank
S1A	0.213	6
S2A	0.131	9
S3A	0.197	7
S4A	0.257	5
S5A	0.385	4
S6A	0.460	2
S7A	0.459	3
S8A	0.171	8
S9A	0.766	1

Tables 5.32 display the mean and S/N ratios for the closeness value in the response table. From the mean effect plots in figure 5.16 and 5.17 main effect diagrams are used to determine the optimal factor setting for S/N ratios, which is the most effective parametric combination. The ideal factor setting is as follows: welding current = 115 A, gas flow rate = 20 l/min, and travel speed = 2.5 mm/min. The current contributes 53 percent more than the gas flow rate and travel speed. Figure. 5.18 illustrates the input parameters' percentage contribution to TOPSIS.

Table 5.32 Response Means closeness value

Level	Current (A)	Travel speed (mm/min)	Gas flow rate (l/min)
1	0.1803	0.2813	0.3097
2	0.3673	0.3847	0.2290
3	0.4653	0.3470	0.4743
Delta	0.2850	0.1033	0.2453
Rank	1	3	2
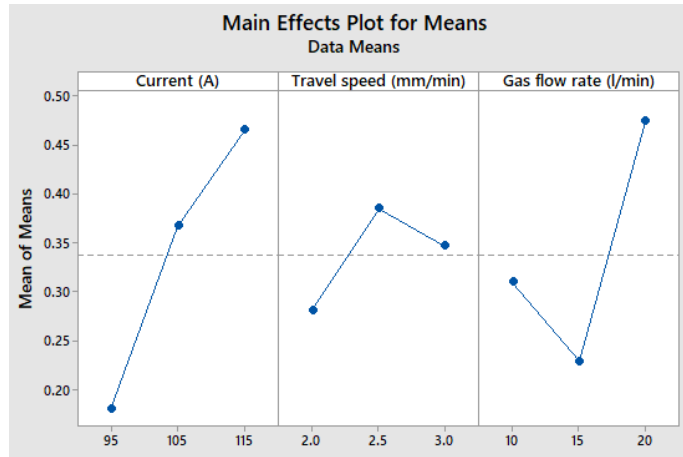
Figure 5.16 Main effects plot for means of closeness value
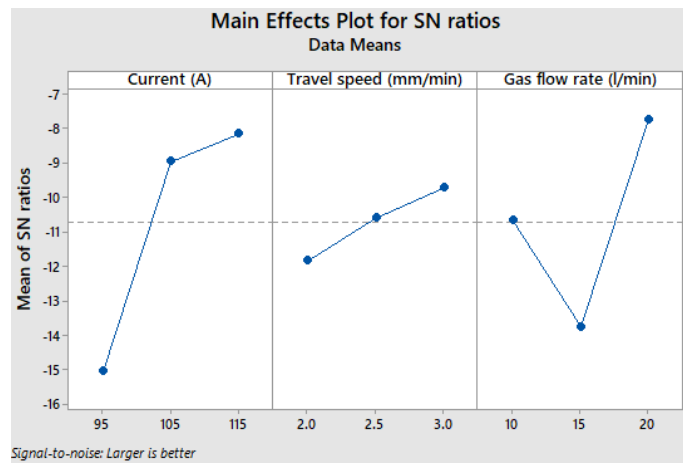
Figure 5.17 Main effects plot for S/N ratio closeness value

Table 5.33 Response table for S/N ratio of closeness value

Source	DoF	Seq.-SS	Adj.-SS	Adj.-MS	F	P
Current (A)	2	0.13295	0.13295	0.06647	0.94	0.517
Gas flow rate (l/min)	2	0.10477	0.10477	0.05239	0.74	0.576
Travel speed (mm/min)	2	0.02299	0.02299	0.01150	0.16	0.861
Residual Error	2	0.14212	0.14212	0.07106		
Sum	8	0.40284				

Pie - Chart diagram of Percentage of contribution in TOPSIS: Dissimilar welding on Austenitic SS304L to Ferritic SS 409M are shown in figures 5.15.
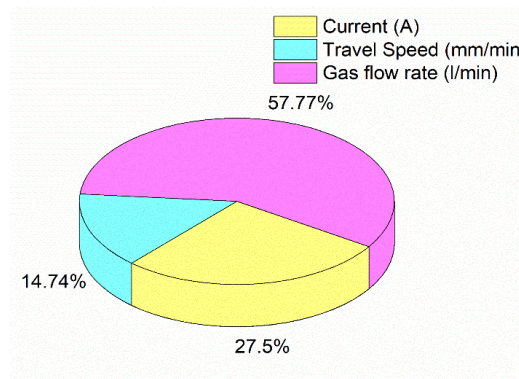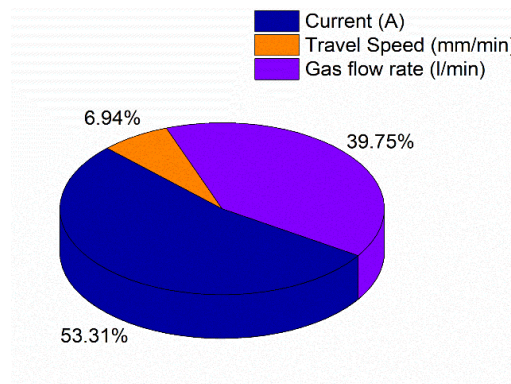

Figure 5.18 Percentage of contribution of input parameters in TOPSIS

6.1 Conclusions

The present experimental investigations of TIG welding process have been categorized as- i) similar material welding of Austenitic SS 304L ii) similar material welding of Ferritic SS 409M and iii) dissimilar material welding between Ferritic SS 409M and Austenitic SS 304L. In this work, three crucial process parameters have been chosen as welding current, gas flow rate, and travel speed. On the other hand, five important aspects such as UTS, % of elongation, bead width, penetration depth and micro hardness have been selected as responses parameters. Concluding remarks are summarised as follows based on the experimental outcomes and observations -

6.1.1 Conclusions drawn from ASS 304L welded material:

- ✓ It has been found from the visual inspection and X-ray radiography that most of the welding samples are defect free in optimal welding condition. Some minor porosity, lack of fusion, and undercuts are observed in the welding zone when process is carried out at aggressive parameter settings.
- ✓ The tensile test showed the satisfactory results (i.e. within the prescribed range 612.9 MPa – 650.14 MPa) for this material whereas input factors have some influence on the material's mechanical properties.
- ✓ The maximum hardness is observed in the welded zone followed by HAZ and parent metal. In this case the maximum hardness in the weld zone is obtained as 423 whereas in the HAZ and base metal are as 325 and 295.
- ✓ The base metal's microstructure displays a pure Austenitic structure with a significant amount of Austenitic twin. It is impossible to discern any significant differences between the HAZ microstructure and that of the base metal. On the other hand, HAZ exhibits an increase in grain growth. Another characteristic of HAZ is the presence of an Austenitic twin phase, while the grain of weld metal is equiaxed. Some samples also exhibit columnar dendritic development.
- ✓ The optimal parametric combination (C2: welding current 95 A, G2: gas flow rate 15 l/min, and T3: travel speed 3 mm/min) from GRA yields the best possible results.

✓ The recommended parametric configuration using TOPSIS analysis are as C2: welding current of 105 A, G1: gas flow rate of 20 l/min, and T3: travel speed of 2 mm/min.

6.1.2 Conclusions drawn from FSS409M welded material:

✓ It is discovered from the visual inspection and X-ray radiography that most of the welding samples are defect free in optimal welding condition. Some minor porosity, lack of fusion, and undercuts are observed in the welding zone when process is carried out at aggressive parameter settings.

✓ Best UTS result (498.9 MPa) is found from the sample S9B with an % of elongation of 22.2%. On the other hand, sample S1B gives the worst tensile strength 432.5 MPa with a percentage elongation of 20.4.

✓ The testing results showed that gas flow rate and travel speed have greater impact rather than the current. The Grey based Taguchi results revealed that C1G1T1, with a current of 95 A, a gas flow of 10 l/min, and a travel speed of 2 mm/s, is the optimal parameter combination.

✓ The TOPSIS optimisation technique identified the optimal parameter combination in C2, G3, and T2, with a current of 105 A, a gas flow rate of 20 l/min, and a travel speed of 2.5 mm/s.

✓ Base material shows typically Ferritic matrix which is usual for Ferritic stainless steel in general, Austenitic grains are found to be coarser in HAZ than in base metal. This may be attributed to lower cooling rate in the HAZ region. In some of the portion's, precipitated carbide has been found. Dispersed carbide phases are found in HAZ region.

6.1.3 Conclusions drawn from dissimilar welded material:

✓ Visual inspection and X-ray radiography tests reveal some of the defects in several samples while certain conditions also yield defect-free joints.

✓ The tensile tests give the satisfactory results. The UTS of the welded zone is 644.53 MPa for Austenitic stainless-steel SS 304L and SS 409 Ferritic material combination.

- ✓ Trends in hardness plots are similar, irrespective of parametric combinations.
- ✓ The ferrite matrix comprises austenite at the grain boundaries. The weld metal's microstructure comprises austenite and ferrite. The dominant austenitic grains are easily visible.
- ✓ The GRA optimal parameter settings are C2: current 105A G3: gas flow rate 20 l/min and T2: travel speed = 2.5 mm/s.
- ✓ The TOPSIS optimization technique identified the best influencing factor. The optimal parameter setting obtained from the analysis is as C3: current 115A, G3: gas flow rate 20 l/min, and T2: travel speed 2.5 mm/s.

6.2 Limitation for the present dissertation and scope for future research work

Limitation of the present work are mentioning below.

1. Aspects of weld defect/ porosity have not been estimated quantitively.
2. The obtain ultimate tensile strength was based on engineering stress vs strain diagram. By exploring true stress vs strain diagram, a more accurate data can be obtained.
3. The following mechanical properties (UTM and micro hardness) have been considered in the present work. Other than tensile properties, creep and fatigue properties of the weldment may be studied.
4. The percentage of various phases present with in the microstructure and their individual contribution to the weld mechanical properties have not been studied in the present work.

The work can be extended in the following directions.

1. Weld porosity can be examined through CT scan for accurate measurement of percentage of porosity.
2. Apart from statics mechanical properties, dynamic properties of the weldment may be studied in future.
3. Aspects of simulation- modelling of the welding phenomena can be attempted in future.

4. Instead of micro- indentation hardness, accurate and reliable hardness data can be obtained through nano- indentation harness test.

5. Tensile properties of the weldment may be studied at elevated temperature.

6. Corrosion and wear properties of the fabricated weldment appears to be the important aspects which required in-depth investigation.

7. In the context of industries 4.0, the experimental data carried out in the present welding research can be utilised to support intelligent manufacturing and to setup smart factories. The quantitative experimental data of the present work may also be utilised for virtual welding of similar and dissimilar materials.

[1] Parmar, R. S. (1997), Welding Processes and Technology, Khanna Publications.

[2] (N.d.-b). Iran-mavad.com. Retrieved May 31, 2024

[3] (N.d.-c). Aws.org. Retrieved May 31, 2024

[4] (N.d.). Org.Sy. Retrieved May 31, 2024

[5] Ardika, R. D., Triyono, T., & Muhayat, N. (2021). A review porosity in aluminum welding. Procedia Structural Integrity, 33, 171-180.

[6] Bhavsar, A. N., & Patel, V. A. (2016). Influence of process parameters of TIG welding process on mechanical properties of SS304L welded joint. International Research Journal of Engineering and Technology (IRJET), 3(5), 977-981.

[7] Weman, K. (2012). TIG welding. In Welding Processes Handbook, 63–69. Elsevier.

[8] welding Principle, T. I. G. TIG welding–Method and Application.

[9] Ramkumar, K. D., Chandrasekhar, A., Singh, A. K., Ahuja, S., Agarwal, A., Arivazhagan, N., & Rabel, A. M. (2015). Comparative studies on the weldability, microstructure, and tensile properties of autogenous TIG welded AISI 430 ferritic stainless steel with and without flux. Journal of Manufacturing Processes, 20, 54-69.

[10] Vidyarthy, R. S., Dwivedi, D. K., & Vasudevan, M. (2017). Influence of M-TIG and A-TIG welding process on microstructure and mechanical behaviour of 409 ferritic stainless steel. Journal of Materials Engineering and Performance, 26(3), 1391–1403.

[11] Anttila, S., Karjalainen, P., & Lantto, S. (2013). Mechanical properties of ferritic stainless-steel welds in using type 409 and 430 filler metals. Welding in the World, 57, 335-347.

[12] Vidyarthy, R. S., & Dwivedi, D. K. (2017). Analysis of the corrosion behavior of an A-TIG welded SS 409 weld fusion zone. Journal of Materials Engineering and Performance, 26, 5375-5384.

[13] Vidyarthy, R. S., & Dwivedi, D. K. (2019). Weldability evaluation of 409 FSS with A-TIG welding process. Materials Today: Proceedings, 18, 3052-3060.

[14] Ambade, S., Kataria, R., Tembhurkar, C., & Meshram, D. (2023). Experimental and finite element analysis of temperature distribution in 409 M ferritic stainless steel by

TIG, MIG and SMAW welding processes. Advances in Materials and Processing Technologies, 9(3), 843-858.

[15] Lakshminarayanan, A. K., Shanmugam, K., & Balasubramanian, V. (2009). Effect of welding processes on tensile and impact properties, hardness, and microstructure of AISI 409M ferritic stainless joints fabricated by duplex stainless steel filler metal. Journal of iron and steel research, international, 16(5), 66-72.

[16] Gupta, S. K., Raja, A. R., Vashista, M., & Yusufzai, M. Z. K. (2018). Effect of heat input on microstructure and mechanical properties in gas metal arc welding of ferritic stainless steel. Materials Research Express, 6(3), 036516.

[17] Köse, C., & Topal, C. (2019). Effect of post weld heat treatment and heat input on the microstructure and mechanical properties of plasma arc welded AISI 410S ferritic stainless steel. Materials Research Express, 6(6), 066517.

[18] Amuda, M. O. H., & Mridha, S. (2011). Effect of energy input on microstructure and hardness of TIG welded AISI 430-ferritic stainless steel. Advanced Materials Research, 264, 390-396.

[19] Vidyarthy, R. S., & Dwivedi, D. K. (2017). Analysis of the corrosion behaviour of an A-TIG welded SS 409 weld fusion zone. Journal of Materials Engineering and Performance, 26, 5375-5384.

[20] Mousazadeh, M. A., & Derakhshandeh-Haghighi, R. (2020). Autogenous tungsten inert gas welding of 430 ferritic stainless steel: the effect of inter-pass temperature on microstructure evolution and mechanical properties. Journal of Materials Engineering and Performance, 29, 7807-7820.

[21] Lakshminarayanan, A. K., Balasubramanian, V., & Madhusudhan Reddy, G. (2011). Microstructure and mechanical properties of electron beam-welded AISI 409M-grade ferritic stainless steel. The International Journal of Advanced Manufacturing Technology, 55, 153-162.

[22] Akita, M., Uematsu, Y., Kakiuchi, T., Nakajima, M., Agata, Y., & Takino, K. (2018). Joint microstructures, mechanical properties, and fatigue behaviour of ferritic stainless-steel SUS 430 welds with different filler metals. Welding International, 32(6), 427-435.

[23] Mohandas, T., Reddy, G. M., & Naveed, M. (1999). A comparative evaluation of gas tungsten and shielded metal arc welds of a "ferritic" stainless steel. Journal of materials processing technology, 94(2-3), 133-140.

[24] Lakshminarayanan, A. K., & Balasubramanian, V. (2010). An assessment of microstructure, hardness, tensile and impact strength of friction stir welded ferritic stainless-steel joints. Materials & Design, 31(10), 4592-4600.

[25] Lakshminarayanan, A. K., & Balasubramanian, V. (2013). Process parameters optimisation for friction stir welding of AISI 409M grade ferritic stainless steel. Experimental Techniques, 37, 59-73.

[26] Dinaharan, I., Muthu Krishnan, T., & Palanivel, R. (2022). An assessment of microstructure and tensile behaviour of magnetically impelled arc butt welded AISI 409 ferritic stainless-steel tubes. Journal of Materials Engineering and Performance, 31(10), 7808-7819.

[27] Delgado, A. J., Ambriz, R. R., Cuenca-Álvarez, R., Alatorre, N., & López, F. F. (2016). Heat input effect on the microstructural transformation and mechanical properties in GTAW welds of a 409L ferritic stainless steel. Revista de Metalurgia, 52(2), 68-77.

[28] Zaman, S., Khattak, M. A., & Tamin, M. N. (2018). Effects of welding on the microstructural properties of AISI 430 ferritic stainless steel. Journal of Advanced Research in Materials Science, 44(1), 25-32.

[29] Delgado, A. J., Ambriz, R. R., Cuenca-Álvarez, R., Alatorre, N., & López, F. F. (2016). Heat input effect on the microstructural transformation and mechanical properties in GTAW welds of a 409L ferritic stainless steel. Revista de Metalurgia, 52(2), 68-77.

[30] Ghosh, N., Kumar, P., & Nandi, G. (2016). Parametric optimization of gas metal arc welding process by using grey based taguchi method on AISI 409 ferritic stainless steel. Technological Engineering, 13(1), 6-11.

[31] Benlamnouar, M. F., Bensaid, N., Azzoug, M. O., Saadi, T., Zidani, M., & Badji, R. (2024). Optimization and Evaluation of Mechanical and Electrochemical Properties of Ferritic Stainless Steel Welding Using Taguchi Design. Key Engineering Materials, 973, 61-72.

[32] Lakshminarayanan, A. K., Shanmugam, K., & Balasubramanian, V. (2009). Effect of autogenous arc welding processes on tensile and impact properties of ferritic stainless-steel joints. Journal of iron and steel research, international, 16(1), 62-16.

[33] Raveendra, A., & Kumar, B. R. (2013). Experimental study on pulsed and non-pulsed current TIG welding of stainless-steel sheet (SS304). International Journal of Innovative Research in Science, Engineering and Technology, 2(6), 2337-2344.

[34] Ghosh, N., Pal, P. K., & Nandi, G. (2018). Investigation on dissimilar welding of AISI 409 ferritic stainless steel to AISI 316L austenitic stainless steel by using grey based Taguchi method. Advances in Materials and Processing Technologies, 4(3), 385-401.

[35] Lothongkum, G., Viyanit, E., & Bhandhubanyong, P. (2001). Study on the effects of pulsed TIG welding parameters on delta-ferrite content, shape factor and bead quality in orbital welding of AISI 316L stainless steel plate. Journal of Materials Processing Technology, 110(2), 233-238.

[36] Pasupulla, A. P., Agisho, H. A., Seetharaman, S., & Vijayakumar, S. (2022). Characterization and analysis of TIG welded stainless steel 304 alloy plates using radiography and destructive testing techniques. Materials Today: Proceedings, 51, 935-938.

[37] Yan, J., Gao, M., & Zeng, X. (2010). Study on microstructure and mechanical properties of 304 stainless steel joints by TIG, laser and laser-TIG hybrid welding. Optics and Lasers in Engineering, 48(4), 512-517.

[38] Durgutlu, A. (2004). Experimental investigation of the effect of hydrogen in argon as a shielding gas on TIG welding of austenitic stainless steel. Materials & design, 25(1), 19-23.

[39] Aslam, M., & Sahoo, C. K. (2022). Numerical and experimental investigation for the cladding of AISI 304 stainless steel on mild steel substrate using Gas Metal Arc Welding. CIRP Journal of Manufacturing Science and Technology, 37, 378-387.

[40] Kumar, S., & Shahi, A. S. (2011). Effect of heat input on the microstructure and mechanical properties of gas tungsten arc welded AISI 304 stainless steel joints. Materials & Design, 32(6), 3617-3623.

[41] Shanmugam, K., Lakshminarayanan, A. K., & Balasubramanian, V. (2009). Effect of weld metal properties on fatigue crack growth behaviour of gas tungsten arc welded

AISI 409M grade ferritic stainless-steel joints. International journal of pressure vessels and piping, 86(8), 517-524.

[42] Mahajan, A., Singh, H., Kumar, S., & Kumar, S. (2022). Mechanical properties assessment of TIG welded SS 304 joints. Materials Today: Proceedings, 56, 3073-3077.

[43] Zhou, J., Shen, J., Hu, S., Zhao, G., & Wang, Q. (2019). Microstructure and mechanical properties of AISI 430 ferritic stainless-steel joints fabricated by cold metal transfer welding. Materials Research Express, 6(11), 116536.

[44] Ghosh, N., Pal, P. K., Nandi, G., & Rudrapati, R. (2018). Parametric optimization of gas metal arc welding process by PCA based Taguchi method on austenitic stainless steel AISI 316L. Materials Today: Proceedings, 5(1), 1620-1625.

[45] Ghosh, N., Pal, P. K., & Nandi, G. (2016). Parametric optimization of MIG welding on 316L austenitic stainless steel by grey-based Taguchi method. Procedia Technology, 25, 1038-1048.

[46] Singh, N. K. (2017). Performance of activated TIG welding in 304 austenitic stainless-steel welds. Materials Today: Proceedings, 4(9), 9914-9918.

[47] Ghosh, N., Pal, P. K., Nandi, G., & Rudrapati, R. (2018). Parametric optimization of gas metal arc welding process by PCA based Taguchi method on austenitic stainless steel AISI 316L. Materials Today: Proceedings, 5(1), 1620-1625.

[48] Rajaravi, C., Ganesh, B., Lakshmanan, S., & Gobalakrishnan, B. (2023). Influence of TIG welding processing parameters on mechanical properties of austenitic stainless steel using Taguchi analysis. Materials Today: Proceedings, 72, 2402-2409.

[49] Khrais, S., Mohammed, A., Al, A. A., & Darabseh, T. (2024). Effect of TIG welding parameters on 316 L stainless steel joints using taguchi L27 approach. Materials Research Express, 11(1), 016512.

[50] Tesfaye, F. K., & Getaneh, A. M. (2024). The grey-based Taguchi method was used to enhance the TIG-MIG hybrid welding process parameters for mild steel. Invention Disclosure, 4, 100016.

[51] Neelamegam, C., Meenakshisundaram, R., & Muthukumaran, V. (2024). Process parameter optimization of hot-wire TIG welding of 10 mm thick type 316LN stainless

steel plates. Proceedings of the Institution of Mechanical Engineers, Part C: Journal of Mechanical Engineering Science, 238(3), 849-862.

[52] Linger, M. A., & Bogale, T. M. (2023). Parameters optimization of tungsten inert gas welding process on 304L stainless steel using grey based Taguchi method. Engineering Research Express, 5(1), 015013.

[53] Rajput, S. K., Kumar, A., Tripathi, S. S., & Sachan, E. (2020). Investigation of microstructural behavior and mechanical properties of dissimilar weld joints of austenitic-ferritic stainless steel. Materials Today: Proceedings, 25, 778-784.

[54] Ghosh, N., Pal, P. K., & Nandi, G. (2018). Investigation on dissimilar welding of AISI 409 ferritic stainless steel to AISI 316L austenitic stainless steel by using grey based Taguchi method. Advances in Materials and Processing Technologies, 4(3), 385-401.

[55] Mehmood, S., & Rahman, R. A. U. (2024). Investigating parametric effects during TIG welding of dissimilar metals. Mehran University Research Journal of Engineering & Technology, 43(1), 165-181.

[56] Chaudhari, V., Bodkhe, V., Deokate, S., Mali, B., & Mahale, R. (2019). Parametric optimization of TIG welding on SS 304 and MS using Taguchi approach. Int. Res. J. Eng. Technol, 6(5), 880-885.

[57] Vora, J. J., & Badheka, V. J. (2017). Experimental investigation on microstructure and mechanical properties of activated TIG welded reduced activation ferritic/martensitic steel joints. Journal of Manufacturing Processes, 25, 85-93.

[58] Sivaprasad, K., & Raman, S. G. S. (2007). Influence of magnetic arc oscillation and current pulsing on fatigue behavior of alloy 718 TIG weldments. Materials Science and Engineering: A, 448(1-2), 120-127.

[59] Kumar, H., Ahmad, G. N., & Singh, N. K. (2019). Activated flux TIG welding of Inconel 718 super alloy in presence of tri-component flux. Materials and Manufacturing Processes, 34(2), 216-223.

[60] Wang, Q., Sun, D. L., Na, Y., Zhou, Y., Han, X. L., & Wang, J. (2011). Effects of TIG welding parameters on morphology and mechanical properties of welded joint of Ni-base superalloy. Procedia Engineering, 10, 37-41.

[61] Ibrahim, I. A., Mohamat, S. A., Amir, A., & Ghalib, A. (2012). The Effect of Gas Metal Arc Welding (GMAW) processes on different welding parameters. Procedia Engineering, 41, 1502-1506.

[62] Karadeniz, E., Ozsarac, U., & Yildiz, C. (2007). The effect of process parameters on penetration in gas metal arc welding processes. Materials & design, 28(2), 649-656.

[63] Sharma, A., Verma, A., Vashisth, D., & Khanna, P. (2022). Prediction of bead geometry parameters in MIG welded aluminium alloy 8011 plates. Materials Today: Proceedings, 62, 2787-2793.

[64] Naik, A. B., & Reddy, A. C. (2018). Optimization of tensile strength in TIG welding using the Taguchi method and analysis of variance (ANOVA). Thermal Science and Engineering Progress, 8, 327-339.

[65] Tesfaye, F. K., & Getaneh, A. M. (2024). The grey-based Taguchi method was used to enhance the TIG-MIG hybrid welding process parameters for mild steel. Invention Disclosure, 4, 100016.

[66] Narang, H. K., Singh, U. P., Mahapatra, M. M., & Jha, P. K. (2011). Prediction of the weld pool geometry of TIG arc welding by using fuzzy logic controller. International Journal of Engineering, Science and Technology, 3(9), 77-85.

[67] Anand, K. R., & Mittal, V. (2017). Review on the parametric optimization of tig welding. Int. Res. J. Eng. Technol. (IRJET), 4(01), 2395-0056.

[68] Kim, I. S., Son, J. S., Park, C. E., Kim, I. J., & Kim, H. H. (2005). An investigation into an intelligent system for predicting bead geometry in GMA welding process. Journal of Materials Processing Technology, 159(1), 113-118.

[69] Narang, R., Maheshwari, V., & Khanna, P. (2021). Prediction of bead geometry parameters in MIG welded stainless steel 409L plates by mathematical modelling. Materials Today: Proceedings, 44, 900-908.

[70] Ghosh, N., Pal, P. K., & Nandi, G. (2016). Parametric optimization of MIG welding on 316L austenitic stainless steel by Taguchi method. Archives of Materials Science and Engineering, 79(1), 27-36.

[71] Kumar, S., Singh, P., Patel, D., & Prasad, S. B. (2017). Optimization of TIG welding process parameters using Taguchi's analysis and response surface methodology. International Journal of Mechanical Engineering and Technology, 8(11), 932-941.

[72] Abebe, D. G., & Bogale, T. M. (2023). Optimization of TIG welding process parameters on 304 austenitic stainless steel sheet metal using fuzzy logic-based Taguchi method. Engineering Research Express, 5(4), 045045.

[73] Omprakasam, S., Marimuthu, K., Raghu, R., & Velmurugan, T. (2022). Statistical modelling and optimization of TIG welding process parameters using Taguchi's method. Strojniški vestnik-Journal of Mechanical Engineering, 68(3), 200-209.

[74] Greyjevo, O. G. T. V. Z., & Metodo, A. I. T. (2009). Optimization of weld bead geometry in TIG welding process using grey relation analysis and Taguchi method. Materiali in tehnologije, 43(3), 143-149.

[75] Ogbonna, O. S., Akinlabi, S. A., Madushele, N., Fatoba, O. S., & Akinlabi, E. T. (2023). Grey-based taguchi method for multi-weld quality optimization of gas metal arc dissimilar joining of mild steel and 316 stainless steels. Results in Engineering, 17, 100963.

[76] Bandhu, D., Kumari, S., Prajapati, V., Saxena, K. K., & Abhishek, K. (2021). Experimental investigation and optimization of RMDTM welding parameters for ASTM A387 grade 11 steel. Materials and Manufacturing Processes, 36(13), 1524-1534.

[77] Ahmad, A., & Alam, S. (2018, August). Grey based Taguchi method for optimization of TIG process parameter in improving tensile strength of S30430 stainless steel. In IOP Conference Series: Materials Science and Engineering (Vol. 404, No. 1, p. 012003). IOP Publishing.

[78] Srirangan, A. K., & Paulraj, S. (2016). Multi-response optimization of process parameters for TIG welding of Incoloy 800HT by Taguchi grey relational analysis. Engineering science and technology, an international journal, 19(2), 811-817.

[79] Bahar, D. & Pandey, V & Ijakpaul, T & Anil, Ch & Dilbahar, Muhammad. (2018). Design of TIG welding experiments to optimize the hardness and Toughness of weld bead formed between Cu alloys.

[80] Abima, C. S., Madushele, N., Adeleke, O., Akinlabi, S. A., & Akinlabi, E. (2023). Optimization and Prediction of TIG-MIG hybrid Joint Strength using Adaptive

Neuro-Fuzzy Inference System (ANFIS) Model. In E3S Web of Conferences (Vol. 430, p. 01238). EDP Sciences.

[81] Rajaravi, C., Ganesh, B., Lakshmanan, S., & Gobalakrishnan, B. (2023). Influence of TIG welding processing parameters on mechanical properties of austenitic stainless steel using Taguchi analysis. Materials Today: Proceedings, 72, 2402-2409.

[82] Sutar, V. J., & Jadhav, B. R. (2021). Implementation of TOPSIS optimisation technique in comparative analysis of conventional TIG and activated TIG welding of stainless steel 304L. International Journal of Materials Engineering Innovation, 12(3), 188-206.

[83] Dahmene, F., Yaacoubi, S., Mountassir, M. E., Bouzenad, A. E., Rabaey, P., Masmoudi, M., ... & Taram, A. (2022). On the nondestructive testing and monitoring of cracks in resistance spot welds: recent gained experience. Welding in the World, 66(4), 629-641.

[84] Korra, N. N., & Balasubramanian, K. R. (2012). Parametric optimization of TIG welding on 316l austenitic stainless steel by grey-based Taguchi method. Advanced Materials Research, 383, 4667-4671.

[85] Shrivastava, M., & Kumar, R. (2020). Optimization of GTA Welding Parameters for AISI 304 Stainless Steel using Taguchi Method. In International Conference of Advance Research & Innovation (ICARI).

[86] Mondal, S., Nandi, G., & Pal, P. K. (2021). Parametric optimization of TIG welding of duplex stainless steel without filler rod by PCA method. In IOP Conference Series: Materials Science and Engineering (Vol. 1017, No. 1, p. 012007). IOP Publishing.

[87] Chandrasekhar, N., & Vasudevan, M. (2010). Intelligent modeling for optimization of A-TIG welding process. Materials and Manufacturing Processes, 25(11), 1341-1350.

[88] Vinoth, V., Sudalaimani, R., Ajay, C. V., Kumar, C. S., & Prakash, K. S. (2021). Optimization of mechanical behaviour of TIG welded 316 stainless steel using Taguchi based grey relational analysis method. Materials today: proceedings, 45, 7986-7993.

[89] Avinash, S., Balram, Y., Babu, B. S., & Venkatramana, G. (2019). Multi-response optimization of pulse TIG welding process parameters of welds AISI 304 and Monel 400 using grey relational analysis. Materials today: proceedings, 19, 296-301.

[90] Hu, J., Liu, H., Bi, J., Li, Y., Ao, S., & Luo, Z. (2022). Quality prediction of aluminum alloy resistance spot welding with shunting by introducing spacing factor. Welding International, 36(12), 716-731.

[91] Li, X., Gong, B., Liu, X., Deng, C., & Li, Y. (2018). Effects of hydrogen and microstructure on tensile properties and failure mechanism of 304L K-TIG welded joint. Materials Science and Engineering: A, 735, 208-217.

[92] Patil, S. R., & Waghmare, C. A. (2013). Optimization of MIG welding parameters for improving strength of welded joints. Int. J. Adv. Eng. Res. Stud, 14, 16.

[93] Tabrizi, T. R., Sabzi, M., Anijdan, S. M., Eivani, A. R., Park, N., & Jafarian, H. R. (2021). Comparing the effect of continuous and pulsed current in the GTAW process of AISI 316L stainless steel welded joint: microstructural evolution, phase equilibrium, mechanical properties, and fracture mode. Journal of Materials Research and Technology, 15, 199-212.

[94] Sabzi, M., & Dezfuli, S. M. (2018). Drastic improvement in mechanical properties and weldability of 316L stainless steel weld joints by using electromagnetic vibration during GTAW process. Journal of Manufacturing Processes, 33, 74-85.

[95] Anijdan, S. M., Sabzi, M., Ghobeiti-Hasab, M., & Roshan-Ghiyas, A. (2018). Optimization of spot-welding process parameters in dissimilar joint of dual phase steel DP600 and AISI 304 stainless steel to achieve the highest level of shear-tensile strength. Materials Science and Engineering: A, 726, 120-125.

[96] Sabzi, M., Anijdan, S. M., Eivani, A. R., Park, N., & Jafarian, H. R. (2021). The effect of pulse current changes in PCGTAW on microstructural evolution, drastic improvement in mechanical properties, and fracture mode of dissimilar welded joint of AISI 316L-AISI 310S stainless steels. Materials Science and Engineering: A, 823, 141700.

[97] Tarng, Y. S., Juang, S. C., & Chang, C. H. (2002). The use of grey-based Taguchi methods to determine submerged arc welding process parameters in hardfacing. Journal of materials processing technology, 128(1-3), 1-6.

[98] Murugan, N., & Parmar, R. S. (1994). Effects of MIG process parameters on the geometry of the bead in the automatic surfacing of stainless steel. Journal of Materials Processing Technology, 41(4), 381-398.

[99] Sakthivel, T., Vasudevan, M., Laha, K., Parameswaran, P., Chandravathi, K. S., Mathew, M. D., & Bhaduri, A. K. (2011). Comparison of creep rupture behaviour of type 316L (N) austenitic stainless-steel joints welded by TIG and activated TIG welding processes. Materials Science and Engineering: A, 528(22-23), 6971-6980.

[100] Srirangan, A. K., & Sathiya, P. (2017). Optimisation of process parameters for gas tungsten arc welding of incoloy 800HT using TOPSIS. Materials Today: Proceedings, 4(2), 2031–2039.

[101] Balasubramanian, V., & Guha, B. (1999). Effect of welding process on fatigue crack growth behaviour of ASTM 517 'F' grade steel weld metals. Science and Technology of Welding and Joining, 4(4), 233–239.

[102] Ericsson, M. (2003). Influence of welding speed on the fatigue of friction stir welds, and comparison with MIG and TIG. International Journal of Fatigue, 25(12), 1379–1387.

[103] Bendikiene, R. (2015). Comparative analysis of microstructure and quality of gas metal arc welded and shielded metal arc welded joints. Mechanika, 21(4).

[104] Karthik, G., Karuppuswamy, P., & Amarnath, V. (2014). Comparative evaluation of mechanical properties and micro structural characteristics of 304 stainless steel weldments in TIG and SMAW welding processes.

[105] Jorge, J. C. F., Monteiro, J. L. D., Gomes, A. J. de C., Bott, I. de S., Souza, L. F. G. de, Mendes, M. C., & Araújo, L. S. (2019). Influence of welding procedure and PWHT on HSLA steel weld metals. Journal of Materials Research and Technology, 8(1), 561–571.

[106] Shah, L. H., Akhtar, Z., & Ishak, M. (2013). Investigation of aluminum-stainless steel dissimilar weld quality using different filler metals. International Journal of Automotive and Mechanical Engineering, 8, 1121–1131.

[107] He, Z.-B., Peng, Y.-Y., Yin, Z.-M., & Lei, X.-F. (2011). Comparison of FSW and TIG welded joints in Al-Mg-Mn-Sc-Zr alloy plates. Transactions of the Nonferrous Metals Society of China, 21(8), 1685–1691.

[108] Sayer, S., Yeni, C., & Ertugrul, O. (2011). Comparison of mechanical and microstructural behaviours of tungsten inert gas welded and friction stir welded dissimilar aluminum alloys AA 2014 and AA 5083. Kovove Materialy, 49(2), 155–16

[109] Roy, Rajit & St, Cahyono. (2022). Design of Experiments Using the Taguchi Approach 16 Steps to Product and Process Improvement.

[110] Taguchi, G., Chowdhury, S., & Wu, Y. (2004). Taguchi's quality engineering handbook. Wiley.

[111] Taherdoost, H., & Madanchian, M. (2023). Multi-criteria decision making (MCDM) methods and concepts. Encyclopedia, 3(1), 77–87.

[112] Aruldoss, M., Lakshmi, T. M., & Venkatesan, V. P. (2013). A survey on multi criteria decision making methods and its applications. American Journal of Information Systems, 1(1), 31-43.

[113] Shih, H.-S., & Olson, D. L. (2022). TOPSIS and its Extensions: A Distance-Based MCDM Approach. Springer International Publishing.

[114] Krishnaiah, K., & Shahabudeen, P. (2012). Applied design of experiments and Taguchi Methods. PHI Learning.

[115] Collyer, Charles & Enns, James. (1986). Analysis of Variance - The Basic Designs.

[116] Lindman, H. R. (1992). Analysis of variance in experimental design. Springer New York.

[117] Rojas, H., Vargas, Z., Valdez, S., Serrano, M., del Pozo, A., & Alcántara, M. (2024). Taguchi, Grey Relational Analysis, and ANOVA optimization of TIG welding parameters to maximize mechanical performance of Al-6061 T6 alloy. Journal of Manufacturing and Materials Processing, 8(6), 246.

[118] Wang, H., & Chen, L. (2021). Optimization of TIG Welding for Magnesium Alloys. Journal of Magnesium and Alloys, 9(1), 43.

[119] Ghosh, N., Pal, P. K., & Nandi, G. (2018). Investigation on dissimilar welding of AISI 409 ferritic stainless steel to AISI 316L austenitic stainless steel by using grey based Taguchi method. Advances in Materials and Processing Technologies, 4(3), 385–401.

[120] Srirangan, A. K., & Sathiya, P. (2017). Optimisation of process parameters for gas tungsten arc welding of incoloy 800HT using TOPSIS. Materials Today: Proceedings, 4(2), 2031–2039.

[121] Chellappan, M., Lingadurai, K., & Sathiya, P. (2017). Characterization and Optimization of TIG welded supermartensitic stainless steel using TOPSIS. Materials Today: Proceedings, 4(2), 1662–1669.

[122] Mondal, S., & Kumar Bose, G. (2023). Parametric optimization for hardness of tig welded duplex stainless steel. International Journal of Industrial Optimization, 4(2), 145–155.
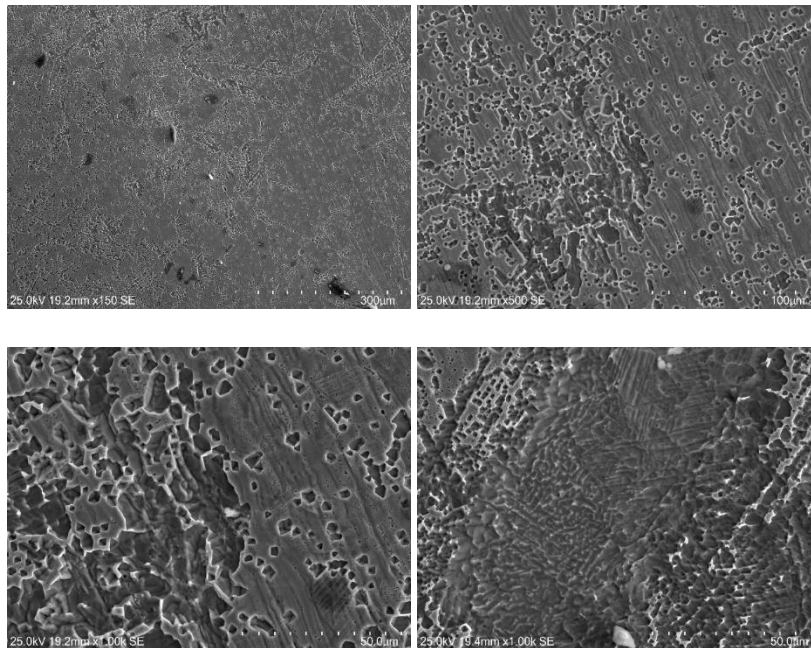
Angshuman Roy

Appendix

Below are random photographic images of a few micro-hardness indentation samples.
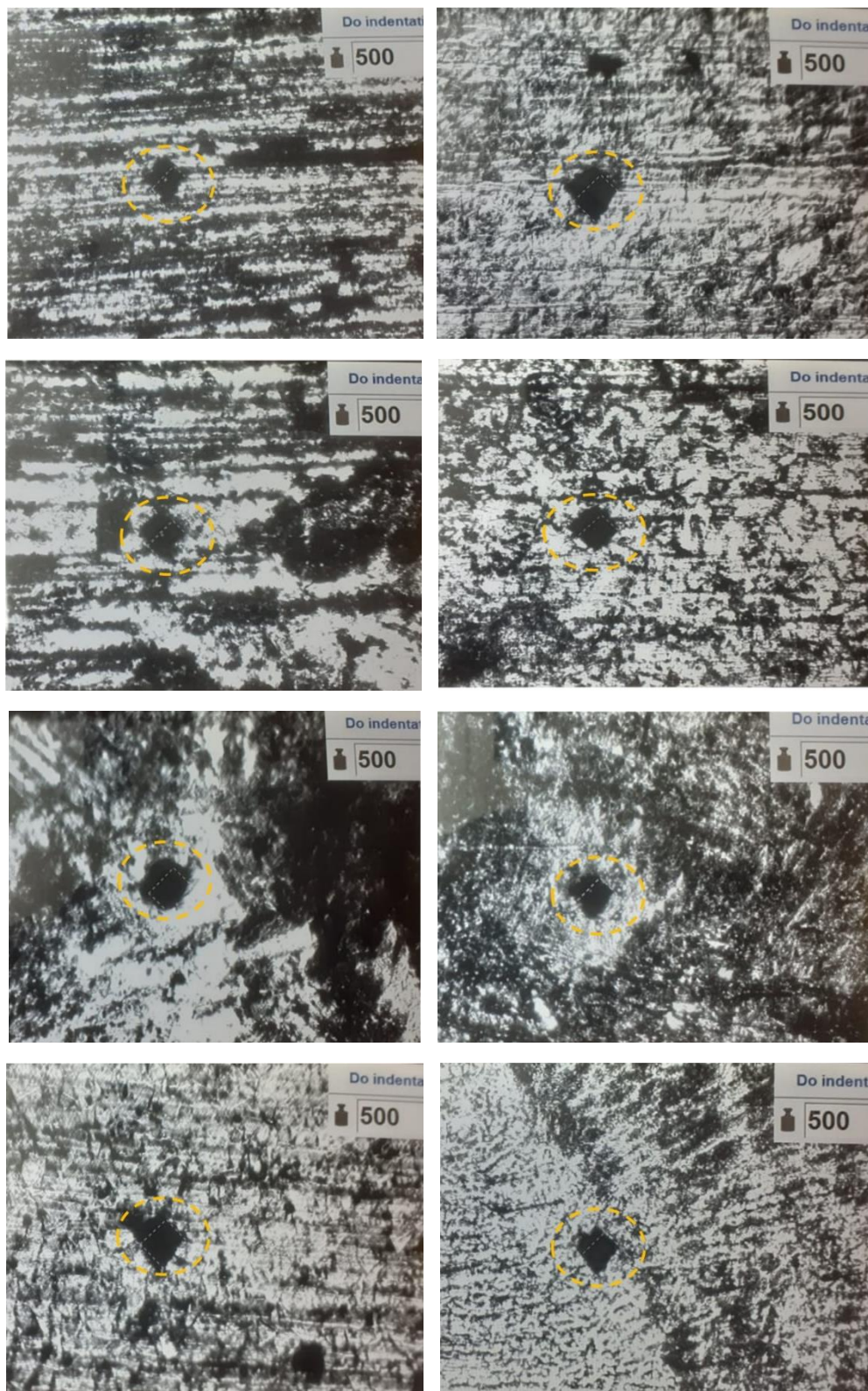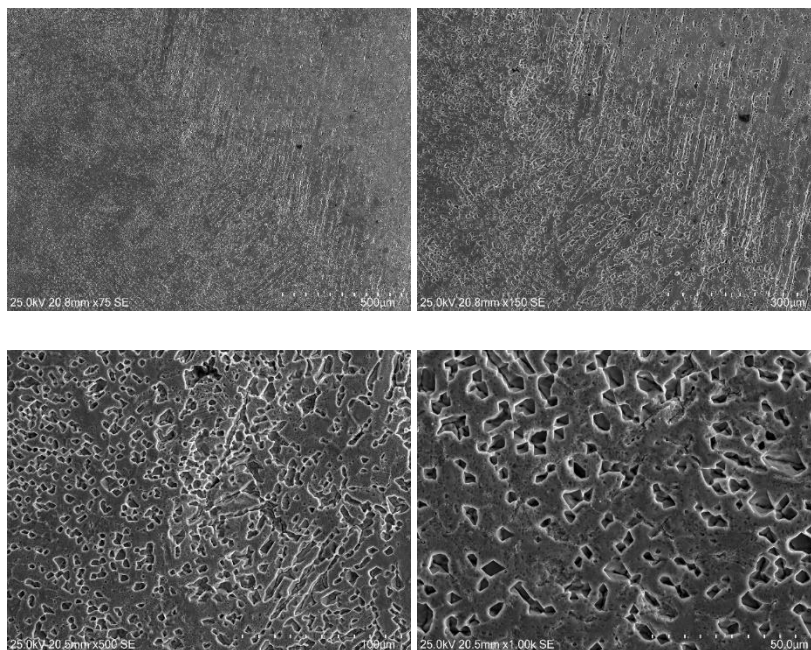
The images of SEM of few welded samples are shown below:
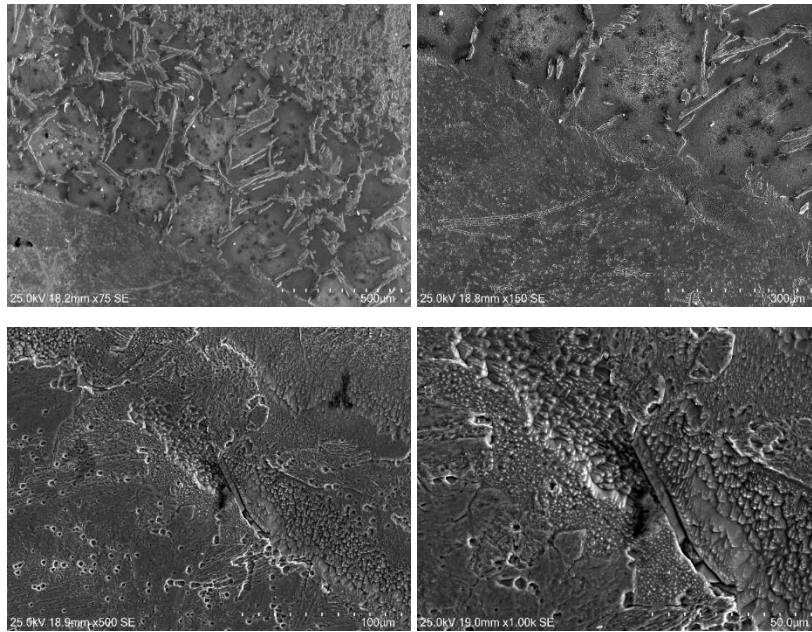
SEM images of welding of ASS 304L

SEM images of sample 2

SEM images of sample S3

SEM images of samples S4
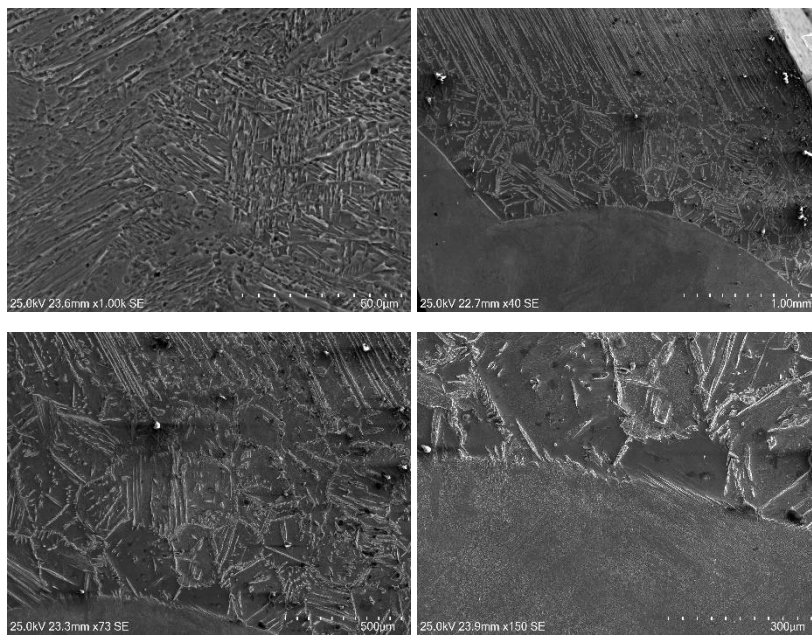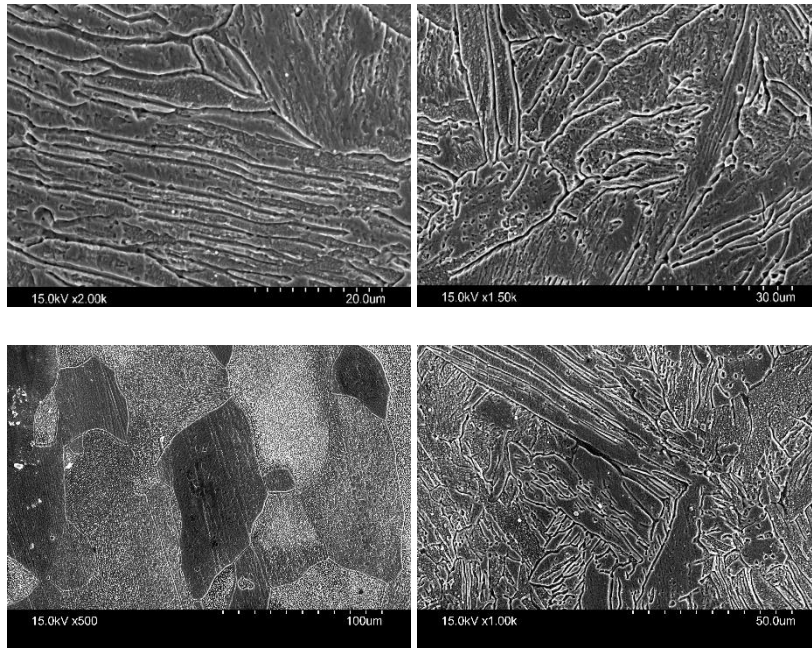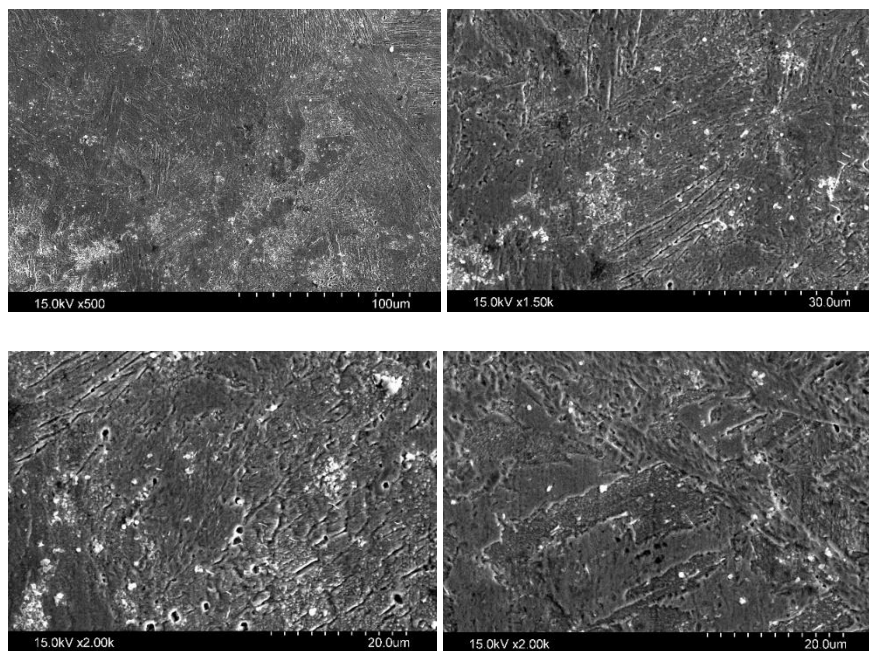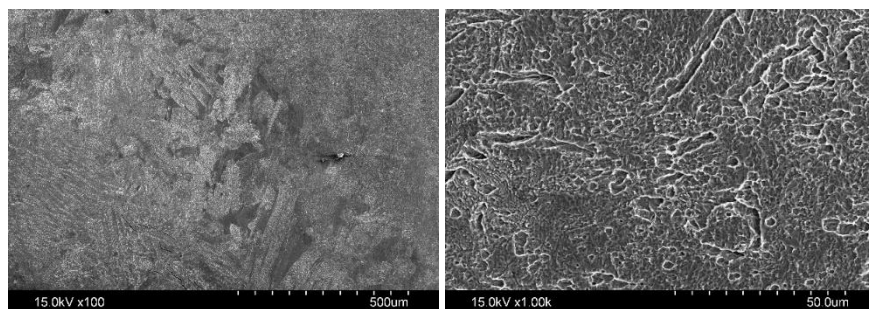

SEM images of samples S8
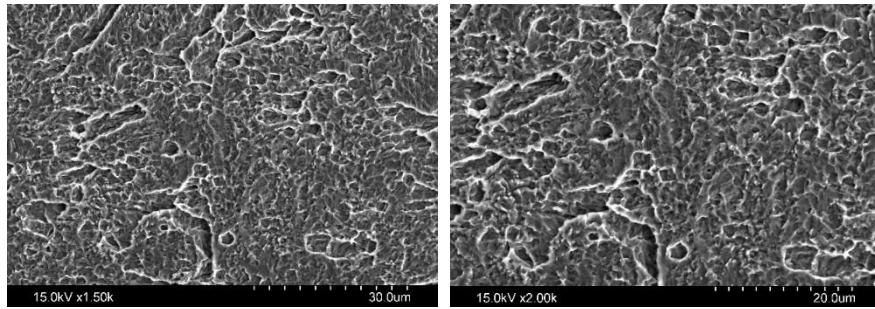
SEM images of welding of FSS 409M
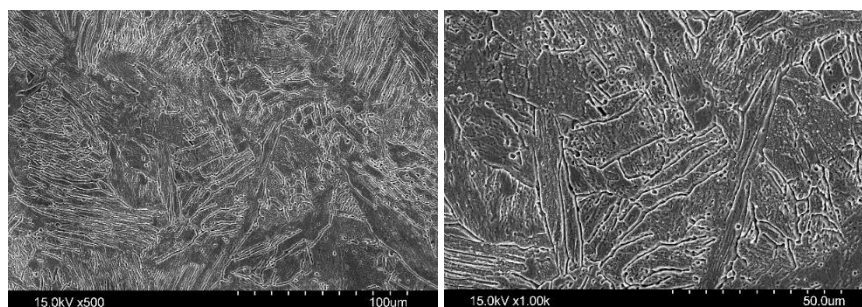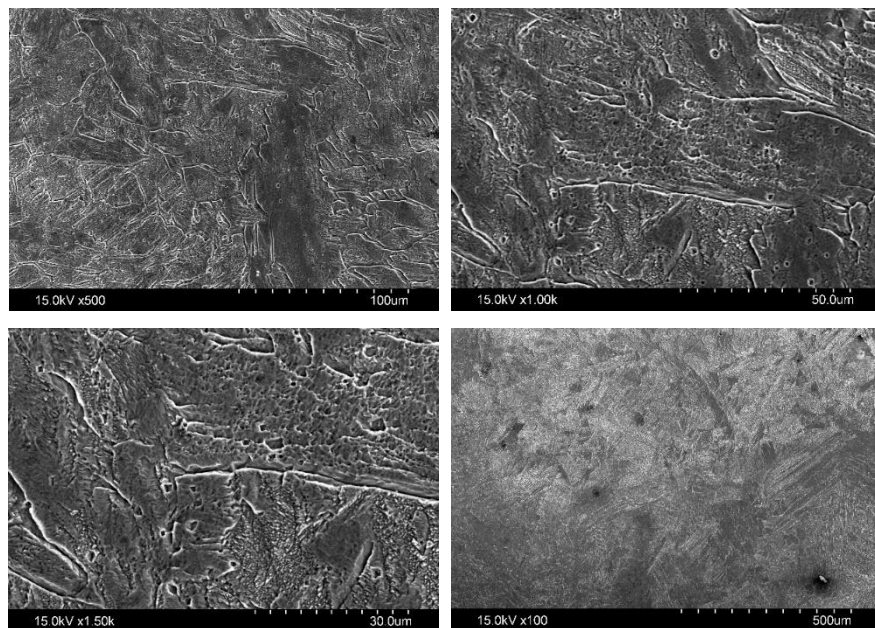
SEM image for S9B
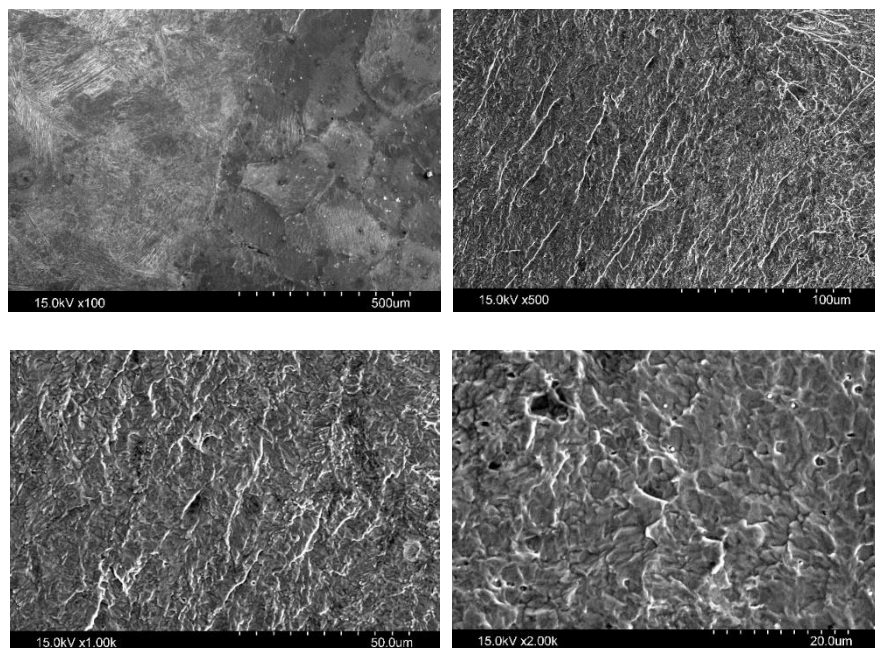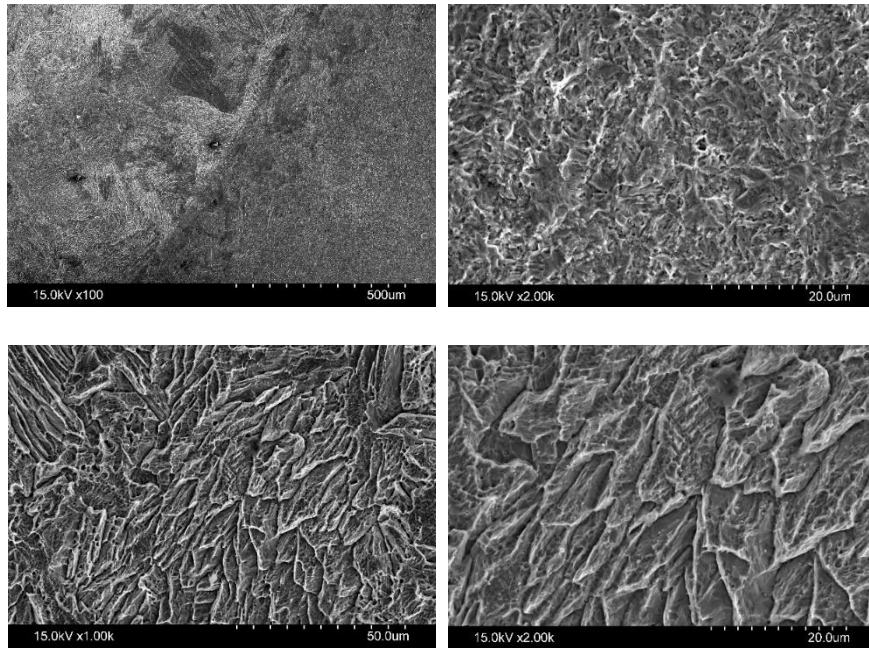

SEM image for S1B

SEM image for S3B

SEM images of dissimilar welding of ASS 304L and FSS 409M

SEM image for S5A

SEM image for S2A

SEM image for S6A

Three sets of tensile test samples (ASS 304L, FSS 409M and ASS 304L+ FSS 409M)

Tensile test samples preparation in milling machine

ORIGINAL PAPER

Analysis of the multi-criteria optimization strategies for determining the weld quality of dissimilar TIG welding between ferritic and austenitic stainless steel

Angshuman Roy[1] · Nabendu Ghosh[2] · Subrata Mondal[1]

Abstract

This research is an analytical and experimental investigation into the process of TIG welding of incompatible materials, notably austenitic and ferritic stainless steels. The Taguchi L9 array was utilized in this weld. After welding, weld samples have been examined visually and X-ray radiographic examination to detect any defects that may be hidden beneath the surface. Combination of advanced analytical techniques GRA, TOPSIS and PCA are used in the study to analyze the data and to identify the optimized input parameters for a multi-objective function. The use of analysis of variance has also helped in identifying the individual contribution of each parameter towards achieving the desired outcomes. Overall, this study demonstrates the importance of advanced analytical techniques in optimizing complex systems and processes. From the results, it can be conclude that PCA is the best optimization technique compared to the remaining techniques.

Abbreviations

GRA	Grey relational analysis
PCA	Principal component analysis
TOPSIS	Technique for order preference by similarity to ideal solution method
TIG	Tungsten inert gas welding
C	Current
G	Gas flow rate
S	Travel speed

✉ Nabendu Ghosh
nabendu2003_ghosh@yahoo.co.in

Angshuman Roy
angshuman_roy01@yahoo.co.in

Subrata Mondal
sub.mondal@gmail.com

[1] Department of Power Engineering, Jadavpur University, Kolkata 700106, India

[2] Department of Mechanical Engineering, Jadavpur University, Kolkata 700032, India

1 Introduction

The quality is the foundation of the success. The customers will judge the products based on their quality, and a bad reputation for quality can quickly lead to elimination by the market. A quality management system for welding should start with a thorough understanding of the design requirements and specifications. Once the design is complete, the materials should be carefully selected to ensure that they meet the necessary quality standards. All welding processes involve joining incompatible substances. Linking materials of different properties can cut down on product bulk and expense without compromising reliability or durability. Joint failure can be avoided by using strong and ductile dissimilar welds. Nuclear power plant, coal-fired boilers, and car industry use dissimilar metal joints. As TIG improves weldment quality, it is used in the production of numerous ferrous and non-ferrous metals. Body-centered cubic crystal makes ferritic stainless steels (FSS) less ductile than austenitic steel, and prevents FSS (ferritic stainless steel) from being heat-treated in the same way as martensitic steel. Older ferritics, like as AISI 430, are used for non-corrosion-critical applications such as kitchenware. FSS combine stainless steel and rust-prone carbon steel benefits. Joints made of ferritic and austenitic materials (F/A joints) are used extensively in the

Optimization of tig welding parameters to enhance the tensile strength of AISI 304 L stainless steel joints using taguchi methodology

Nabendu Ghosh[1] · **Angshuman Roy**[2]

Abstract

TIG-welded AISI 304 L austenitic stainless steel samples are studied in the present work. Several butt joints are made. Plate thickness remains 3 mm. nine butt-welded joints were constructed. Each joint sample was made under specific welding settings. This study varied welding current, gas flow rate, and travel speed. L9 Taguchi design was used. The following input parameters are chosen and given three alternative values: welding current (95 A, 105 A and 115 A), gas flow rate (10 L/min, 15 L/min and 20 L/min), and travel speed (2 mm/s, 2.5 mm/s and 3 mm/s). TIG-welded AISI 304 L austenitic stainless steel butt joints have been visually and X-ray radio graphically analyzed. Then, samples were cut and machined to tensile testing dimensions. A small section of butt-welded joints were taken out for metallographic test samples, which were ground, lapped, and etched before examination under a metallurgical microscope. In TIG welding, welding current, gas flow rate, and travel speed affect austenitic stainless steel welded joints. Ultimate tensile strength (UTS) and percentage of elongation (EL) of welded specimens have also been used to assess weld quality. Taguchi approach predicted optimal parametric setting, and confirmatory test validated optimized answers. Graphics and micrographs depict results. Interpretations and analysis of experimental results have yielded relevant conclusions. The present work may build a comprehensive knowledge base from which working engineers and technicians can select parameter settings with ease in order to produce welds of higher quality that are more accurately, dependably, and predictably.

Keywords TIG welding · Visual and X-ray radiographic test · Tensile test · Microstructure · Taguchi method

1 Introduction

Austenitic stainless steels have slower molten weld pools than ferritic and martensitic alloys. This may limit austenitic alloy weld metal flow and wet ability, reducing fusion defects. Austenitic stainless steel has a wide range of applications, including structural support and containment, construction, culinary, and medical. This study used austenitic stainless steel AISI 304 L. Modern manufacturing strives towards better welds. Hence, adjusting welding quality-determining process parameters is the real challenge. Due of AISI 304 L's corrosion and crack resistance, TIG (Tungsten Inert Gas) welding is difficult. Research is needed because TIG welding austenitic stainless steel with multiple input parameters can be complicated. Some researchers put in significantly more effort than others do because of the diverse things that they are researching. Fatigue loading, bending characteristics, zone hardness, weld width, ultimate tensile strength, yield strength, percentage elongation, and impact strength can all be affected by a number of inputs, the effects of which may be difficult to study. It is possible to combine the processes of microstructural study and analysis under a variety of welding settings, process optimization, and mathematical modelling. Any welding job should generate a connection with the desired qualities. Certain parameters affect welded joint quality across welding procedures, while others are method-specific. Scientists are still examining welding processes. These investigations aim to improve TIG welding quality and ensure that the welded junction has the appropriate

✉ Nabendu Ghosh
  nabendu2003_ghosh@yahoo.co.in

  Angshuman Roy
  angshuman_roy01@yahoo.co.in

1 Mechanical Engineering Department, Jadavpur University, Kolkata 700032, India

2 Power Engineering Department, Jadavpur University, Kolkata 700098, India

Taylor & Francis
Taylor & Francis Group

Check for updates

RESEARCH ARTICLE

Effect of heat input on mechanical and metallurgical properties of AISI 304L stainless steel by using TIG welding

Angshuman Roy[a], Nabendu Ghosh[b] and Subrata Mondal[a]

[a]Power Engineering Department, Jadavpur University, Kolkata, India; [b]Mechanical Engineering Department, Jadavpur University, Kolkata, India

ABSTRACT

In this research, we examine the ways in which heat treatment affects TIG-welded joints made from austenitic AISI 304 L stainless steel. TIG welding was performed on austenitic 304 L stainless steel at low (0.57 KJ/mm), medium (0.63 KJ/mm), and high (0.69 KJ/mm) heat. TIG welding was used to join together AISI 304 L stainless steel samples here. A consistent 3 mm thick plates were taken for the joints. All of the joints were butt-welded. In order to conduct tensile tests, hardness tests, and microstructural analyses, samples were cut and machined to the appropriate dimensions. Once the joints are ready, visual inspection and X-rays were conducted. This study examined the effects of applying different levels of heat on AISI 304 L stainless steel butt joints. The material's tensile properties were tested and analysed after being butt-joined. Welded samples' microstructures were examined with a Leica DM LM metallurgical microscope. Consistent with the microstructural characteristics, the tensile test findings **were** also consistent. The research found that compared to joints prepared with low and high heat input, those prepared with medium heat input exhibited greater tensile strength, percentage elongation and micro hardness value.

1. Introduction

304L is a material that lacks magnetic characteristics, is less expensive overall, and is widely available on the market. It has outstanding formability, ductility, weldability, toughness, and high tensile strength at elevated temperatures [1]. The austenitic stainless steels of the 300 series include the marine-grade 304 L grade, sometimes known as grade 304 L. The letter 'L' denotes a stainless steel with exceedingly low carbon content in this application. Due to the extraordinarily low carbon concentration of this material, welding produces substantially less harmful carbide precipitation. In comparison to other varieties of stainless steel, this type is often the most welds able due to the physical features it possesses and the welding processes that are done on it. TIG welding is commonly required for the connecting of austenitic stainless-steel components [2]. In the molten weld pool, one of the most important governing elements for heat transfer and mass transfer, liquid movement, and thermochemical reactions is the amount of heat that is introduced by welding [3]. As the weld metal hardens, it

also plays a crucial role in altering its chemistry. Li et al. [4] examined the impact of hydrogen on 304 L K-TIG weld metal tensile characteristics and failure mechanism. Hydrogen atoms interact with strain-induced ′ martensite to reduce ductility and strength. Kumar et al. [5] examined welding current's effect on welded joint tensile strength and microstructural change in the fusion zone, heat-affected zone, and austenitic stainless steel 304 L parent metal. Pulsing and continuous current affect AISI 304 L butt joints, according to Widyianto et al. [6]. Patil and Waghmare [7] examined welding current, voltage, and speed on AISI 1030 mild steel UTS. Taguchi method is used to investigate and optimize welding parameters. Welding speed, among other factors, affects tensile strength. Increasing welding speed and reducing current increases the weld's tensile strength. Ambekar and Sunil [8] explored welding and penetration. GMAW process parameters of AISI 410 Martensitic stainless steel were optimized using L16-based orthogonal array Taguchi analysis. Raut and Shelke [9] did a case study to determine the

---

Taylor & Francis
Taylor & Francis Group

Check for updates

RESEARCH ARTICLE

Multi-criteria optimization of TIG welding process parameters on AISI 409M stainless steel by Grey Taguchi method

Angshuman Roy[a], Nabendu Ghosh[b] and Subrata Mondal[a]

[a]Power Engineering Department, Jadavpur University, Kolkata, India; [b]Mechanical Engineering Department, Jadavpur University, Kolkata, India

ABSTRACT

AISI 409M ferritic stainless steel materials were examined in this study. TIG welding was utilized for the creation of butt welded joints in the construction of the L9 Taguchi orthogonal array experiment. A visual and X-ray examination of the joints followed the procedure. After the butt-joining, a slew of experiments were run to figure out the material's specific properties. There has been an evaluation of the weld quality in terms of the specimens' ultimate tensile strength (UTS) and percentage elongation (PE). Grey-Taguchi methodology was used to interpret, discuss and analyse the collected data. It appears that the investigation has led to some conclusive results.

1. Introduction

Eleven to twelve percent chromium utility stainless steels bridge the difference in corrosion resistance between stainless steels and carbon steels [1,2]. Most household utensils and other items are made of ferritic steels. Ferritic stainless steels (FSSs) are becoming increasingly popular since they resist corrosion better and cost less. It is also common to utilize low-chromium grades in vehicle exhaust systems because of their corrosion resistance and cost-effective fabrication [2]. SS 409M plates are highly sought after for their excellent corrosion resistance, and this is largely due to their composition of ferritic steel. Ferritic steel is a type of chromium stainless steel that is known for its exceptional resistance to corrosion, making it an ideal material for use in a variety of applications. This type of steel is made up of a high percentage of chromium, which gives it its characteristic resistance to corrosion. In addition to chromium, ferritic steel also contains varying amounts of carbon, silicon and other elements that help to improve its strength and durability.

When it comes to manufacturing SS 409M plates, ferritic steel is the material of choice due to its impressive performance in harsh environments. When exposed to high temperatures, chemicals or other corrosive substances, ferritic steel was able to withstand the elements and maintain its integrity over time. Overall, the use of ferritic steel in the production of SS 409M plates is a testament to the strength and versatility of this unique material. By leveraging the properties of ferritic steel, manufacturers are able to create products that are both durable and reliable, making them a popular choice for a wide range of industries and applications. High temperatures do not alter stainless steel 409M mechanical or corrosion qualities. It is widely accepted that it is made of stainless steel chromium, which is used in exhaust systems and other applications that require weldability. It is widely used in the pipe and automobile industries, as well as in mildly corrosive environments, for plates made of 409M. There are several applications for stainless steels of grade 409M in the automotive industry including exhaust tubes, catalytic converters and mufflers. TIG can provide superior weldments under specific circumstances. Weld-quality criteria are a factor in the usefulness and implementation of this technique. The material to be welded is obviously one of the requirements. Weld quality is influenced by bead geometry, mechanical–metallurgical qualities and weld chemistry, all of which are impacted by input parameters. In

---

CERTIFICATE

2nd International Conference on Mechanical Engineering (INCOM 2024)

05 – 06 January 2024 | Jadavpur University

INCOM24-309

This is to certify that *Angshuman Roy* from Research Scholar Jadavpur University has presented the paper titled "**Grey-Based Taguchi Technique for Parametric Optimization of TIG Welded AISI 304L Austenitic Stainless Steel**" [Paper ID: **INCOM24-309**] at the 2nd International Conference on Mechanical Engineering (INCOM 2024) held at Jadavpur University, Kolkata, India during 05 – 06 January 2024. The conference has been organized by the Department of Mechanical Engineering, Jadavpur University.

Prokash Chand Roy 5/01/24
Organizing Secretary
(INCOM 2024)

Karmakar 05/01/24
Chairman
(INCOM 2024)

International Conference on Advanced Mechanical Engineering and Industrial Management

ICAMEIM
KOLKATA, INDIA 2024

Organized by

Department of Mechanical Engineering

Swami Vivekananda Institute of Science & Technology, Kolkata

CERTIFICATE OF PARTICIPATION

This certificate is presented to **Angshuman Roy** for his/her actively participation during the conduct of three-days International conference on **"International Conference on Advanced Mechanical Engineering and Industrial Management"** held in the Swami Vivekananda Institute of Science & Technology, Kolkata, India during 11th to 13th March 2024.

Sghosh
Dr. Sonali Ghosh
Principal

Suman Das
Dr. Suman Das
Convener

Das
Dr. Somnath Das
Organizing Secretary